

Utah State University

DigitalCommons@USU

All Graduate Theses and Dissertations

Graduate Studies

5-2016

Computational Studies of Microscopic Superfluidity in the 4He Clusters

Angeline R. Wairegi

Follow this and additional works at: <https://digitalcommons.usu.edu/etd>



Part of the [Chemistry Commons](#)

Recommended Citation

Wairegi, Angeline R., "Computational Studies of Microscopic Superfluidity in the 4He Clusters" (2016). *All Graduate Theses and Dissertations*. 4949.

<https://digitalcommons.usu.edu/etd/4949>

This Dissertation is brought to you for free and open access by the Graduate Studies at DigitalCommons@USU. It has been accepted for inclusion in All Graduate Theses and Dissertations by an authorized administrator of DigitalCommons@USU. For more information, please contact digitalcommons@usu.edu.



COMPUTATIONAL STUDIES OF MICROSCOPIC SUPERFLUIDITY IN ^4He
CLUSTERS

by

Angeline R. Wairegi

A dissertation submitted in partial fulfillment
of the requirements for the degree

of

DOCTOR OF PHILOSOPHY

in

Chemistry

Approved:

Dr. David Farrelly
Major Professor

Dr. Alexander Boldyrev
Committee Member

Dr. Stephen Bialkowski
Committee Member

Dr. Steve Scheiner
Committee Member

Dr. T.C Shen
Committee Member

Mark R. McLellan
Vice President for Research and
Dean of the School Graduate
Studies

UTAH STATE UNIVERSITY

Logan, Utah

2016

Copyright © Angeline R. Wairegi 2016

All Rights Reserved

ABSTRACT

Computational Studies of Microscopic Superfluidity in ^4He Clusters

by

Angeline Wairegi, Doctor of Philosophy

Utah State University, 2016

Major Professor: David Farrelly

Department: Department of Chemistry and Biochemistry

The physics that result in the decoupling of a molecule from a bosonic solvent at 0 K are studied. Fixed-node diffusion Monte Carlo (FNDMC) coupled with a Genetic Algorithm is used to perform simulations of the bosonic droplets doped with various molecules. The efficacy and accuracy of this approach is tested on a strongly coupled 2-dimensional quartic oscillator with excellent results. This algorithm is then applied to $^4\text{He-CO}$ and $^4\text{He-HCN}$ clusters respectively in an effort to determine the factors that result in the onset of microscopic superfluidity. The decoupling of the doped molecule from the bosonic solvent is found to be, primarily, a result of the combined effect of the repulsive interaction between the helium atoms and bose symmetry. The effects of rotor size versus molecular anisotropy in a NH_3 molecule seeded into a ^4He droplet is studied as well. Simulations are done using the accurate rotational constants ($B_0 = 9.945 \text{ cm}^{-1}$, $C_0 = 6.229 \text{ cm}^{-1}$) and using “fudged” versions of the rotational constants ($B_{fudged} = 0.9945 \text{ cm}^{-1}$, $C_{fudged} = 0.6229 \text{ cm}^{-1}$) for the $|0011\rangle$ state. The simulations done with the fudged rotational constants experience a slightly smaller reduction than those done using the accurate rotational constants. This is attributed to the importance of molecular anisotropy versus the size of larger rotational constants in molecules whose rotational constants fall in an intermediate regime.

(134 pages)

PUBLIC ABSTRACT

Computational Studies of Microscopic Superfluidity in ^4He Clusters

Angeline Wairegi

The onset of microscopic superfluidity has been reported in ultracold droplets of bosons (^4He atoms or para- H_2 molecules) containing a variety of molecular dopants. The physics of these droplets involve both Bose-Einstein condensation (BEC) and superfluidity. The two phenomena, while closely related, are not exactly the same. Superfluidity is fundamentally a microscopic effect and no thermodynamic limit is necessary; it is still remarkable, though, that the signature of superfluidity has been reported in doped droplets consisting of as few as 4 ^4He atoms. The studies presented here adopt a molecular vantage point to investigate the quantum mechanics behind the rotational dynamics of dopant molecules in small droplets consisting of ^4He atoms. The overarching goal is to develop a detailed quantum mechanical understanding of the onset of microscopic superfluidity. Physically small though these droplets are, they represent a significant challenge to many body quantum physics. The most direct method of investigation is to use Quantum Monte Carlo (QMC) algorithms to perform the calculations. Fixed node diffusion Monte Carlo (FNDMC), a type of QMC algorithm, is employed for these studies. Finding nodal surfaces for use in the calculation of the excited states is an essential part of this algorithm, which assumes the nodal topology of the target wave function is known in advance. To that end, we developed a novel approach utilizing a genetic algorithm version of the FNDMC method in which the nodal hypersurfaces are computed systematically and on-the-fly within the DMC procedure. This algorithm is then applied to elucidating the nodal topology of $^4\text{He}\text{-CO}$, $^4\text{He}\text{-HCN}$ and $^4\text{He}\text{-NH}_3$ and is then utilized to study the phenomenon of microscopic superfluidity and the renormalization of rotational constants in these clusters.

ACKNOWLEDGMENTS

I would like to thank my mother and friends for their support throughout this journey. I owe my continued sanity to them. I would like to thank my advisor, Dr. Farrelly, for his guidance and patience. He did the impossible by turning a self confessed luddite into a programmer. A heart felt thank you to the members of my dissertation committee: Dr. Alex Bolydrev, Dr. Steve Scheiner, Dr. Stephen Bialkowski and Dr. T.C Shen for their support. I would also like to thank the NSF for the grant that funded this research.

Angeline Wairegi

CONTENTS

	Page
ABSTRACT	iii
PUBLIC ABSTRACT	iv
ACKNOWLEDGMENTS	v
LIST OF FIGURES	viii
LIST OF TABLES	x
1. INTRODUCTION	1
2. ON THE FLY NODAL SEARCHES IN IMPORTANCE SAMPLED, FIXED-NODE DIFFUSION MONTE CARLO USING A PARALLEL, FINE-GRAINED, GENETIC ALGORITHM	26
2.1. Graphical abstract	27
2.2. Abstract	28
2.3. Introduction	28
2.4. Genetic-algorithm diffusion Monte Carlo	30
2.4.1. Genetic Algorithms	31
2.4.2. Nodal optimization	33
2.5. Application and results	35
2.5.1. Quartic Oscillator	35
2.5.2. Excited states of He-C ₂ H ₂	40
2.5.3. Computational details	42
2.6. Conclusions	42
2.7. Acknowledgments	43
3. MICROSCOPIC SUPERFLUIDITY IN ⁴ HE CLUSTERS STIRRED BY A ROTATING IMPURITY MOLECULE	46
3.1. Abstract	46
3.2. Publication	46

4. MICROSCOPIC SUPERFLUIDITY OF HCN DOPED ^4HE DROPLETS	59
4.1. Abstract	59
4.2. Introduction	59
4.3. Genetic algorithm	61
4.4. On the fly computation of nodal hypersurfaces	62
4.5. Epochal GA-DMC	64
4.6. Computer methodology: fine grained parallel genetic algorithm	65
4.7. Reduced dimensionality models	66
4.8. Potential energy surface (PES)	67
4.9. Results and conclusions	67
4.10. Acknowledgments	69
5. RENORMALIZATION OF THE ROTATIONAL CONSTANTS OF NH_3 SEEDDED IN SMALL ^4HE CLUSTERS	70
5.1. Abstract	70
5.2. Introduction	70
5.3. Hamiltonian	74
5.3.1. Nodal functions	75
5.3.1.1. Isotropic nodal functions	76
5.3.1.2. Adiabatic nodal functions	77
5.4. Importance sampling	78
5.5. Recrossing correction	79
5.6. Computational details	80
5.7. Results	80
5.8. Acknowledgments	83
6. SUMMARY	86
REFERENCES	93
APPENDIX	105
CURRICULUM VITAE	123

LIST OF FIGURES

Figure	Page
1.1. Flow diagram of the DMC algorithm	8
1.2. Flowchart of a binary genetic algorithm	14
1.3. Pressure-temperature phase diagram of ^4He	17
1.4. Reduced dimensionality model, bosons-on a- ring (BOAR).	20
1.5. Rotational spectrum of OCS in a beam seeded with ^4He	22
2.1. Scatterplot (small filled circles, red online) showing the location of several relatively high fitness energy clusters detected by the GA- DMC algorithm after the first 25 generations.	36
2.2. Contour plots of the wave functions for the state with energy, $E=6.55$; (a) accurate wave function, (b) a high fitness function individual from half-way through the calculation and (c) the converged GA- DMC estimate of the nodal surface for this state.	39
2.3. Contour plots of the wave functions for the state with energy, $E=9.551$; (a) accurate wave function, (b) a high fitness function individual from half-way through the calculation and (c) the converged GA- DMC estimate of the nodal surface for this state.	44
2.4. Density plots of the wave functions for the BOAS (a-c) and accu- rate (d) He- C_2H_2 state nominally labeled $ j, l \rangle = 1, 4 \rangle$ with total angular momentum $J = 3$	45
3.1. Bosons-on-a-ring model.	49
3.2. Effective rotational constant (B_{eff}) for a CO dopant as function of ^4He atoms (N)	51

3.3. Comparison of the actual ^4He -atoms-on-a-ring wave functions using the soft Gaussian barrier (left column) with the BF wave functions (right column) corresponding to the TG gas in the presence of an impurity molecule; $N = 2$ (top row) and $N = 5$ (bottom row)	55
3.4. Floquet eigenvalues ϵ_α (where α labels the Floquet mode [142]) as a function of the ratio ω_{eff}/ω_0	57
4.1. Energy splittings ($2B_{eff}$) for a -type, $J = 1-0$ rotational transitions as a function of the number of ^4He atoms (N).	68
5.1. Renormalized rotational constants (RC) for NH_3 as a function of the number, N , of ^4He atoms.	82

LIST OF TABLES

Table	Page
3.1. Energy splittings ($\Delta E = 2B_{\text{eff}}$) between the ground state and the lowest excited state in the a -type series of the $\text{CO-}^4\text{He}_N$ cluster. Units are cm^{-1}	50
5.1. Ground and selected $J = 1$ excited state energies and standard errors for the $^4\text{He}_N\text{-NH}_3$ clusters considered for $N = 1, 20$. The rotational constants used are $B_0 = 9.945 \text{ cm}^{-1}$, $C_0 = 6.229 \text{ cm}^{-1}$. Energies are from the DMC computations.	84
5.2. Ground and selected $J = 1$ excited state energies and standard errors for the $^4\text{He}_N\text{-NH}_3$ clusters considered for $N = 1, 10$ using the “fudged” rotational constants $B_{\text{fudged}} = 0.9945 \text{ cm}^{-1}$, $C_{\text{fudged}} = 0.6229 \text{ cm}^{-1}$. Energies are from the DMC computations.	85

CHAPTER 1

INTRODUCTION

The science of ultra-cold droplets of bosonic atoms, for example ^4He or *para*- H_2 , seeded with impurity molecules has been and continues to be of great experimental and theoretical interest. The two articles that lay claim to having started the field come from the groups of Giancinto Scoles [1] and Peter Toennies [2] and are well on their way to becoming citation classics. A long list of molecules doped into ^4He droplets have been studied, both experimentally and theoretically [3–14]. Novel and challenging experiments have been and continue to be done in which the ^4He droplet is used as an ultra cold (≈ 0.38 K) matrix to study other species, including many that had previously been studied only in the gas phase [3, 15–19]. These droplets may contain as few as 2 [20–27] ^4He atoms or 1000s [4] of atoms in the case of nanodroplets. A partial list of the systems studied include: water [28–31], water anion clusters [32], ammonia clusters [28, 33–36], ammonia water clusters [37], hydrated HCl clusters [38–41], acetic acid clusters [42], and atomic and ionic dopants in helium clusters and films [43]. Nanodroplets of ^4He have also been used as nanocryosats [1, 20, 44] to form exotic species and aggregates, as chemical nano reactors [30, 45–48] to isolate otherwise unstable reaction intermediates and as matrices to study the spectroscopy of molecules, including large organic molecules, ions and nano structures [5, 39, 49–51] and for surface deposition [52]. New highly sensitive spectroscopic techniques have also been developed based on the unique characteristics of ^4He droplets; for example, an infrared (IR) spectroscopic method that analyses molecular ions by capturing them in ^4He nanodroplets [53]. Eventually, it is hoped, this new spectroscopic techniques will allow for better studies into cold biologically important molecules and clusters important to aerosol formation in the atmosphere.

The question of microscopic superfluidity has been tackled in some of these studies, most often in regards to the ^4He clusters, but recently in studies of bosonic para- H_2 as well. The physics of bulk superfluidity has been attributed to both Bose-Einstein condensation (BEC) and superfluidity. BEC is a result of Bose statistics which occur due to the macroscopic occupation of the same quantum state, whereas superfluidity is a hydrodynamic phenomenon characterized by zero viscosity and frictionless flow.

The physics of microscopic superfluidity, on the other hand, is less well known. While superfluidity is fundamentally a microscopic effect and no thermodynamic limit is necessary, it is, nevertheless, remarkable that the signature of microscopic superfluidity has been reported for doped droplets containing as few as 4 ^4He atoms. The first signs of microscopic superfluidity were observed in early “Andronikashvili-type” experiments. In these early experiments, spectra of SF_6 and OCS dopants [2, 54] in ^4He droplets revealed sharp rotational features, characteristic of free (gas phase) molecular rotation, but with renormalized (reduced) rotational constants. This behavior, to varying degrees, seems to be the norm for molecules doped to a ^4He solvent.

Microscopic superfluidity is often described using the language of the two-fluid theory of Tisza and Landau [55–59] in which the helium density around the dopant cluster consists of a normal and a superfluid fraction. In path integral Monte Carlo (PIMC) calculations, microscopic superfluidity is characterized by the existence of macroscopic exchange paths winding across unit cells. Studies of small CO doped para- H_2 droplets [55, 60], using a PIMC coupled worm algorithm [55, 60], done to determine the normal and superfluid fractions of the bosonic solvent, observed microscopic superfluidity in as few as 6 para- H_2 molecules. Although theoretical and experimental studies have observed the phenomenon of microscopic superfluidity in small clusters of bosonic molecules, it is still difficult to picture

how superfluidity can occur with so few molecules, in some cases as few as 4 - 6 ^4He atoms [21, 61, 62] or 6 para- H_2 molecules [60].

The core issue in the studies outlined in subsequent chapters is the mechanism by which the helium density decouples from the rotational motion of the molecular dopant. In practice, the onset of microscopic superfluidity is characterized by a nonclassical increase in the effective rotational constant (B_{eff}) with increasing cluster size. In $^4\text{He}_N\text{-CO}$ clusters, for example, where N denotes the number of ^4He atoms in the cluster, high resolution d-millimeter wave studies [21, 25] have been able to trace the onset of microscopic superfluidity in clusters containing up to $N = 10$ ^4He atoms.

There are a large number of published reviews that describe the many experimental and theoretical advances and challenges in the field [3–14]. It is evident, from these studies, that one of the great challenges of examining these systems, for computational studies in particular, is how to perform accurate and fully quantum mechanical treatments on these fundamentally many-body systems.

One method employed, an alternative to the essentially statistical mechanics, finite temperature based PIMC approach, is to adopt a molecular view point to study the mechanics that lead to the decoupling of the doped molecule from the bosonic solvent. The Schrödinger equation gives the accepted description of microscopic phenomena at non relativistic energies. In fact, it would not be overstating it to say that solving the many-body Schrödinger equation, accurately, is one of the most important fundamental problems in physics and chemistry [63–65]. The solution of the time-dependent Schrödinger may be given as a linear superposition of stationary states in which the time dependence is given by a phase factor $e^{-iE_n \frac{t}{\hbar}}$, where E_n is the n^{th} energy level of the quantum system in question.

Whether dealing with systems composed of bosons or fermions the main problem in solving the Schrödinger equation accurately is this: how to increase the

number of particles without having the computer time spin out of control. One solution is to use quantum Monte Carlo (QMC) methods [63, 66–71] these include: variational Monte Carlo [70], diffusion Monte Carlo [18, 65, 70, 72], path integral Monte Carlo [73, 74], projection operator imaginary time Schrödinger equation (POITSE) [75, 76], and reptation QMC (RQMC) to study dopants in ^4He clusters, often with excellent agreement with the experimental results [21, 25, 55, 77–79]. Unlike most other conventional quantum chemical approaches, QMC methods can be made to scale roughly as the square of the system size [64, 65, 71, 80]. Most computational studies will therefore usually use variations of quantum Monte Carlo (QMC) methods [63, 66–71, 80]. QMC methods provide accurate solutions while scaling more slowly with the system [64, 65, 71, 80], in contrast to other quantum chemistry approaches which quickly become impractical, unless approximations are made, with increasing system size.

An example of a QMC method utilized in solving computational problems is the diffusion Monte Carlo (DMC) method. The DMC algorithm, utilizes imaginary time τ , replacing the time t with $i\tau$. The solution is given by

$$\sum e^{(-iE_n \frac{t}{\hbar})} \quad (1.1)$$

where $n = 0, 1, \dots, n$. The DMC algorithm is based on the observation that as the quantum system evolves through imaginary time, the ground state energy will be that of the longest lasting transient, with energy $E_0 < E_n$, where $n = 1, 2, \dots, n$. This means, essentially, that regardless of the initial state in which the system is prepared, one can determine both the ground state energy, E_0 , and the ground state wave function, Ψ_0 , by simply allowing a long enough evolution of the wave function in imaginary time.

The DMC method can be formulated in two ways. One formulation comes from the Feynman path integral solution of the time-dependent Schrödinger equation;

using path integrals to express the wave function as a multidimensional integral which can be evaluated by employing the Monte Carlo method. The second approach is based on the similarity between the imaginary time Schrödinger equation and a generalized diffusion equation. In this method, the diffusion Monte Carlo (DMC) algorithm exploits the similarity between the diffusion equation, with a position dependent source / sink term - and - the Schrödinger equation in imaginary time (ITDSE). The ITDSE in integral form is given by:

$$\Psi(R', \tau + d\tau) = \int dR G(R \rightarrow R', d\tau) \Psi(r, \tau) \quad (1.2)$$

where $G(R \rightarrow R', d\tau) = \langle R' | e^{-d\tau \hat{H}} | R \rangle$ is the imaginary time Green function and \hat{H} is the Hamiltonian. Boson particles, ^4He atoms for example, will obey Boltzmann statistics and will have no nodes in the ground state. While the Green function is generally unknown, it can be approximated using a short time approximation [70] as:

$$G(R \rightarrow R', d\tau) \sim \prod_i^N \left(\frac{m_i}{2\pi d\tau} \right)^{\frac{3}{2}} \times e^{[-m_i \frac{(R'_i - R_i)^2}{2d\tau}]} \times e^{-[V(R) + V(R') - 2E_r] \frac{d\tau}{2}} \quad (1.3)$$

$V(R)$, in this case, is the total interaction potential between the N particles whose coordinates are R in the $3N$ -dimensional space and E_r is the reference energy. The first exponential in Eq. (1.3) generates a diffusive random walk. The second exponential is simulated by a birth/death process with E_r as the “reference” energy.

In practice, DMC simulations will often employ importance sampling [72, 87, 91, 92], where a trial wave function, Ψ_T , is used to guide the walk. Implementing importance sampling improves the efficiency of the DMC algorithm and also increases the precision of the computed energies [70]. Additionally, importance sampling prevents the unphysical dissociation of clusters containing large number

of ^4He atoms. Implementing importance sampling results in a diffusion like equation for the mixed function $f(R, r_i) = \Psi(R, r_i)\Psi_T(R, r_i)$ where R and r_i are the molecular and atomic coordinates, for the doped impurity and the bosonic solvent respectively. Additional drift terms - quantum forces - are introduced into the diffusive process which guide the walkers to regions of high density [72].

Algorithms to evaluate the path integral representation and those solving the diffusion-reaction equation obeyed by the wave function yield essentially the same formulation of the DMC method. The formulation one chooses to use depends mainly on one's expertise. The path integral method requires knowledge of the corresponding formulation of quantum mechanics, whereas the formulation of the DMC method based on the diffusion-reaction equation requires familiarity with the theory of stochastic processes.

The theoretical formulation of the DMC algorithm can be outlined as follows [93]:

1. The solution for the time dependent Schrödinger equation is expressed as a formal series expansion in terms of the eigenfunctions of the Hamiltonian. The real time, t , is transformed to imaginary time, τ , by replacing $t \rightarrow i\tau$. The solution of the resulting imaginary time Schrödinger equation becomes a series of transients that, as $\tau \rightarrow \infty$, experience exponential decay. The longest lasting transient corresponds to the ground state (the state with the lowest possible energy) of the system.
2. The ground state energy and wave function are determined. The Monte Carlo method samples the wave function after each time step. An approximation of the wave function at each time step is given by the spatial coordinate distribution of the replicas involved in the combined diffusion and birth-death processes. The wave function will converge in imaginary time towards the time independent ground state wave function only if the origin

of the energy scale is equal to the ground state energy. A reasonable guess at the ground state energy is used as the starting point. This guess is then refined after each time step in which a diffusive replacement and birth-death process is applied to all particles at once. The initial estimate should eventually coverage to the desired ground state energy and the distribution of the particles converge to the ground state wave function.

The computational implementation of the DMC algorithm is shown in Fig. 1.1. The external data required is collected in the input block via a menu driven, interactive interface. To begin with one should select the quantum system on which the calculation is to be performed; this entails programming the right spatial dimensionality, d , and the potential energy, V . The other input parameter needed are as follows: (i) initial number of replicas (N_0), (ii) the maximum number of replicas (N_{max}), (iii) the seed value for the random number generators, (iv) the number of time steps to run the simulation τ_0 , (v) the value of the time step ($\Delta\tau$), (vi) the limits of the coordinates for the spatial sampling of the replicas (x_{min}, x_{max}) and, (vii) the number of spatial “boxes” (n_b) for sorting the replicas during their sampling. In the subsequent step, indicated by the “initialize replicas” block, a two dimensional matrix known as psips is initialized [93]. The first row of the psips matrix identifies the replicas between one and N_{max} ; the second column points to information regarding the replica and the other elements are used to store the coordinates of the replicas.

After initialization the algorithm then enters a loop consisting of the walk, branch and count blocks. In the walk portion of the loop, the replicas undergo a diffusion process. This is done by adding the value $\Delta\tau\rho$, where ρ is a random number and $\Delta\tau$ is one time step, to each replica. In the branching process, each diffusion step of the replica is subjected to a birth-death process. A variable m_n is calculated for each replica. If $m_n = 0$ the replica is killed by setting the corresponding existence flag to zero. If $m_n = 1$ the replica is left as is and if the

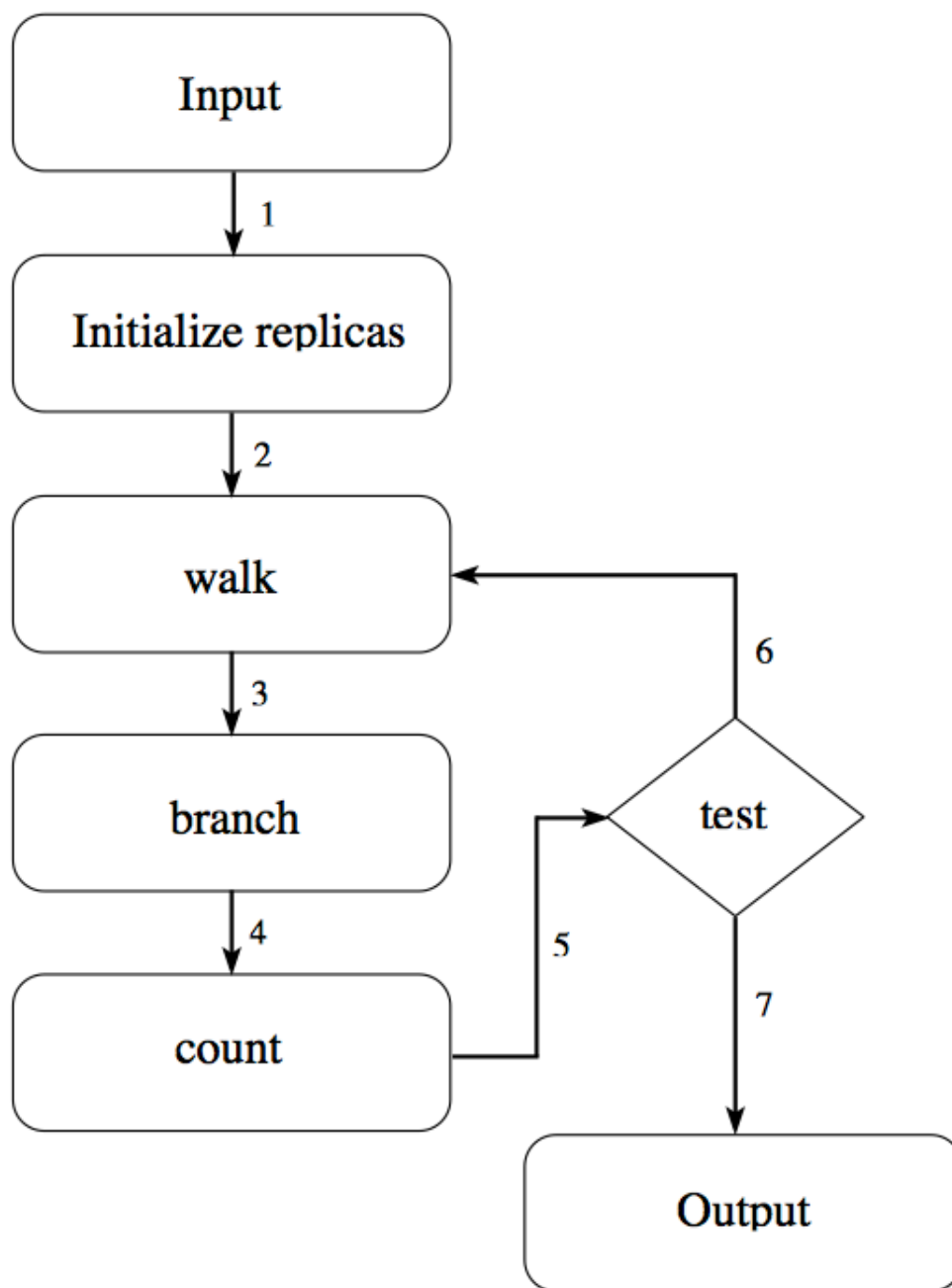


FIG. 1.1 Flow diagram of the DMC algorithm [93].

value of $m_n = 2$ the replica is duplicated. For $m_n = 3$ two identical copies of the replica are generated. The count block returns the ground state wave function of the system by counting the distribution of the replicas among the boxes n_b . The output block returns the results of the simulation. The results that are obtained are, (i) the average value of the reference energy $\langle E_R \rangle \approx E_0$, (ii) the standard deviation of the calculated average energy δE_r , (iii) the imaginary time evolution of $\langle E_R \rangle$ for the first τ_0 time steps and (iv) the normalized spatial distribution of the replicas.

Despite their many advantages, QMC methods come with an intrinsic problem that complicates their application to many systems: they only converge to the exact ground state energy of a many-body system if the wave function contains no nodes. In all other cases, i.e., for excited states or fermions, approximations must be made to solve the problem.

The total wave function is the product of the orbital and the spin wave function. In the case of bosons (particles with integer spins) the total wave function is symmetric with respect to any permutations of the particles while for fermions (particles with half integer spin) the total wave function is antisymmetric with respect to such permutations. This constraint determines the symmetry of the orbital portion of the ground state wave function for fermions but not for bosonic states. This means that the orbital ground state wave function of fermions will have nodes, i.e., regions with different signs. This is the origin of the “sign” problem that plagues the application of QMC methods to fermionic systems [66, 67, 69, 80–86]. One approach that is taken when applying QMC algorithms to fermions or excited states is to use the fixed node diffusion Monte Carlo (FNDMC) method [67, 70, 87]. In the FNDMC algorithm, a particular nodal topology is assumed for the trial wave function used to guide the calculation. The overall accuracy of the solution depends on the accuracy of the guiding wave function. If the assumed nodal topology is exact then the QMC algorithm will converge

to the exact numerical solution. It is therefore critical that we develop means of accurately determining the nodal hypersurfaces of many-body wave functions; this is in fact an active area of investigation [68, 81–86, 88–90, 90].

In fixed node diffusion Monte Carlo, the nodes of the guiding wave function are used to partition the space into pockets within which the wave function is either positive or negative [87]. Any walkers that cross a node are eliminated. The portion of wave function within each pocket contains the ground state solution of a fictitious particle contained in the pocket. This means then that the overall energy can be found by performing separate ground state calculations inside each pocket, yielding pocket energies for positive portions of the wave function, E_+ , and the negative portions of the wave function, E_- . Since the energy of the actual state must be the same inside each pocket, the resultant energies E_+ and E_- should be equal if the nodal hypersurface used is exact. Of course this means that one must either have prior knowledge of the nodal topology of the target wave function or have an effective means of refining the initial guess to resemble the exact nodal hypersurface.

There are a number of different methods that have been used to generate the nodal hypersurface for the trial wave function for use in FN-DMC computations; taking advantage of the symmetry in a complex to predict its nodal topology, for example. All the methods employed so far have had significant disadvantages to them. Symmetry, for example, is not always a viable option especially in the case of unknown highly complex wave functions. Bressanini and Reynolds [94], in fact, found unexpected symmetries in the nodes of several atoms and molecules which led them to speculate that in some cases the nodal hypersurfaces will have higher symmetry than the wave function. Other techniques such as the use of random forests of decision trees to classify nodal pocket [95, 96]; the use of self healing DMC in which the nodal hypersurfaces are successively improved as the

computation proceeds [81], and a direct optimization procedure [97] have also been used. The viability, ease and adaptability of these approaches remains to be seen.

In molecular physics, Buch et al. developed a systematic approach of nodal optimization [88]. This approach relies on the observation that the separate DMC calculations inside each pocket will yield the same energy if the nodal hypersurface used is exact. By optimizing the node to achieve equal energies in each node, they were able to obtain satisfactory results for the CO-H₂O complex [88] and also the water hexamer [89]. In addition to the energy constraint, they utilized one other optimization criteria: comparison of direction flux histograms. The derivatives of the wave function must be continuous across the node; therefore, the normalized local flux of the DMC walkers crossing a nodal surface in opposite directions will be equal for the exact node. The histograms were obtained by binning walkers that crossed the nodes in each direction. Then the histogram comparison was done by hand [88]. While effective in this particular case, there are number of valid arguments that can be raised against the use of directional histograms as an optimization criteria. First, it may not always be a viable option in the case of highly excited states with many different pockets. Second, the walkers crossing the nodal surface are driven by the Green function or propagator; however, we only have an approximate expression for the Green function. If one employs importance sampling with an accept/reject step in it in the DMC code, then as the time step approaches zero both the number of attempted node crossing per Monte Carlo step and the number of attempted nodal crossing per unit time goes to zero.

The first problem is easily solved. We simply perform two simulations in which the phase of the wave function is either positive or negative. If the nodal surface is correct, averaging over all the pockets in the positive phase and over all the pockets in the negative phase will produce equal total pocket energies, regardless of the number of nodal pockets involved. Solving the second problem was the basis of a large portion of this research project, i.e., the use of non-directional

histograms in a genetic algorithm diffusion Monte Carlo (GA-DMC) algorithm to optimize the nodal topography of a target wave-function.

The key idea for the project was to utilize a genetic algorithm to hone in on the nodal hypersurfaces of the target state within the DMC calculation. The genetic algorithm (GA) is a subset of evolutionary algorithms that model biological processes to optimize highly complex functions [98]. The algorithm allows a population consisting of many individuals to evolve under specified selection rules to a state that minimizes the cost function, i.e., maximizes the “fitness”. This method was developed by John Holland in the 1960s [99], and popularized by David Goldberg in 1989 who used it to solve a difficult problem involving the control of gas-pipeline transmissions [98]. Genetic algorithms may be used to find global extrema in high dimensional spaces. There are numerous advantages to using the genetic algorithm: (i) it optimizes with continuous or discrete parameters; (ii) it doesn’t require derivative information; (iii) it is well suited for parallel computers; (iv) it optimizes parameters with extremely complex cost surfaces and can jump out of a local minimum; (v) it provides a list of optimum parameters and, (vi) it can work with all types of data, e.g., numerically generated data, experimental data or even analytical functions. Another useful advantage of this method is that, as long as the problem can be encoded and the optimization criteria defined, the GA is easy to implement; mainly because the GAs are portable and require minimal interfacing between the GA part of the code and the intended application.

In the genetic algorithm, initially, a population of randomly chosen individuals is created and a fitness level assigned to each individual based on the user defined fitness function. The individuals each represent a possible solution to the optimization problem being studied. Each individual is evaluated against a user defined fitness function. The fitness function is specific to each problem. The next generation is then created by breeding (via recombination or mutation) only the

individuals that satisfied the criteria set by the fitness function. The new population is used in the next iteration of the algorithm and so on. After a certain predetermined number of generations the algorithm is terminated. If a satisfactory solution has not been found, the last generation may be used as the starting point for the evolution of further generations.

The optimization criteria, as stated previously, is user defined; often in the form of a fitness function that is systematically refined by the GA. Some examples of optimization criteria used involved the comparison of pocket energies obtained during separate DMC calculation [64, 88, 100, 101], comparative analysis of both directional histogram [100] and non-directional histograms [90, 102]. In most cases, the most computationally demanding step of the process is the evaluation of the fitness function. Evaluation of the fitness function usually involves performing several DMC calculations for each GA individual; computing the fitness function accounts for 99% of the computer time. It is therefore important to implement a computer methodology that maximizes computational efficiency. Using fine-grained parallel genetic algorithms does just that. In practice, the most important steps of the GA are (i) encoding a representation of the possible solution and (ii) defining a fitness function against which to test the individuals.

When encoding a representation of possible solutions to the problem, the goal is to map the topology of a candidate nodal surface onto a bit string of 0's and 1's. Since algorithms exist to convert numbers into bit string, encoding the representation then simply becomes encoding an arbitrary nodal surface by a set of parameters which are chosen by the GA. In general, a nodal wave function may be parameterized as $\Psi = \sum_n c_n \theta_n$, where the c_n are expansion coefficients and θ_n are a set of basis functions. The GA will refine the expansion coefficients, c_n , using the defined optimization parameters. Several different excited states may be represented by the same basis vectors, but with different coefficients; consequently, multiple maxima in the fitness function will exist. Picking the c_n directly will

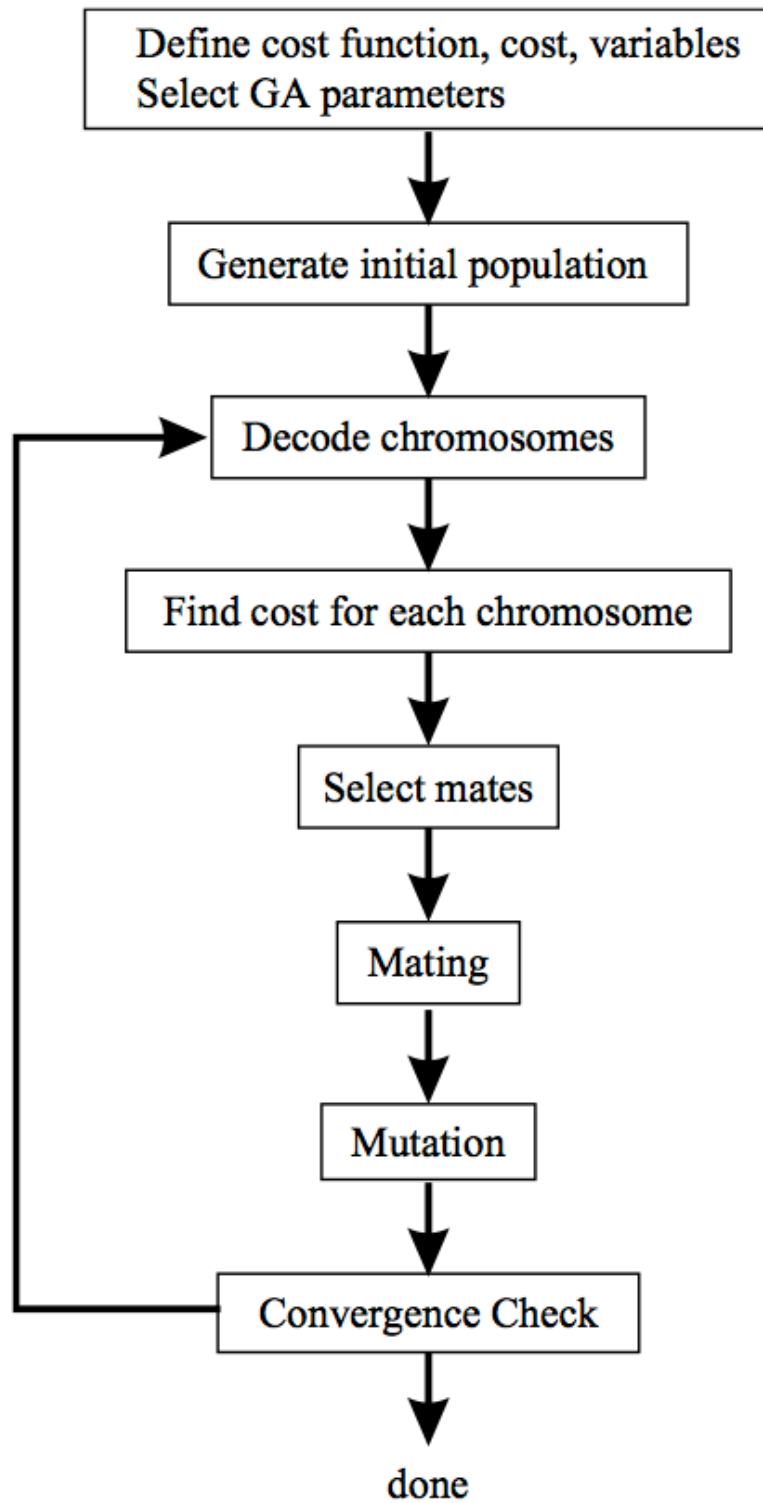


FIG. 1.2 Flowchart of a binary genetic algorithm [98].

cause the GA to oscillate between the different excited states consistent with the parameterized nodal surface. In order to tighten the target range, two approaches can be taken: (i) modify the fitness function so that only states in a given energy interval are found, or (ii) bias c_n to target the state of interest.

The fitness function criteria used is specific to each problem. In some studies [64, 100] the optimization criteria was based on the requirement that the separate DMC calculations performed inside each nodal pocket result in identical pocket energies if the node was exact. Additionally, comparison of the similarity between directional flux histogram, generated by binning walkers crossing the node on either side, was done. In fixed node diffusion Monte Carlo (FNDMC), walkers that cross nodal surfaces are eliminated. Since the wave function must be continuous across the nodes, the rate of elimination of walkers crossing the node must be the same [88]. An alternative optimization criteria was proposed by Lüchow et al. [90, 102]. It argues that if the true wave function is governed by $\hat{H}\Psi = (\hat{T} + V)\Psi = E\Psi$ where \hat{T} is the kinetic energy operator, then the functions Ψ_T , $\hat{T}\Psi_T$ and $\hat{H}\Psi_T$ will all have the same nodal hypersurfaces when the trial wave function, Ψ_T , has the same node as the true wave function, Ψ . This lead to an approach based on minimizing the distances between the nodal hypersurfaces of Ψ_T , $\hat{T}\Psi_T$ and $\hat{H}\Psi_T$. The procedure outlined by Lüchow et al. [90, 102] derived explicit expressions for the distances between the nodal hypersurfaces. The feasibility of this approach, however, depends on the hypersurfaces being (i) close to each other and (ii) locally parallel. This approach is also complicated by a number of other factors: (i) while Ψ_T and $\hat{H}\Psi_T$ all have nodes in common when Ψ_T is an eigenfunction, it is possible for $\hat{T}\Psi_T$ to have additional nodes and, (ii) it is also possible that there will be functions that exist that, though not eigenfunctions, are such that $\hat{H}\Psi_T$ and Ψ_T have nearly identical nodes.

We developed a new algorithm that avoids many of the problems of the Lüchow et al. method. In this new approach, the GA generates a random population of

trial wave functions based on a suitable parametrization of the node. For each Ψ_T a new function $\Xi_T = \hat{H}\Psi_T$ is formed. Two separate FNDMC calculations are performed using the node defined by Ψ_T . The calculations correspond to the positive and negative regions of the wave function. This will yield two pocket energies E_{Ψ}^+ and E_{Ψ}^- . The previous step is repeated using Ξ_T instead of Ψ_T . This yields two new energies E_{Ξ}^+ and E_{Ξ}^- . During the calculations, flux histogram of walkers crossing the nodal surface of Ψ_T and Ξ_T , independent of direction, are computed. If Ψ_T is an exact eigenfunction then all the pocket energies and the histograms generated will be identical. The goal is to use the GA to iterate to a Ψ_T which most nearly fulfills this criterion. The fitness function is then constructed by requiring near equality of the pocket energies with small standard deviations; minimizing the standard deviations between the energies E_{Ψ}^+ , E_{Ψ}^- , E_{Ξ}^+ and E_{Ξ}^- and minimizing the differences between the flux histograms. The multidimensional histogram comparison is done automatically [100, 101].

To test the viability of this method the GA-DMC algorithm was applied to the calculation of the excited states of a coupled quartic oscillator and excited states of the He-C₂H₂.

The GA-DMC algorithm, once the viability was established, was utilized in computational studies of the phenomenon of microscopic superfluidity. The weak van der Waals potential between ⁴He atoms and the fact that they are bosons have a dramatic influence on their properties. ⁴He is one of a very short list of substances that does not solidify even at the lowest temperatures, i.e., at temperatures of 0 K. Instead of a triple point, usually found in most substances, ⁴He has a λ -line connecting the points marked by λ ($P\lambda = 0.05$ bar, $T\lambda = 2.18$ K) and λ' in Fig. 1.3 which separates the normal liquid (He I) from the superfluid (He II).

While there have been numerous experimental and computational studies of macroscopic superfluidity, studies into the manifestations of microscopic superfluidity have been fairly recent. In 1992, Scoles et al. observed unusually sharp,

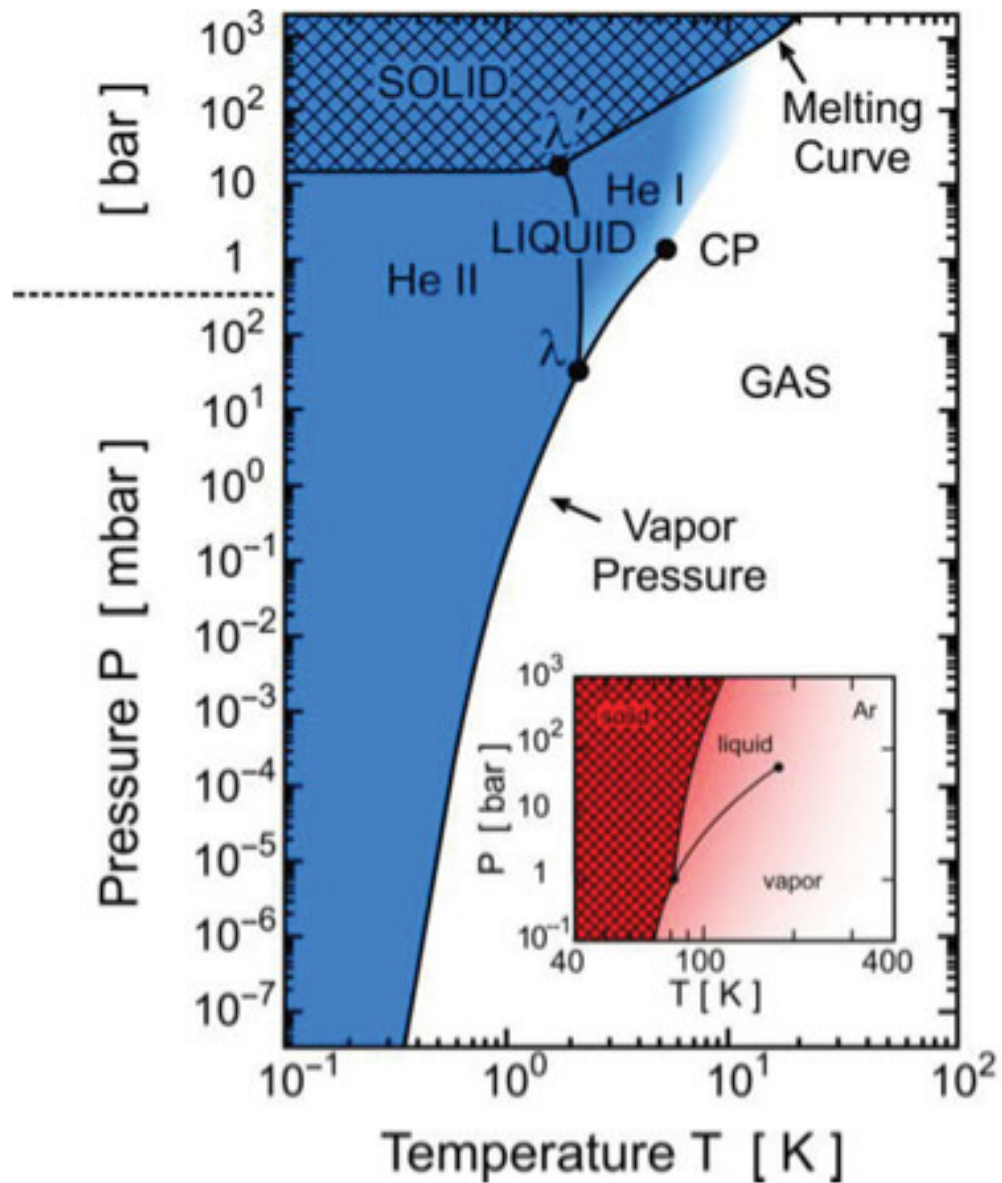


FIG. 1.3 (color online). Pressure-temperature phase diagram of ^4He . The inset shows the phase diagram for argon which has a triple point typical to most other substances [62]. Figure can also be found online at www.tandfonline.com.

infrared spectral features of the SF₆ molecule and SF₆ dimer attached to ⁴He droplets [1] and later studies by Toennies et al. [54] on the same system revealed a complete set of rotation lines. These results indicated that the dopant molecules were rotating almost freely inside the helium solvent. Since then other molecules seeded into ⁴He clusters have shown similar spectral features indicating that the seeded molecule had decoupled from the boson solvent [4, 7]. Experimentally, decoupling is signaled by the appearance of sharp, free-molecule-like, rotational lines in the spectra. This process of decoupling has been attributed to the onset of microscopic superfluidity and in some ⁴He-dopant complexes has been observed for as few as 4-6 helium atoms [21, 25, 103]. In computational studies, microscopic superfluidity is inferred from the nonclassical turnaround and subsequent increase in the effective rotational constant (B_{eff}) of the dopant as the number of ⁴He atoms (N) is increased. Similar observations have been made for *para*-H₂ cluster [55].

PIMC calculations have shown that in clusters with decoupled dopant molecules superfluid and normal fluid components coexist [55]. This complies with the two-fluid model of superfluids set out by Tisza and Landau [56]. In a PIMC study of $p-(H_2)_N$ -CO clusters the superfluid fraction was observed to decline from about 95% at $N = 1$, to roughly 82% at $N = 6$ followed by an increase essentially to 100% for $N > 10$. These results are similar to those found experimentally for B_{eff} of $N < 10$ ⁴He atoms. While the PIMC method can simulate essentially all the properties of superfluid ⁴He it does so by projecting the system onto a classical analogy. In essence, the quantum mechanics behind decoupling are not studied. The main goal of this study then is to examine, quantum mechanically, how decoupling of the molecule occurs from the bosonic solvent at 0 K.

Complexes of helium clusters seeded with impurity molecules have high quantum many body dynamics that make it difficult to achieve a qualitative understanding of the observed effects. In most cases, simulations done using simple

models of the system can provide insight into the properties of the system of interest. The results attained can then be compared against more computationally demanding simulations once a first principal treatment of the system has been done. Finding a model that simplifies the computational calculations while still capturing the physics of the system is essential.

Theoretical studies have shown that a one-dimensional (1D) gas of impenetrable bosons, known as a Tonks-Girardeau (TG) gas [104–106], constrained to a ring of finite circumference exhibits microscopic superfluidity. It has a critical velocity below which the system is hard to stir and a vanishing drag force. Taking advantage of this property, we introduce reduced dimensionality models to investigate the mechanism that leads to decoupling of the molecule from the bosonic solvent. In this reduced dimensionality model, the ^4He atoms are confined to a ring as shown in Fig. 1.4. This model is referred to as bosons-on-a-ring (BOAR). The BOAR model, originally conceived to simplify the search for nodal surfaces, is similar in some respects to Lehmann’s “toy” Hamiltonian which consists of two interacting rigid rings, one of which simulates the molecule and the other the ^4He atoms [107]. In the “toy model” the molecule is treated as a rigid planar rotor with moment of inertia I_1 ; the orientation of the molecule is given by θ_1 . The ^4He solvent is treated as a ring of N helium atoms that form another rigid planar rotor with moment of inertia I_2 and with orientation given by θ_2 [107].

As noted earlier, the phenomenon of free rotations is often designated as a manifestation of microscopic superfluidity. Fig. 1.5 shows the change in the measured rotational energy constant B ($B = \frac{\hbar^2}{2\pi I}$), where I is the moment of inertia for end-over-end rotation versus the number of helium atoms. The effective rotational constants of molecules embedded in ^4He droplets, B_{He} , once microscopic superfluidity is attained, is smaller than that of the free molecule, B_{gas} . For example, for the SF_6 molecule the renormalized rotational constant B (which is analogous to B_{He}) is approximately one third of its gas phase value B_{gas} (or B_0).

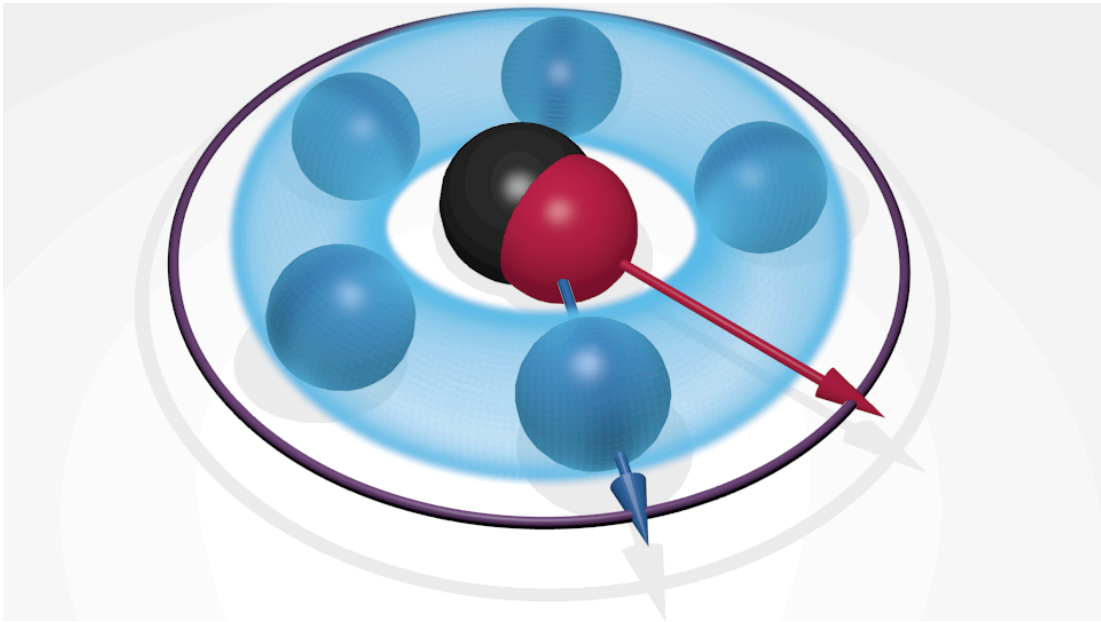


FIG. 1.4 (color online). Reduced dimensionality model, bosons-on a- ring (BOAR). The ⁴He atoms (blue) are confined to revolve on a ring of radius R_0 measured from the center of mass of the CO molecule (black/red). The molecule is pinned at the origin and rotates in the plane of the ring. The azimuthal angles of the molecule and the i^{th} ⁴He atom are θ and ψ_i , respectively.

This behavior seems, to varying degrees, to be the norm for molecules seeded into ⁴He nanodroplets [4].

The extent of renormalization can be expressed as $\Delta = \frac{B}{B_0}$. The extent of renormalization of the gas phase constants fall into two categories [4, 7, 108]. Effective rotational constant of heavy molecules ($B_0 < 0.5 \text{ cm}^{-1}$) in ⁴He are about a factor of three smaller than those in the gas phase; while those of the light rotors ($B_0 > 1 \text{ cm}^{-1}$) are only a few percent smaller than the gas phase rotational constants. Light rotors tend to have a small renormalization because of their large rotational constants. These large rotational constants, in effect, average the interaction potential so that the rotor appears to the ⁴He atoms to have a potential that is almost spatially isotropic. Therefore, the angular momentum transfer between the helium atoms and the rotor is relatively ineffective. In the case of a completely isotropic potential the angular momentum quantum numbers

of the molecule and the atom are conserved separately. For heavy rotors, a fraction of the helium density is able to follow the rotor adiabatically, i.e., there is a rigid coupling of the molecular rotation to the local non-superfluid helium density that is induced by molecular interaction [9, 109]. Theoretical calculations have shown that the local helium density cannot adiabatically follow the motion of the rapidly rotating light molecule [9, 110]. It is the dragging of the helium density which leads to the relatively large renormalization observed for heavy rotors.

While most of the light and heavy rotors follow the renormalization trends stated in the previous paragraph there have been molecules that have not behaved as expected. The renormalization constant observed for the HF molecule, for example, was larger than calculated for HCl and HBr, despite the fact that HF has a much larger gas phase rotational constant than the other two molecules [111]. This has been attributed to the slightly stronger anisotropy of the He-HF intermolecular potential. The extent of renormalization is 0.98 for HF, ~ 1 for HBr and ~ 1 for HCl. The relative effects of the molecular anisotropy in this series of molecules, though apparent, is relatively weak in comparison to the renormalization induced by the size of the rotation constants.

Another important consideration in the extent of renormalization of the rotational constant is the rate at which the renormalization achieves its saturated value (the nanodroplet limit) as a function of the number of ^4He atoms. Saturation has been observed to occur with as few as $N = 8$ ^4He atoms [9, 112]. This observation is in fact what engendered the adiabatic following model. In adiabatic following the ^4He atoms are able to respond immediately to the motion of the molecule which, in effect, carries a “coating” of ^4He density along with it. The molecule coated with the ^4He density experiences a much more isotropic interaction with rest of the solvent as N is increased. Once the coating is completed, saturation is expected to occur relatively fast as a function of N . In large rotors, as there is little to no adiabatic following, we consider the (hypothetical) limit in which the

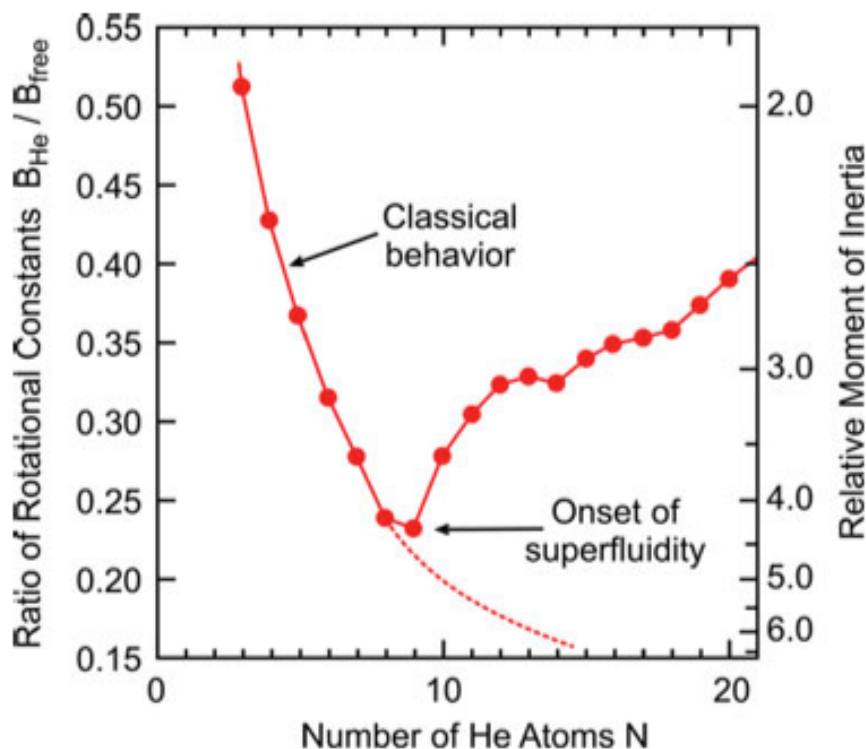


FIG. 1.5 (color online). Rotational spectrum of OCS in a beam seeded with ^4He . Rotational energy constant of OCS seeded in ^4He beam is plotted as a function of the number of attached ^4He atoms. The moment of inertia relative to the free molecule is plotted on the left ordinate [62]. Figure can also be found online at www.tandfonline.com.

potential is isotropic, known as the isotropic binary complex (IBC). At this limit there is no possibility of angular momentum exchange between the molecule and the solvent atoms and so saturation is reached immediately. This suggests that light rotors will have a relatively fast approach to the nanodroplet limit due to fast averaging of the potential. This was observed in the studies of HF, HCl and HBr [113] and CH_4 [114] seeded into ^4He droplets where saturation was attained in the first solvation shell.

The NH_3 molecule, a light rotor ($B_0 = 9.945 \text{ cm}^{-1}$) seems to behave rather unusually. Behrens et al. [33] measured a renormalization constant $B = 7.5 \text{ cm}^{-1}$ which represents a 25% reduction in B_0 . Whereas, more recently, Slipchenko and

Vilesov [35] and Suárez et al. [115] found only a 3% - 5% reduction in B_0 , which is much closer to the theoretical prediction. The disparity in the Behren et al. study has been attributed to poor spectral resolution in the experiment. This seems to be supported by a recent theoretical study by Viel et al. [116] which finds a much smaller blueshift of the ν_2 mode than Behrens et al. which is consistent with the results of Slipchenko and Vilesov and Suárez et al. . It is still interesting to study the quantum solvation dynamics of NH_3 in a ^4He cluster to confirm or disprove these conflicting results and also, perhaps more importantly, to gain further insight into the renormalization of rotational constants.

This dissertation deals with the investigations into (i) the viability of the GA-DMC algorithm, (ii) the phenomenon of microscopic superfluidity as observed in $^4\text{He}_N\text{-CO}$ and $^4\text{He}_N\text{-HCN}$ clusters, and (iii) renormalization of the rotational constants of NH_3 molecule seeded into a ^4He droplet. It is organized as follows:

Chapter 2 deals with finding nodal surfaces on the fly within a DMC calculations using the genetic algorithm. A novel method of defining the fitness function is studied; one that relies on minimizing the difference between the nodal functions of the guiding wave functions, Ψ_T , and $\hat{H}\Psi_T$, where \hat{H} is the Hamiltonian. The GA optimizes the parameters that define the trial wave function. The viability of this approach is tested by applying the GA to elucidating the nodal hypersurfaces of several excited states of a non-integrable two-dimensional quartic oscillator and the excited states of the $\text{He-C}_2\text{H}_2$ complex. The results obtained show that combining the GA to FNDMC calculations can be an effective method of locating or refining the nodal surfaces of a wave function on the fly.

Chapter 3 outlines the method and the results of a study of the microscopic superfluidity in ^4He clusters stirred by a rotating impurity molecule. The effective moment of inertia of a CO impurity molecule doped into $^4\text{He}_N$ clusters and $p\text{-(H}_2\text{)}$ solvent clusters initially increases with increase in cluster size (N) and then has a non classical decrease at $N = 4$ for the $^4\text{He}_N$ clusters and $N = 6$ for the $p\text{-(H}_2\text{)}$

solvent clusters which suggests molecule-solvent decoupling and a transition to microscopic superfluidity. However, the mechanism that leads to this decoupling is not understood. To investigate this we employ a one dimensional model in which the ^4He atoms are confined to a ring. This model captures the physics of the system. Results obtained suggest that decoupling happens primarily due to boson solvent-solvent repulsion. Furthermore, the results obtained from the DMC and basis set calculations suggest that the system can be modeled as a Tonks-Girardeau gas which then allows for the N -particle time-dependent Schrödinger equation to be solved directly. Computations of the integrated particle current reveal a threshold for stirring and current generation that is indicative of superfluidity.

Chapter 4 also deals with microscopic superfluidity but in this case with HCN as the dopant molecule in ^4He clusters. Once again, reduced dimensionality models are used to study the mechanism of microscopic superfluidity: the one dimensional model in which ^4He atoms are confined to a ring, bosons-on-a-ring (BOAR) and its three dimensional counterpart, bosons on a sphere (BOAS) where the ^4He atoms are allowed to move around a sphere. The results show an initial decline in the effective rotational constant B_{eff} and subsequent rise at $N = 4$, indicating an onset of microscopic superfluidity. The data obtained also suggests that the decoupling of the HCN molecule from the ^4He solvent clusters was due to solvent-solvent repulsive effects.

Chapter 5 discusses the solvation dynamics of NH_3 molecule seeded into a droplet of ^4He containing $N = 1-25$ ^4He atoms studied using the diffusion Monte Carlo method for the ground state calculations and the fixed node diffusion Monte Carlo method for excited state calculations. The investigation centers around the $|0011\rangle$ states using anisotropic nodes. The accurate rotational constants ($B_0 = 9.945 \text{ cm}^{-1}$, $C_0 = 6.229 \text{ cm}^{-1}$) and “fudged” versions of the rotational constants ($B_{fudged} = 0.9945 \text{ cm}^{-1}$, $C_{fudged} = 0.6229 \text{ cm}^{-1}$) of the molecule are used in the simulations. The reduction in B_0 calculated using the accurate rotational constants

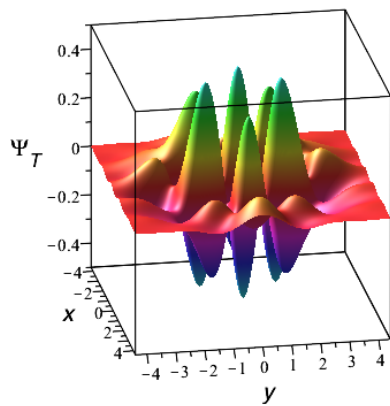
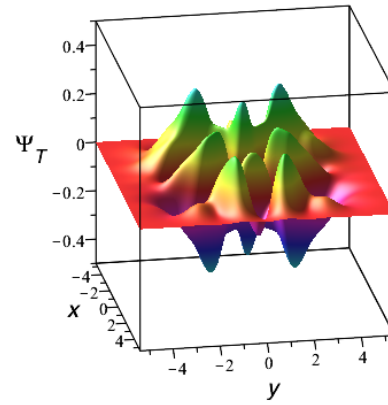
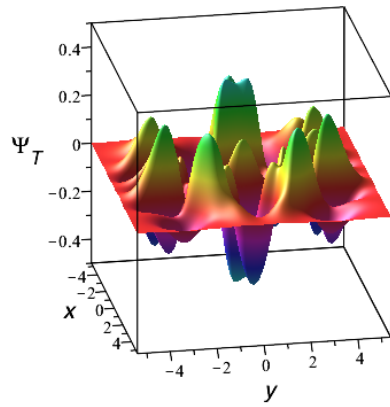
for the ammonia molecule for the $|0011\rangle$ state, about 34% , is much higher than expected and requires further investigation. The fudged rotational constants were in an indeterminate range between the light and heavy rotors. While both show a reduction in the renormalization constants the simulations done with the fudged rotational constants experience a slightly smaller reduction than those done using the accurate rotational constants. This may be attributed to the importance of molecular anisotropy versus the size of larger rotational constants in molecules whose rotational constants fall in an intermediate regime.

Chapter 6 provides a summary of each of the studies presented and any future work that needs to be performed.

CHAPTER 2

ON THE FLY NODAL SEARCHES IN IMPORTANCE SAMPLED,
FIXED-NODE DIFFUSION MONTE CARLO USING A PARALLEL,
FINE-GRAINED, GENETIC ALGORITHM

2.1 Graphical abstract



2.2 Abstract

A method of finding nodal surfaces on the fly in importance-sampled, fixed-node diffusion Monte Carlo calculations is described. The procedure relies on minimizing the difference between the nodal functions of the guiding wave function, Ψ_T , and $\hat{H}\Psi_T$, where \hat{H} is the Hamiltonian. This is done by allowing the trial wave function to depend on a set of parameters whose values are then optimized using a parallel genetic algorithm (e.g., the Pikaia code developed in astrophysics). Application is made to the calculation of several excited states of a non-integrable two-dimensional quartic oscillator and to excited states of the He-C₂H₂ complex.

2.3 Introduction

Solving the many-body Schrödinger equation *accurately* is a fundamental problem in physics and chemistry [63–65]. Although progress is being made in treating ever larger systems, most quantum chemistry methods [117] quickly become impractical unless approximations are made. Quantum Monte Carlo (QMC) methods are an alternative which can provide accurate solutions while scaling more slowly with system size [64, 65, 71, 80]. These advantages, coupled with recent advances in computational power, have resulted in QMC approaches becoming more widely used, for example, in materials science [63, 81] and molecular physics [15–19, 29, 65, 118–120].

Despite their advantages, QMC methods converge to the exact ground state of a many-body wave system only if the ground state wave function is node-free. This is the origin of the “sign” problem which complicates applications of QMC methods to fermionic systems [66, 67, 69, 80–86]. A similar difficulty arises in the computation of excited states which always contain nodes. The most common way to apply QMC approaches to states containing nodes is to use the fixed-node method [67, 70, 87].

In practical applications of the fixed-node version of the diffusion Monte Carlo (FNDMC) method [64, 65, 69, 70, 80], any DMC walkers (replicas) that cross a predetermined nodal hyper surface are eliminated. That is, the nodes of the trial N-body wave function partition the configuration space into pockets within which the wave function has either a positive sign or a negative sign. The portion of the wave function lying inside each pocket can be considered to be the ground state solution of a fictitious particle contained in that pocket. This allows the energy to be found by performing a separate *ground state* DMC calculation inside each pocket, i , here denoted E_+^i or E_-^i , where the $+$ and $-$ subscripts indicate the sign of the wave function inside a given pocket. Because the energy of the actual state must be the same inside each nodal pocket the separate DMC calculations inside all of the nodal pockets will yield the same energy if the nodal hyper surface used is exact. Obviously, this is a difficult problem because one must know in advance the nodal topology of the unknown state being sought. For this reason, finding nodal hyper surfaces of many-body wave functions is an active area of investigation [68, 81–86, 88–90, 102].

Various procedures, including guessing, have been used to generate nodes for the fixed-node procedure [68]. Symmetry can sometimes be used to determine the nodal topology but this is obviously not possible in general [94]. Lester and co-workers have attempted to describe and classify nodal pockets using machine learning techniques such as random forest of decision trees [95, 96]. More recently, several attempts to determine or improve the nodal hyper surface on the fly have been described including self-healing DMC [81, 90, 97, 102].

In molecular physics, Buch and co-workers developed a systematic approach that relies on the observation that separate DMC calculations inside each of the nodal pockets will yield the same energy if the nodal hyper surface used is exact [88, 89]. We have recently developed an automated version of this procedure in which the search for nodes is treated as an optimization problem that is solved

using a *genetic algorithm (GA)*, on the fly, i.e., within the DMC computation itself [100, 101, 121]. Essentially, the nodal surface is optimized such that the normalized local flux of DMC walkers crossing the surface in opposite directions are equal, as are the pocket energies. To impose these conditions, *directional flux histograms* are computed by performing separate DMC computations on each side of the node. By adjusting parameters in the assumed nodal hyper surface until (i) $E_+ = E_-$ and until (ii) the flux histograms in both directions are sufficiently similar, convergence was achieved.

In this letter we describe an alternative approach; rather than requiring equal fluxes of walkers crossing the assumed nodal surface in opposite directions, a genetic algorithm (GA) is used to minimize the difference between the nodal functions of the guiding wave trial, Ψ_T and the function $\hat{H}\Psi_T$ where \hat{H} is the Hamiltonian. This is done by allowing the trial wave function to depend on a set of parameters whose values are then refined using a GA.

This Letter is organized as follows: Section 2 describes the nondirectional histogram procedure and explains how this can be used to generate optimization criteria for use in a GA. Application is made in Section 3 to a model coupled oscillator problem and to excited state of the He-C₂H₂ complex. Comparison is made with accurate basis set calculations. Conclusions are in Section 4.

2.4 Genetic-algorithm diffusion Monte Carlo

Comprehensive reviews of the DMC algorithm, and its various implementations, are available [64, 65, 69, 70, 80] so only a brief overview of the method will be provided.

The DMC approach exploits the similarity between the diffusion equation - augmented by a position dependent source/sink term - and the Schrödinger equation in imaginary time (ITDSE) $\tau = it$. In practice, DMC simulations often implement importance sampling [72, 87, 91, 92] in which a trial wave function

- here denoted as Ψ_T - is used to guide the walk. Using a “good” trial wave function speeds up convergence, reduces statistical errors and may, in practice, be essential to prevent the unphysical dissociation of weakly bound clusters [72, 112]. Frequently, variational Monte Carlo (VMC) calculations are first done to generate trial wave functions.

Extending the DMC method to excited states, or ground states of many-fermion problems, is a difficult problem. This is because, in DMC, the wave function, Ψ , rather than $|\Psi^2|$, is the probability distribution of the diffusive walk; if the wave function has nodes then the underlying probability distribution is clearly not positive everywhere. To deal with this problem, the fixed-node method is often used in which any DMC walkers that cross a predetermined nodal hypersurface are eliminated. If the nodal hypersurface for a particular state cannot be obtained in advance, for example, by symmetry argument or variationally, then the DMC calculation for that state cannot proceed. A desirable strategy is, therefore, to optimize the nodal surface on-the-fly, i.e., within the DMC calculation. The GA-DMC method described previously [100, 101] is one way to achieve this goal. Here we describe a refined optimization procedure within the GA-DMC method which more easily allows for importance sampling.

2.4.1 Genetic Algorithms

Genetic algorithms provide a way of finding global extrema in high-dimensional search spaces. An advantage of the method is that, provided a suitable fitness function and encoding of the problem is defined, the GA algorithm is easy to implement. This is because GA codes are portable and require tentatively little interfacing between the GA part of code and the intended application [122]. GAs can also be coupled with other artificial intelligence approaches, including pattern recognition methods and decision tree [96, 122–124].

In simulations using GAs, a population of “individuals” is allowed to interbreed and evolve to an optimal solution as governed by a particular fitness function. The fitness function is specific to the problem at hand. Each individual in the population is a representation (or chromosome) of a possible solution to the optimization problem - in this case a guess at the node. The individual is encoded as a string of binary bit (i.e., 0s and 1s). To start off, a population of randomly chosen individuals is created and a fitness level is assigned to each individual based on a user-defined fitness function. This constitutes the first generation. The next generation is formed by selecting individuals from the previous generation, based on their fitness, and then forming new individuals (“breeding”) by recombination and mutation. The new population is used in the next iteration of the algorithm and so on. The algorithm terminates after a certain predetermined number of generation. In the event that a satisfactory solution has still not been found, the last generation may be used as the starting point for the evolution of further generations. In practice, the two most important steps are (i) encoding a representation of a potential solution and (ii) defining a fitness function against which to test the individuals.

Typically, the most computationally demanding step of the process is the evaluation of the fitness function. In the present application this is also the case because it involves performing several DMC computations for each GA individual. In fact, essentially all the computer time is consumed in computing the fitness function. This suggests a parallel approach in which each GA individual is farmed out to a separate “slave” cpu (or cpu core) while a master cpu takes care of the GA-related operations. It is most natural to send one individual to each available core (or thread). This method is known as “fine-graining”. The parallel Pikaia genetic algorithm was used [125].

2.4.2 Nodal optimization

Recently, Lüchow and co-workers [90, 102] have proposed a new optimization criteria based on the observation that if the true wave function is governed by $\hat{H}\Psi = (\hat{T} + V)\Psi = E\Psi$ where \hat{T} is the kinetic energy operator and V the potential energy surface (PES), then the function Ψ , $\hat{T}\Psi$ and $\hat{H}\Psi$ will all change sign at the same places. This suggest an optimization scheme based on minimizing the distances between the nodal hyper surface of the trial wave function, Ψ , $\hat{T}\Psi$ and $\hat{H}\Psi$. The actual method suggested by Lüchow and co-workers [90, 102] is to derive explicit expressions for distances between the nodal hyper surfaces of the three functions using a multivariate Taylor series expansion. However, this relies on the hyper surfaces being (i) close to each other and (ii) locally parallel. This approach gave good results for several models as well as for realistic systems but it is quite complicated to apply in general. In particular, it will not necessarily be the case that the nodal hypersurface of of the functions Ψ , $\hat{T}\Psi$ and $\hat{H}\Psi$ will be close or parallel for any arbitrary trial wave function. A further problem is that, even for the exact wave function, the function $\hat{T}\Psi$ may have additional nodes beyond those it shares with Ψ and $\hat{H}\Psi$ (this is easily demonstrated using the one-dimensional (1D) harmonic oscillator as an example). It is also possible that Ψ , $\hat{T}\Psi$ and $\hat{H}\Psi$ have nearly identical nodes even for a poor choice of Ψ_T .

Here we propose an algorithm to converge to the actual nodal hypersurface of a given state within the DMC calculation:

1. A GA is used to generate a random population of trial wave functions having particular nodal structures (“individuals”). This requires a suitable parameterization of the node. In general, this will be a system ansatz, possibly similar to the procedure adopted in a variational Monte Carlo (VMC) calculation.
2. For each Ψ_T a new function $\Xi_T = \hat{H}\Psi_T$ is then formed.

3. Importance sampled DMC is done using Ψ_T as the guiding wave function [72, 87, 91, 126]. In practice, this corresponds to performing two separate calculations in regions where $\Psi_t > 0$ and where $\Psi_t < 0$. This yields two pocket energies E_+ and E_- . This procedure works even if there are more than two pockets, i.e., for highly excited states. In this case E_+ and E_- are weighted average energies over all of the pockets for which the wave function is positive or negative, respectively.
4. Throughout all of these calculations flux histograms are accumulated as walkers cross the nodal surface of Ψ_T and Ξ_T independent of direction. Only Ψ_T is used to define the nodal surface for the actual elimination of walkers to avoid numerical instabilities.
5. If Ψ_T were an exact eigenfunction then all the pocket energies and histogram would be identical. The objective of the GA is to iterate to a Ψ_T which most nearly fulfills this criterion.

The fitness function is the same as used previously [100, 101] and is constructed by

1. Requiring equality of pocket energies.
2. Minimizing the distance and the standard deviation between the energies E_+ and E_- . In practice each fitness function (FNDMC) calculation may be repeated several times, using a different random number seed, to improve the statistics. However, this significantly increases the computational expense.
3. Minimizing the differences between the flux histograms. The histogram comparison is done automatically [100, 101]. In these calculations 1D histograms are sufficient and were constructed by projecting the binned walkers onto the x - or y - axes. In other cases multidimensional histogram comparison may be required.

2.5 Application and results

The GA-DMC algorithm was applied to the calculation of the excited state of a coupled quartic oscillator and excited states of the He-C₂H₂ van der Waals complex.

2.5.1 Quartic Oscillator

The Hamiltonian for this problem is given by

$$H = \frac{1}{2}(p_x^2 + \alpha p_y^2) + \lambda(x^4 + \alpha y^4) + \gamma x^2 y^2 \quad (2.1)$$

This Hamiltonian - and variants of it - has been extensively studied in the context of classical and quantum chaos [127] and the nodal structure of its wave function has also been recently investigated [128]. For comparison, accurate results were obtained by expansion in a direct product basis of 1D irreducible representation (A₁, A₂, B₁, B₂) and one 2D (E) representation. While taking advantage of symmetry would allow the number of coefficients in the GA search to be reduced it would also favorably bias the nodal search. We partially break the symmetry of the Hamiltonian by setting $\alpha = 2$. We set $\lambda = \frac{1}{2}$ and $\gamma = \frac{-6}{5}$ and atomic units are used throughout. Nodal surfaces can be encoded by assuming that the trial wave function may be represented by the following expansion:

$$\Psi_T(x, y; c_{n,m}) = \sum_{n=0}^N \sum_{m=0}^M c_{n,m} \phi_n(x) \phi_m(y) \quad (2.2)$$

In the expansion $N = M = 5$ for a total of 36 unknown real coefficients. Initially, the coefficients were generated randomly in the range (-1,1) such that

$$\sum_{n=0}^N \sum_{m=0}^M c_{n,m}^2 = 1 \quad (2.3)$$

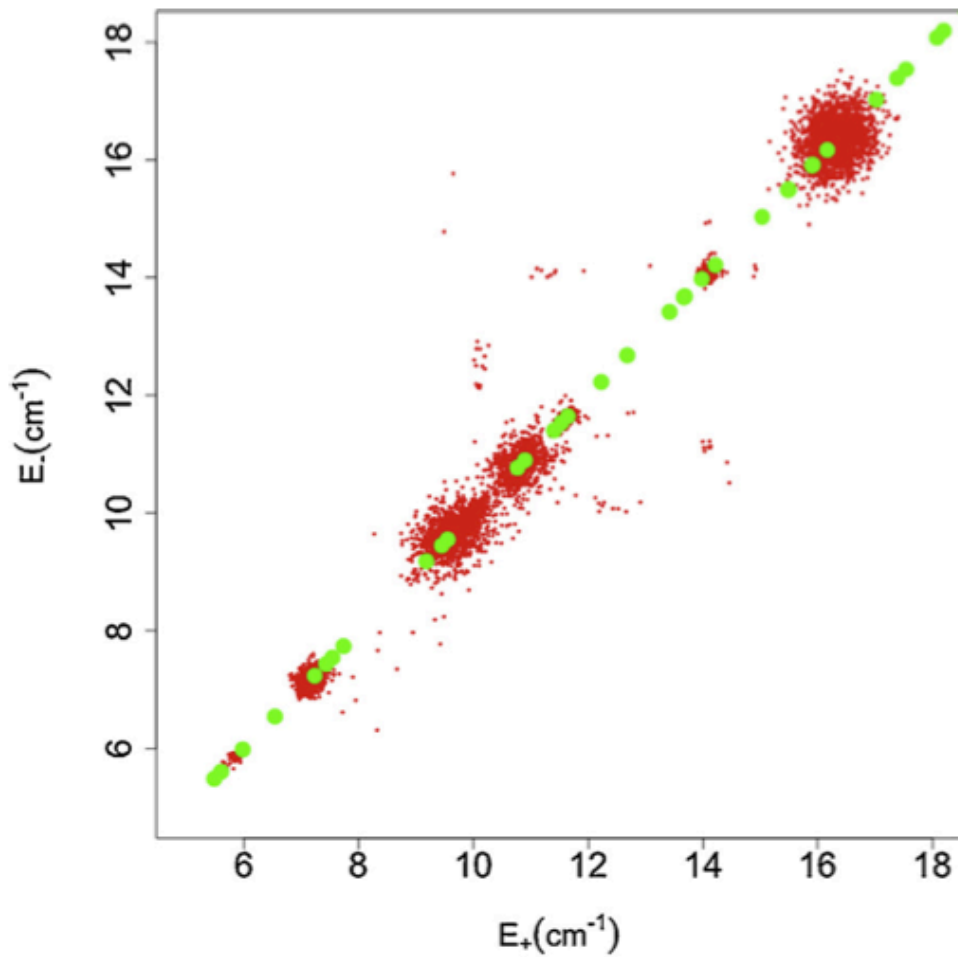


FIG. 2.1 (color online). Scatterplot (small filled circles, red online) showing the location of several relatively high fitness energy clusters detected by the GA-DMC algorithm after the first 25 generations. Also shown along the diagonal are the accurate eigenvalues (large filled circles, green online) obtained using a finite basis set as described in the text. (For interpretation of the references to color in this figure legend, the reader is referred to the web version of this article.)

Subsequently, the coefficients are modified by the GA with normalization being imposed before each new DMC run. In the DMC calculation importance sampling was done using Ψ_T to guide the walkers. In the converged variational calculations we set $N = M = 8$. Our procedure for locating the excited states is as follows:

1. A target range of energies is first selected. The fitness function is arbitrary set to zero if the average of the pocket energies of an individual falls outside of the target range.
2. Within the energy region of interest a scatter plot is made showing the final pocket energies of high-fitness individuals after 25 generations. An example is shown in Figure 2.1 in which several clusters are apparent. Also shown are the accurate eigenvalues obtained from numerical diagonalization of the Hamiltonian matrix. In displaying the GA-DMC clusters a fitness cut-off was used to eliminate the poorest quality individuals from the population. Several clusters are apparent which lie close to the actual eigenvalues. In principle, by systematically increasing the energy using relatively narrow energy windows, most or all of the eigenvalues can be located. In practice, it is often the case that only certain states are sought (e.g., Ref. [121]) and, in this case, system-specific information can be used to guide the GA.
3. One of the clusters is selected for further investigations and a new GA-DMC calculation is done. The calculation then proceeds as before except that:
 - (a) The energy range of interest is tightened around the cluster of interest.
 - (b) A new initial set of coefficients is generated from individuals whose pocket energies lie within the targeted cluster.
 - (c) As before, the GA varies the coefficient in the cluster of interest.

- (d) An “epochal” procedure [101] is used in which the number of DMC walkers and the total diffusion time are increased after every 25 generations.
4. The process is repeated until satisfactory convergence is achieved - i.e., until no further significant increase in the fitness function is observed.
 5. Finally a set of fixed-node DMC calculations using the best node are done to generate good statistics. Thus the error bars provided do not reflect uncertainties due to statistical fluctuations in the GA itself. In principle a small population of high-fitness nodal surfaces could be used then averaged.

In the calculations reported here, typically 3000 walkers were used to start and this number was increased to 9000 for the final set of calculations (step 5 above). Each generation contained 80 individuals and the propagation of $\sim 30 - 120$ generations was required to achieve satisfactory convergence.

Several states were selected for investigations using this procedure and the results for two of them are shown in Figures 2.2 and 2.3. Each panel shows the accurate eigenstate, an intermediate GA-DMC estimate of the nodal surface and the best GA-DMC estimate of the nodal surface. For comparison we also used the best variational function as a trial wave function in a FN-DMC calculation. The energies resulting from these calculation (i.e., using essentially the exact node) are given in the figure captions. In all cases the GA-DMC method leads to energies which are essentially indistinguishable from those found using the exact node. In the calculations corresponding to Figures 2.2 - 2.4 no knowledge of any symmetries in the problems were assumed. In all cases the wave function found by GA-DMC and the exact wave function are very similar as are the nodal surfaces. It is important to note that it is not necessary for the wave functional to be globally similar for the FN-DMC calculations to succeed, only that the nodes approximate the accurate nodes sufficiently well. A further set of calculations was also done for

a higher energy state using basis vectors of the appropriate symmetry in Eq. (2.4) - in this case products of odd function in x and even functions in y . This was done to compare with an unrestricted nodal search (i.e., one in which the symmetry of the Hamiltonian is not exploited). Not only is the converged nodal function closer to the exact one but, as expected, taking advantage of symmetry considerably speeds up the calculation. However, even though the nodal surface (and wave function) found in the symmetry-restricted calculation was slightly superior to that in the unrestricted calculation, the difference in the energies between the two calculations was negligible.

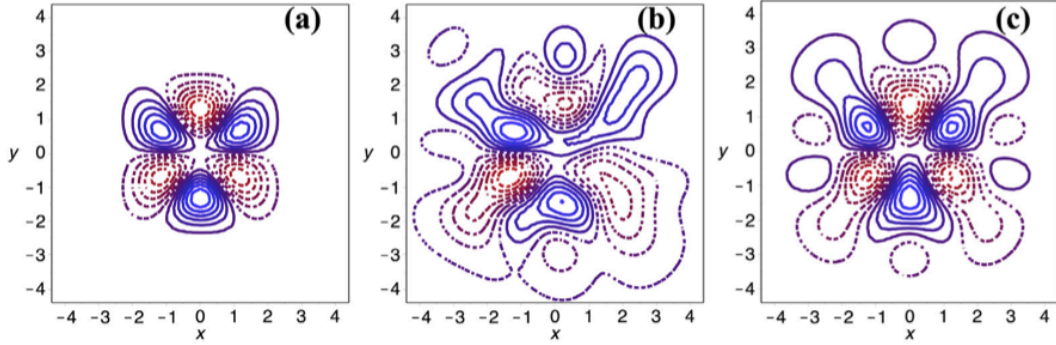


FIG. 2.2 Contour plots of the wave functions for the state with energy, $E=6.55$; (a) accurate wave function, (b) a high fitness function individual from half-way through the calculation and (c) the converged GA-DMC estimate of the nodal surface for this state. Blue (solid) and red (dashed) contours correspond to regions where the wave function is positive and negative, respectively. The pocket energies obtained for the converged GA-DMC calculation are $E_+ = 6.55 \pm 0.02$ and $E_- = 6.56 \pm 0.03$. For comparison, using the accurate wave function in a DMC calculation yields $E_+ = 6.55 \pm 0.03$ and $E_- = 6.55 \pm 0.02$. (For interpretation of the references to color in this figure legend, the reader is referred to the web version of this article.)

2.5.2 Excited states of He-C₂H₂

We also made application to the calculation of several excited states of the He-C₂H₂ complex using a recent intermolecular potential energy surface [129, 130]. As in a previous study of the He-CO complex [121] the He atom is confined to a sphere (in this case of a radius $R_0 = 9.55$ bohr). The BOAS model has consistently been shown to provide a reasonably accurate description of the nodal surfaces of weakly bound van der Waals complexes containing several He atoms. The advantage is that considerably less computational effort is required to solve the BOAS problem than the full dimensionality problem because of difficulties including the radial degrees of freedom [100, 101, 121]. Here we demonstrate how GA-DMC can be used to compute nodal surfaces on the fly of these systems.

The Hamiltonian, in the BOAS approximation, is [121]

$$\hat{H} = \frac{\hat{j}^2}{2I} + \frac{\hat{l}^2}{2mR_0^2} + V(R, \theta) \quad (2.4)$$

where I is the moment of inertia of the C₂H₂ molecule; \hat{j} is the molecular rotational angular momentum (AM) operator and \hat{l} is the orbital AM operator for the He atom (mass m). The atom-molecule potential energy surface (PES) is $V(R, \theta)$ where R and θ are the usual Jacobi coordinates [129, 130]. Based on diffusion Monte Carlo calculations for the full problem we set $R_0 = 9.55$ bohr throughout. The gas phase rotational constant for C₂H₂ is $B_0 = 1.176642$ cm⁻¹.

The procedure is as follows.

1. Because the He atom is confined to the surface of the sphere the primitive basis functions that are used depend on three angles; the space-fixed polar angles of the molecule (θ_1) and the atom (θ_2) and the difference between the azimuthal angles of the molecule and the atom, that is, $\phi = \phi_1 - \phi_2$. They also depend on two quantum numbers (j, m_j) for the molecule and two

(l, m_l) for the atom. The total angular momentum quantum number, J , is a good constant of the motion.

2. Explicitly the primitive basis functions are given by:

$$\Psi_{j,m_j}^{l,m_l}(\theta_1, \phi_1, \theta_2, \phi_2) = Y_j^{m_j}(\theta_1, \phi_1) \times Y_l^{m_l}(\theta_2, \phi_2) \quad (2.5)$$

3. However, the basis functions used in the optimization are linear combinations and are defined:

$$\Psi_j^l = \sum_{m_j=-j}^{m_j=j} \sum_{m_l=-l}^{m_l=l} \langle j, m_j, l, m_l | J, O \rangle \times Y_j^{m_j}(\theta_1, \phi_1) \times Y_l^{m_l}(\theta_2, \phi_2) \quad (2.6)$$

where $\langle j, m_j, l, m_l | J, O \rangle$ are Clebsch-Gordon coefficients.

4. The total expansion of the wave function with unknown coefficients is

$$\Phi = \sum_{j=0}^{j=N} \sum_{l=0}^{l=N} c_j^l \times \Psi_j^l \quad (2.7)$$

where the $(N + 1)^2$ coefficients are optimized using the GA-DMC.

Figure 2.4 compares the converged GA-DMC energies and wave functions with the accurate BAOS wave function obtained by an accurate diagonalization of the Hamiltonian given by Eq. (2.6). The basis functions in Eq. (2.6) were used in the diagonalization. Also, shown are accurate results of the full dimensional complex obtained using a discrete variable representation for the radial degree of freedom of the complex. Similar results were obtained for other excited states. This approach is easily generalized to more than a single He atom.

2.5.3 Computational details

For the quartic oscillator, the calculations were performed using a small computer cluster consisting of 5 nodes, each of which contained a Core intel i7 processor. Each i7 processor had 4 cores and hyper threading was used for a total of 80 processes per run. Each generation thus contained a total of 80 individuals and each generation took about 10 min to complete. The total number of generations required to achieve convergence varied with the complexity of the nodal surface. The simplest nodal topology studied here, shown in Figure 2.2, was found to be converged after 63 generations. The more complicated nodal surface shown in Figure 2.3 was converged after 96 generations, respectively. Without taking advantage of symmetry, convergence to the nodal structure shown was achieved after 112 generations; using symmetry led to convergence after 33 generations. For the He-C₂H₂ complex the calculations were done at the Utah State High Performance Computing Center (HPCC) using the Pikaia code [125]. A population of 80 individuals was used and the calculations for the state shown in Figure 2.4 converged after 60 generations.

2.6 Conclusions

These results show that combining a GA with FNDMC calculations can be an effective way of locating (or improving) nodal surface on the fly. In order to apply the method it is necessary that a parameterization of the nodal surface be available. In the present computations a basis set expansion with unknown coefficients was assumed. This will likely not be the best choice for higher dimensional problems. However, this is not a drawback particular to GA-DMC because, in any FNDMC calculation, some choice of nodal function is necessary; the GA-DMC procedure provides a systematic way of improving on that choice. If a decent guess at the nodal surface is available in advance then a VMC calculation might be preferable. However, in many applications a good approximation to the nodal surface will

not be available. Furthermore, even if the trial wave function is obtained using VMC the GA method could still be used to refine the nodal surface. This may be necessary because it is not clear if a VMC calculation, which minimizes the energy, necessarily also produces a good estimate of the nodal hyper surface.

The main challenge for the GA-DMC is the construction of an *ansatz* for the trial wave function and nodal surface. Of course, additional complications may also arise related to possible pathologies of the nodal hyper surface involved (e.g., bottlenecks, jumps from one positive region to another after “flying” over negative regions, etc.). Discovering how to handle these complications will require further study as will the possible application of this approach to fermionic systems. Because the nodal surface of many-fermion systems may be very complicated, even for the ground state, it may be difficult to capture the nuance of small nodal pockets. In these cases it may be necessary to employ more sophisticated methods for multi-dimensional histogram comparison.

2.7 Acknowledgments

This work has been supported by the US National Science Foundation through grant CHE-1300504. We thank the HPCC at Utah State University for computer time. We also thank Sandra Lundell for helpful comments.

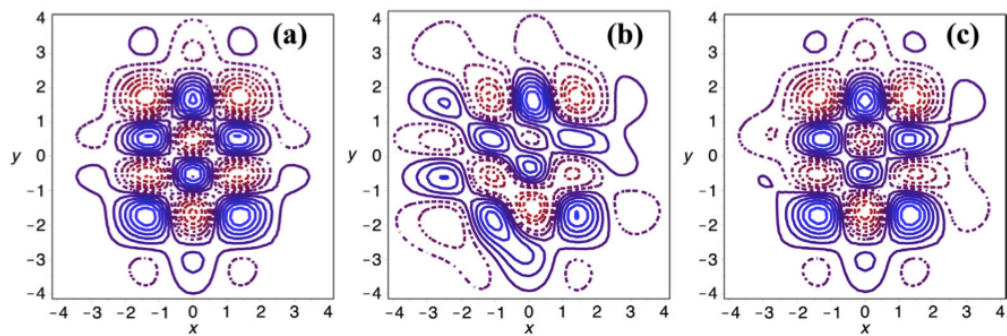


FIG. 2.3 Contour plots of the wave functions for the state with energy, $E=9.551$; (a) accurate wave function, (b) a high fitness function individual from half-way through the calculation and (c) the converged GA-DMC estimate of the nodal surface for this state. Blue (solid) and red (dashed) contours correspond to regions where the wave function is positive and negative, respectively. The pocket energies obtained for the converged GA-DMC calculation are $E_+ = 9.56 \pm 0.09$ and $E_- = 9.55 \pm 0.04$. For comparison, using the accurate wave function in a DMC calculation yields $E_+ = 9.55 \pm 0.04$ and $E_- = 9.55 \pm 0.06$. (For interpretation of the references to color in this figure legend, the reader is referred to the web version of this article.)

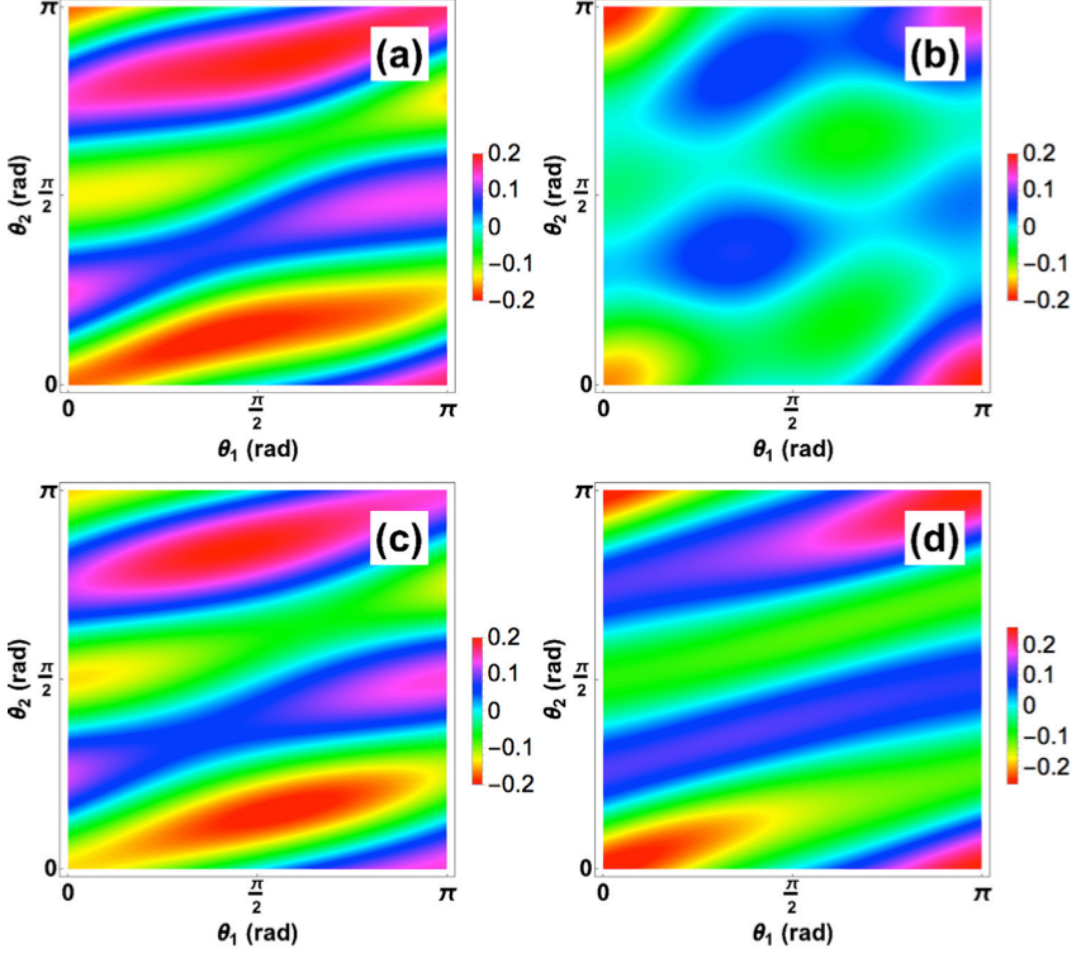


FIG. 2.4 Density plots of the wave functions for the BOAS (a-c) and accurate (d) He-C₂H₂ state nominally labeled $|j, l \rangle = |1, 4 \rangle$ with total angular momentum $J = 3$. The accurate energy of the BOAS state is $E = 5.965 \text{ cm}^{-1}$ with respect to the ground state. The figure shows projections of the wave function onto the $\theta_1 - \theta_2$ plane: the azimuthal angles of the molecule (ϕ_1) and the atom (ϕ_2) are both set to zero. Panel (a) shows the accurate BOAS wave function; (b) shows a typical individual from part-way through the calculation. The energies for this state are $E_+ = 4.813 \pm 0.014$ and $E_- = 3.772 \pm 0.007$. Panel (c) shows the converged GA-DMC estimate of the nodal surface for this state. The pocket energies obtained for the converged GA-DMC calculation are $E_+ = 5.943 \pm 0.009$ and $E_- = 5.947 \pm 0.007$. For comparison panel (d) show the equivalent projection of the full dimensional wave function (i.e., with the He atom not being confined to a sphere). The exact energy for the state in panel (d) is 5.740 cm^{-1} [130].

CHAPTER 3

MICROSCOPIC SUPERFLUIDITY IN ^4He CLUSTERS STIRRED BY A
ROTATING IMPURITY MOLECULE

3.1 Abstract

The effective moment of inertia of a CO impurity molecule in $^4\text{He}_N$ and $p\text{-H}_2$ solvent clusters initially increases with N but then commences a nonclassical decrease at $N = 4$ (^4He) or $N = 6$ ($p\text{-H}_2$). This suggests molecule-solvent decoupling and a transition to microscopic superfluidity. However, the quantum decoupling mechanism has not been elucidated. To understand the decoupling mechanism, a one dimensional model is introduced in which the ^4He atoms are confined to a ring. This model captures the physics and shows that decoupling happens primarily because of bosonic solvent-solvent repulsion. Quantum Monte Carlo and basis set calculations suggest that the system can be modeled as a stirred Tonks-Girardeau gas. This allows the N -particle time-dependent Schrödinger equation to be solved directly. Computations of the integrated particle current reveal a threshold for stirring and current generations, indicative of a superfluid.

3.2 Publication

Impurity molecules doped into small bosonic clusters consisting of ^4He or $p\text{-H}_2$ solvent particles appear to decouple from their environment as the cluster grows in size [2, 4, 21, 61, 62, 112]. Decoupling is suggested experimentally by sharp, free-molecule-like, rotational lines in the spectra and has been attributed to the onset of a new phenomenon, microscopic superfluidity [5, 25, 27, 55, 61, 62]. However, the relationship between microscopic superfluidity and conventional (bulk) superfluidity remains largely unexplored. The onset of microscopic superfluidity

Coauthored by Angeline R. Wairegi, Antonio Gamboa, Andrew D. Burbanks, Ernestine A. Lee and David Farrelly. Reproduced with permission of *Phys. Rev. Lett.*, 112, 143401 (2014). Copyright 2014 American Physical Society.

is inferred from the nonclassical turnaround and subsequent increase in the effective rotational constant (B_{eff}) of the molecule (a decrease in the effective moment of inertia) as the number (N) of solvent particles is increased [21, 25, 55, 103]. Microscopic (or mesoscopic) superfluidity also occurs in cold-atom physics and, in particular, low-dimensional ultra cold gases [105, 131, 132]. For example, theoretical studies demonstrate that a one dimensional (1D) gas of impenetrable bosons—a Tonks-Girardeau (TG) gas [104–106]—constrained to a ring of finite circumference displays a critical velocity below which the system is hard to stir. If the stirring perturbation is a δ -function barrier then it experiences a zero drag force except at certain stirring velocities [133]. Here we demonstrate that the physics of microscopic superfluidity in bosonic solvents shares much in common with a stirred TG gas with the barrier replaced by a rotating impurity molecule. This finding allows the N -body time-dependent Schrödinger equation (TDSE) to be solved numerically. In particular, computation of the integrated particle current uncovers key signatures of superfluidity [131].

The decoupling of impurity molecules from the bosonic solvent has previously been attributed to superfluidity in path integral Monte Carlo (PIMC) simulation [55]. Using the two-fluid model, in $p\text{-H}_{2N}\text{-CO}$ clusters, both a normal and a superfluid component were found to coexist. The main finding of the PIMC calculations was a superfluid fraction that declined from about 95% at $N = 1$ to about 82% at $N = 6$, followed by an increase to essential 100% for $N > 10$. These calculations provide excellent agreement with the experimentally observed behavior of B_{eff} for $N < 10$, as do previous 0 K quantum Monte Carlo simulations [78, 111, 113]. Nevertheless, as emphasized in a recent review [62], while PIMC can simulate essentially all the properties of superfluid ^4He , it does so by projecting the system on a classical analogy. This may make it difficult to draw direct conclusions about the actual quantum behavior. For example, the reporting of a normal and superfluid fraction for $N = 1$ [55] is difficult to interpret physically. Furthermore, there is no

unique definition of microscopic superfluidity [131], and the quantum decoupling mechanism itself has not previously been elucidated.

Our objective is to understand how the decoupling mechanism occurs and also whether calculations of the particle current density indicate superfluid behavior. The latter calculation requires the solution of the $(N + 1)$ -body TDSE, which is clearly not possible for the full dimensionality problem. Therefore, we construct a reduced-dimensionality model of the ${}^4\text{He}_N$ -CO system with the ${}^4\text{He}$ atoms confined to a ring as shown in Fig. 3.1 (not to be confused with the Lehmann’s very useful but nevertheless “toy” model [107]). This model has the felicitous property that it permits accurate quantum basis set computations for $N \leq 5$. Using quantum Monte Carlo calculations, we first demonstrate that the model contains the essential physics, that is, the turnaround in B_{eff} . The calculations suggest a further simplification: modeling the problem as a stirred TG gas. It is this step that allows us to solve the TDSE directly for N ${}^4\text{He}$ atoms stirred by the molecule.

The Hamiltonian, in the limit of the BOAR approximation (see Fig. 3.1), is

$$\hat{H}_{BOAR} = \frac{\hat{j}_z^2}{2I_{CO}} + \sum_{i=1}^N \left[\frac{\hat{l}_{iz}^2}{2mR_0^2} + V(\phi_i - \theta) \right] + \sum_{i < k}^N U(\phi_i - \phi_k) \quad (3.1)$$

where I_{CO} is the moment of the inertia of the CO molecule and \hat{j}_z is the molecular rotational angular momentum (AM) operator; the quantity $\frac{\hbar^2}{2mR_0^2} \approx 0.19 \text{ cm}^{-1}$ is used to define a moment of inertia $I_0 = Mr_0^2$; \hat{l}_{iz} is the orbital AM operator for the i^{th} ${}^4\text{He}$ atom (mass m), and ϕ_i and θ are angles show in Figure 3.1. The atom-molecule potential energy surface (PES) is $V(\phi_i - \theta)$ and the PES of Ref. [134] is used. The He-He PES is $U(\phi_i - \phi_k)$. Based on previous diffusion Monte Carlo calculations [100] R_0 , we set at $R_0 = 9$ bohr throughout. The gas phase rotational constant for CO is $B_0 = 1.9225125 \text{ cm}^{-1}$. Two reference angular frequencies are

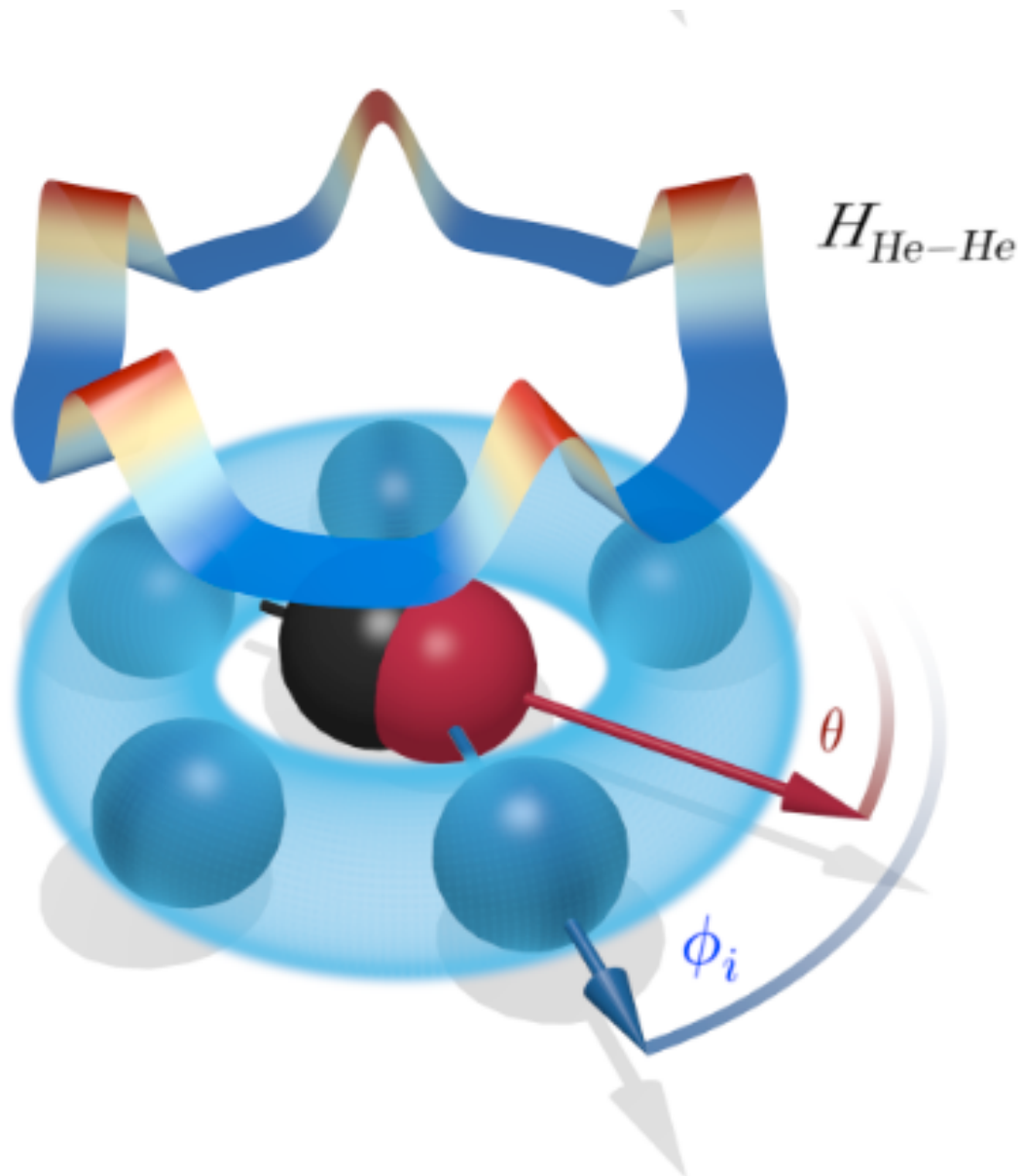


FIG. 3.1 (color online). Boson-on-a-ring model. The ${}^4\text{He}$ atoms (blue) are confined to revolve on a ring of radius R_0 measured from the center of mass of the CO molecule (black/red). The molecule is pinned at the origin and rotates in the plane of the ring. The azimuthal angles of the molecule and the i^{th} ${}^4\text{He}$ atom are θ and ψ_i , respectively. The ribbon above the ring illustrates the soft Gaussian potential, $U_{\text{He-He}}^g$, as a function of the angles between the He atoms.

introduced for future use: $\omega_0 = \frac{\hbar}{I_0}$ and $\omega_{eff} = \frac{\hbar}{I_{CO}^{eff}}$ where I_{CO}^{eff} is an effective moment of inertia that will be varied.

To further simplify the Hamiltonian, the $^4\text{He-CO}$ PES is expanded in Legendre polynomials with only the first three (dominant) terms being retained, i.e., $V(R, \Theta) = \sum_{n=0}^{n=2} V_n(R_0) P_n(\Theta)$ where $\Theta = \phi_i - \theta$. Actually, in the BOAR model, the isotropic V_0 contribution is simply an additive constant. Three forms for the He-He PES are used: (i) the empirical PES of Aziz, McCourt, and Wong (AMcW) [135], (ii) a purely repulsive Gaussian barrier, and (iii) a δ -function potential as in the TG gas. The Gaussian barrier is given by $U_{He-He}^{(g)}(\phi_{ij}) = g_0 e^{-\alpha \phi_{ij}^2}$ where ϕ_{ij} is the angle between the i^{th} and j^{th} ^4He atom (see Figure 3.1). The Gaussian approximation interpolates between the actual AMcW PES and the TG limit. In addition, its function form simplifies the calculation of matrix elements as compared to the AMcW PES. Two set of parameters for the Gaussian barrier are used (see the caption to Fig. 3.2) corresponding to a hard and soft barrier. The soft Gaussian, shown as a ribbon in Fig. 3.1, roughly models the actual van der Waals radius of the ^4He atoms, whereas the much harder barrier lies closer to the TG limit of a δ -function potential with strength going to infinity [131].

TABLE 3.1 Energy splittings ($\Delta E = 2B_{\text{eff}}$) between the ground state and the lowest excited state in the a -type series of the $\text{CO-}^4\text{He}_N$ cluster. Units are cm^{-1} .

N	Expt.	BOAS ^a	BOAR ^b	BOAR ^c	BOAR ^d	BOAR ^e
1	0.576	0.516 ± 0.029	0.183	0.191 ± 0.027	0.213 ± 0.022	0.191 ± 0.025
2	0.516	0.443 ± 0.031	0.174	0.176 ± 0.028	0.187 ± 0.028	0.134 ± 0.029
3	0.482	0.357 ± 0.052	0.101	0.110 ± 0.051	0.154 ± 0.061	0.114 ± 0.066
4	0.488	0.457 ± 0.072	0.425	0.417 ± 0.067	0.492 ± 0.069	0.323 ± 0.072
5	0.526	0.583 ± 0.083	0.754	0.712 ± 0.092	0.772 ± 0.077	0.534 ± 0.079
6	0.616	0.654 ± 0.152	–	0.931 ± 0.142	1.042 ± 0.098	0.755 ± 0.107
7	0.787	0.951 ± 0.176	–	1.356 ± 0.192	1.412 ± 0.134	1.051 ± 0.113
8	1.442	1.275 ± 0.201	–	1.723 ± 0.277	1.953 ± 0.199	1.312 ± 0.211
9	1.893	1.612 ± 0.245	–	–	–	–
10	2.342	1.883 ± 0.312	–	–	–	–

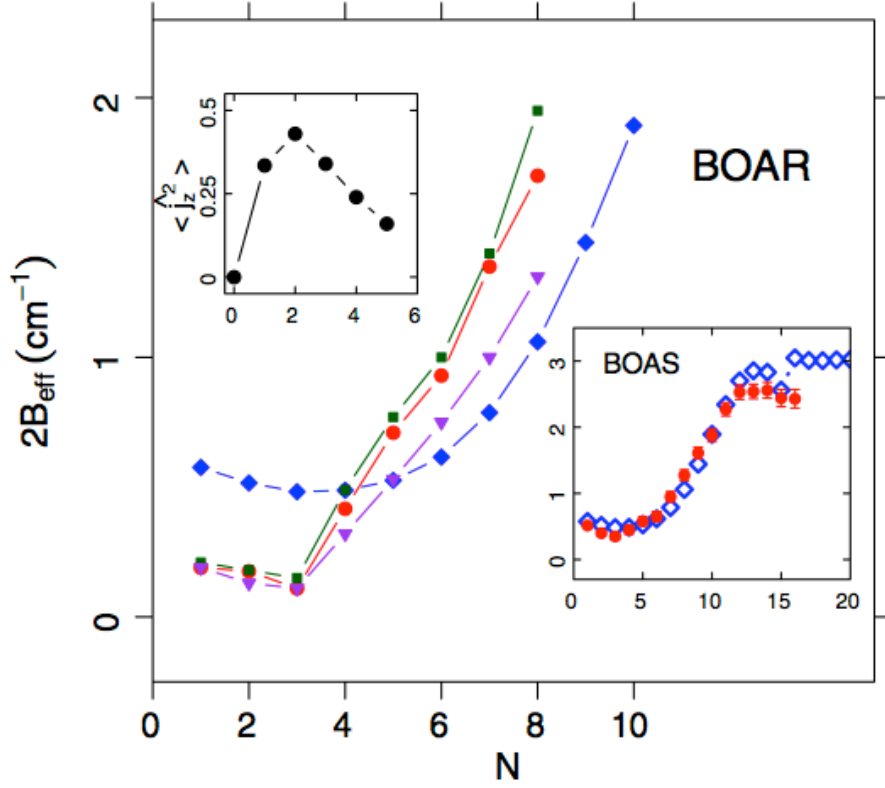


FIG. 3.2 (color online). Effective rotational constant (B_{eff}) for a CO dopant in ^4He atoms (N). Shown are the experimental results (blue diamonds-mm/microwave results [21] for $N \geq 10$ and IR results otherwise [79]); FNDMC results using the Aziz PES (green circles) and two different forms of the Gaussian barrier with $g_0 = 100\text{cm}^{-1}$, $\alpha = 40\text{rad}^{-2}$ (soft barrier, red circles) and $g_0 = 500\text{cm}^{-1}$, $\alpha = 750\text{rad}^{-1}$ (hard barrier, purple inverted triangles). For clarity, error bars have been omitted from the hard Gaussian barrier. The large triangles are results from the accurate basis calculations. The lower inset compares experimental to FN-DMC results in the BOAS model using the soft Gaussian. The Aziz PES leads to almost indistinguishable results. The upper inset shows $\langle j^2 \rangle$ as a function of N obtained from the basis set calculations.

Fig. 3.2 compares computed values of the effective rotational constant B_{eff} with the experimental results [21, 79]. As in the experiments, B_{eff} is defined to be half of the energy difference between the ground state and the lowest excited a-type state [21, 100]. The fixed-node diffusion Monte Carlo (FN-DMC) results were obtained using the genetic algorithm DMC method [100]. Results are shown using the AMcW PES and both the hard and soft Gaussian barriers in the BOAR model. Not shown are the accurate results (for ≤ 5) obtained using a finite basis set consisting of Bose symmetrized products of eigenfunctions of the operator \hat{j}_z (i.e., $e^{im_j\theta}$) and \hat{l}_{iz} (i.e., $e^{im_i\phi_i}$). See Table. 3.1 for tabulated results up to $N = 10$.

To illustrate how well the Gaussian barrier captures the physics, the lower inset in Fig. 3.2 also compares experimental to FN-DMC results in a “bosons-on-a-sphere” (BOAS) model. In the approximation, the ^4He atoms move on the surface of a sphere, and the CO molecule is allowed to rotate in three dimensions. The BOAS Hamiltonian is closer to the full problem than is the BOAR model, and the agreement with experiment is correspondingly better, especially for $N < 10$. The BOAS model is better because it less simplified and more faithfully reproduces how the ^4He density is distributed in three dimensions. However, both the BOAR and BOAS models capture the initial decrease in B_{eff} with an early turnaround at $N \sim 3 - 4$. The value of N at which the turnaround occurs can be varied by altering the strength or symmetry of the atom-molecule interaction or by varying B_0 artificially. All of the calculations in Fig. 3.2 are quite congruent with the experimental results. A practical advantage of the BOAR (as compared to BOAS) model is that accurate basis set calculations are possible for N values that bracket the turnaround in B_{eff} . The results of the basis set results up to $N = 5$, reported in the Supplemental Material [136], agree we with the DMC results.

^aobtained using fixed-node diffusion Monte Carlo and the soft Gaussian barrier

^bobtained using a finite basis set and the soft Gaussian barrier

^cobtained using fixed-node diffusion Monte Carlo and the AMcW potential

^dobtained using fixed-node diffusion Monte Carlo and the soft Gaussian barrier

^eobtained using fixed-node diffusion Monte Carlo and the hard Gaussian barrier

Also shown in Fig. 3.2 is $\langle \hat{j}_z^2 \rangle$ for the ground state of the BOAR Hamiltonian as a function of N using the soft Gaussian barrier in the basis set calculations. After an early rise to a maximum at $N = 2$, $\langle \hat{j}_z^2 \rangle$ falls quite rapidly with increasing N . Absent any atom-molecule coupling (e.g., $N = 0$), or for an isotropic interaction, $\langle \hat{j}_z^2 \rangle = 0$. Deviations of $\langle \hat{j}_z^2 \rangle$ from zero (in the ground state) are, therefore, an indicator of the extent of molecule-solvent coupling, i.e., \hat{j}_z is no longer a constant of the motion when anisotropic coupling exists. The decrease in $\langle \hat{j}_z^2 \rangle$ with N therefore demonstrates dynamical decoupling of the molecule. The decoupling is primarily due to the repulsive solvent-solvent interactions because it occurs even when the AMcW He-He potential, which contains both repulsive and attractive branches, is replaced by a purely repulsive Gaussian barrier.

The dynamical decoupling of the solvent suggest the system might reasonably be modeled as a one-dimensional TG gas confined to a ring and stirred by the molecule; that is, we take the δ -function limit of the Gaussian barrier and drop the term in \hat{j}_z^2 in Eq. (3.1) altogether. It is important to note that the latter step is not an adiabatic approximation based on the different time scales of the solvent and the bare CO molecule. Rather, it is motivated by the basis set calculations, which demonstrate that the molecule decouples substantially even for the relatively small values of N . The main reason for making this approximation is that it allows the TDSE to be solved numerically for N particles, thereby allowing the particle current to be computed. The resulting Hamiltonian is

$$\hat{H}_{TG} = -\frac{\hbar^2}{2mR_0^2} \sum_{i=1}^N \frac{d^2}{d\phi_i^2} + \sum_{i<k}^N g\delta(\phi_i - \phi_k) + \sum_{i=1}^N V(\phi_i - \omega_{eff}t). \quad (3.2)$$

Because the rotational kinetic energy operator for the molecule has been neglected, θ may be replaced semi-classically by $\omega_{eff}t$ where ω_{eff} is the (variable) angular frequency introduced earlier and t is time. This approximation has the

justification that if the rotationally excited molecule is undergoing effective free rotation then the ^4He atoms will be subject to a time periodic perturbation. The presence of the δ -function potential allows, in the TG gas limit when $g \rightarrow \infty$, the Bose-Fermi (BF) mapping [104, 105] to be applied. The relative insensitivity of the results to the hardness of the Gaussian barrier is the reason that the system can be modeled as a TG gas with no need to consider the more complicated (to implement) Lieb-Liniger case [131]. For the ground state, the bosonic wave function is given by

$$\Psi_B(\phi_1, \phi_2 \phi_1, t) = \frac{1}{\sqrt{N!}} |\det[\psi_l(\phi_i, t)]|, \quad (3.3)$$

where $l, i = 1 \dots N$. The determinant is a Slater determinant constructed using N orbitals, $l = 0 \dots N - 1$ [105], defined as solutions of the TDSE

$$i\hbar \frac{d\psi_l(\phi, t)}{dt} = \left(-\frac{\hbar^2}{2mR_0^2} \frac{d^2}{d\phi^2} + V(\phi - \omega t) \right) \psi_l(\phi, t). \quad (3.4)$$

To compute the current density, the TDSE is integrated numerically with the initial ($t = 0$) states being the N orbitals obtained by solving a form of the Whittaker-Hill equation [137]

$$\left(-\frac{\hbar^2}{2mR_0^2} \frac{d^2}{d\phi^2} + a\cos\phi + b\cos 2\phi \right) \psi_l(\phi) = E_{l\psi_l}(\phi), \quad (3.5)$$

where $a = V_1(R_0)$, $b = 3V_2(R_0/4)$ and an inessential additive constant has been omitted. The orbitals may be solved for numerically using recurrence relations [137, 138]. To demonstrate that the TG limit of the BOAR model is, in fact, a reasonable approximation, we compare directly the BF-mapped Whittaker-Hill

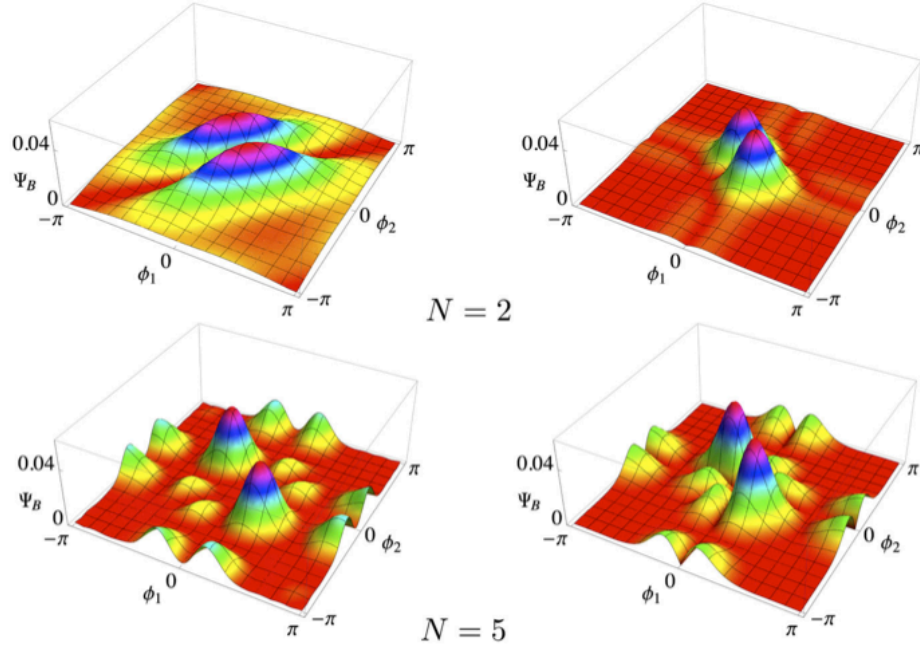


FIG. 3.3 (color online). Comparison of the actual ^4He -atoms-on-a-ring wave functions using the soft Gaussian barrier (left column) with the BF wave functions (right column) corresponding to the TG gas in the presence of an impurity molecule; $N = 2$ (top row) and $N = 5$ (bottom row). To allow a comparison θ is set to 0. For $N = 5$, three of the five helium angles were fixed.

wave functions (at $t = 0$) and the accurate BOAR wave functions obtained from the basis set calculations, with $\theta = \omega_{eff}$, $t = 0$. Figure 3.3 presents sections through BOAR (using the soft Gaussian barrier) and BF wave functions for $N = 2$ and $N = 5$. For $N = 2$, the BOAR wave function is significantly more delocalized than the BF wave function. At $N = 5$ the agreement is much better, although clearly not perfect. These plots are evidence of the rapid decoupling of the molecule from its environment with increasing N . They also justify taking the TG limit.

The TDSE in Eq. (3.4) corresponds to a TG gas confined to a ring and stirred by a freely rotating molecule. Similar to Schenke et al. [133], who used a δ barrier to stir a TG gas confined to a ring, we calculate the time- and space- averaged current density, F , for a non adiabatic initial excitation of the molecule at $t = 0$. The TDSE was integrated numerically (after scaling) using as initial states the

orbitals obtained by solving Eq. (3.5) for the $l = 0 \dots 6$ orbitals corresponding to $N = 7$. The TDSE was integrated using a method similar to that described in Ref [139]. Results were checked using a fast Fourier transform, split-operator procedure [140, 141]. We also computed the Floquet quasienergies using generalized Floquet theory [142], and they, together with F , are shown in Fig. 3.4 as function of the angular frequency ratio ω_{eff}/ω_0 .

At integer values of the ratio ω_{eff}/ω_0 the Floquet states, starting at $N = 4$, show avoided crossings similar to those discovered in Ref. [133]. These states become coupled by the molecule that opens up gaps at integer values of ω_{eff}/ω_0 . This allows for the population of higher AM states and thereby current excitation. The structure of the Floquet spectrum thus accounts for the peaks in the integrated current density also shown in Fig. 3.4. It is significant that the avoided crossings first appear when the molecule has significantly decoupled from its environment, i.e., close to the onset of microscopic superfluidity. Away from integer values of ω_{eff}/ω_0 , the flux plot indicates that the TG gas is harder to stir. There also exists a velocity threshold for current generation at $\omega_{eff}/\omega_0 = 1$, which is indicative of superfluid behavior. However, unlike in Ref. [133], below this threshold, F is not exactly zero, nor is it zero between subsequent peaks. Rather, the background current increases and eventually saturates. This predicts that B_{eff} will converge to a nanodroplet limiting value lower than B_0 , which is consonant with both experiment and previous quantum Monte Carlo studies [78, 100, 113]. That is, the molecular impurity will experience a drag force even at 0 K. Similar behavior at 0 K has been noted previously in a quasi-1D Bose-Einstein condensate [132].

In summary, the BOAR model show the decoupling of molecule can be traced primarily to the interplay between the purely repulsive interactions between the bosonic ^4He atoms and the strength and symmetry of the molecule-solvent interaction. Solving the TDSE in the TG limit reveals a drag force at 0K together with a threshold for stirring. Because the energy spectra for 1D hard-core bosons and

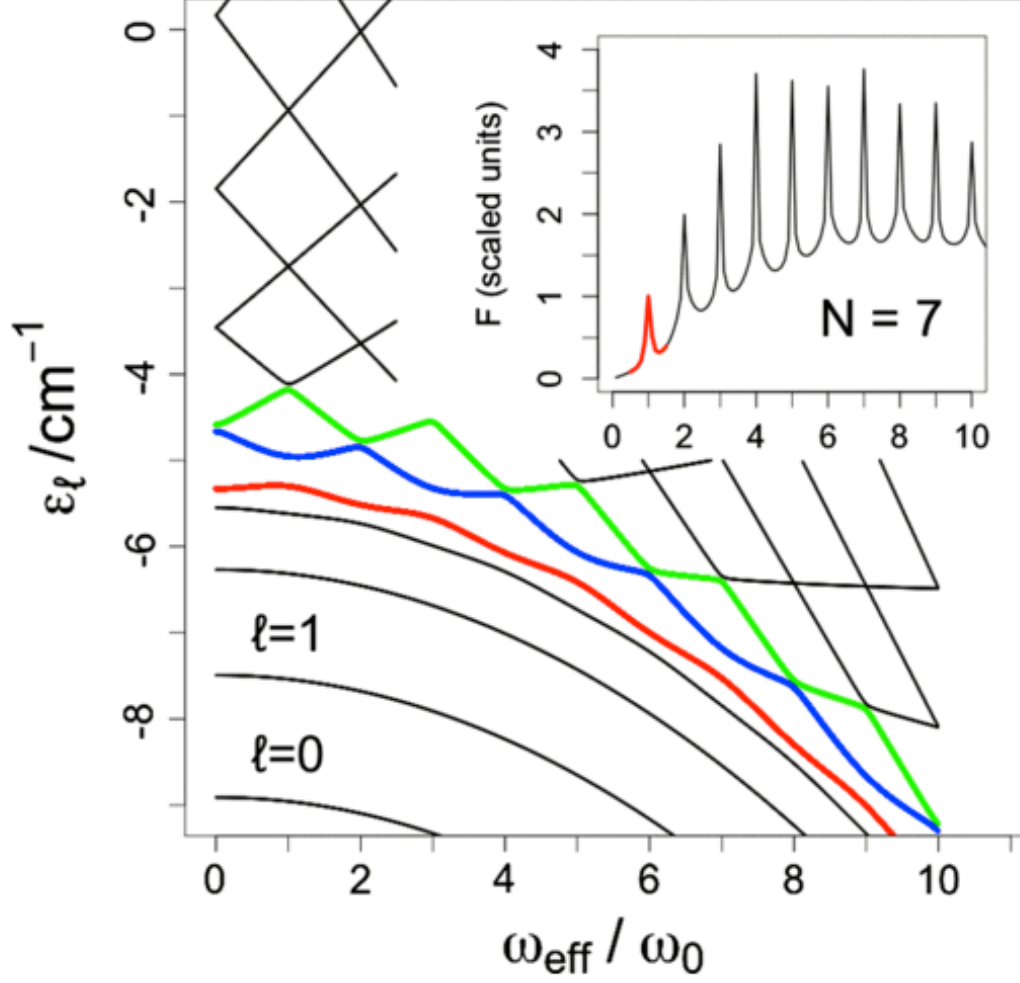


FIG. 3.4 (color online). Floquet eigenvalues ϵ_α (where α labels the Floquet mode [142]) as a function of the ratio $\omega_{\text{eff}}/\omega_0$. The insert shows the long-time-averaged, spatially integrated flux, F , obtained by propagating the time dependent BF mapped wave function numerically (shown also as a function of $\omega_{\text{eff}}/\omega_0$). The flux and its averaging were done as described in the text and in Ref. [133]

fermions are identical [104], any significant differences between purely repulsive-doped 1D fermionic ^3He and bosonic ^4He atoms confined to a ring must arise because of the differences in the decoupling mechanism (that is, if decoupling occurs at all for ^3He [2, 61, 62, 143]). For fermions (^3He) the attractive part of the He-He PES may play a role by providing a pairing mechanism [144].

This work was supported, in part, by Grant No. CHE1300504 from the National Science Foundation to D.F. at Utah State University. We thank a referee for pointing out an article that finds the exact ground state for a Bose-Einstein condensate on a ring [145].

CHAPTER 4

MICROSCOPIC SUPERFLUIDITY OF HCN DOPED ^4He DROPLETS

4.1 Abstract

The phenomenon of superfluidity, and its closely related counterpart the Bose-Einstein condensate, in ^4He has been extensively studied since its discovery in 1955. However, comparatively fewer studies have been done on the phenomenon of microscopic superfluidity which has been observed in as few as four ^4He atoms. Microscopic superfluidity is characterized by the initial increase of the effective moment of inertia with increasing cluster size (N) and a subsequent decrease at $N = 4$ for (^4He atoms) or $N = 6$ for ($p\text{-H}_2$). This non classical turnaround in the effective moment of inertia is considered an indicator of molecule-solvent decoupling. The physics behind this decoupling are largely unexplored. In this article we describe the study of microscopic superfluidity in ^4He -HCN clusters using a new fixed-node diffusion Monte Carlo (FNDMC) method. In this approach a genetic algorithm is coupled to the FNDMC method and used to elucidate the nodal surfaces of the wave function on the fly and a reduced dimensionality model, a one dimensional model in which the ^4He atoms are confined to a ring (BOAR model), is introduced to study the decoupling mechanism of the dopant molecule and the boson solvent. Previous studies [121] on a similar system, ^4He -CO, show the system can be modeled as a stirred Tonks-Girardeau gas which then allows for the N -particle time-dependent Schrödinger equation to be solved directly. The data obtained suggests that the decoupling mechanism is primarily a factor of bosonic solvent-solvent repulsion.

4.2 Introduction

The quantum solvation of molecular dopants in bosonic solvents is currently of great interest [2, 4, 7, 146, 147]. Conventional wisdom states that a molecule dissolved in a liquid will not rotate as freely, with a few notable exceptions [7, 148],

as it might in a gas. However, numerous studies have observed coherent molecular rotations over many periods in ultra cold droplets of ^4He atoms [2, 4, 6, 7, 12, 44, 54, 146, 149–153]. The pioneering “Andronikashivilli-type” experiments in this field [2, 54] studied SF_6 and OCS molecules doped into ^4He nanodroplets [1, 6, 12]. These experiments observed sharp rotational features, characteristic of free (gas-phase) molecular rotations, but with reduced (renormalized) rotational constants; a trend that was observed across the board in molecules seeded into ^4He nano-droplets [4, 146]. In fact, impurity molecules doped in both ^4He or $p\text{-H}_2$ clusters, seem to decouple from their environment with increasing cluster size [2, 4, 21, 61, 62, 112]; indicated in experimental studies by the observation of sharp, free-molecule-like, rotational lines in the spectra [5, 25, 27, 55, 61, 62]. This decoupling has been attributed to a new phenomenon, microscopic superfluidity.

The relationship between microscopic superfluidity and bulk superfluidity remains largely unexplored. The onset of microscopic superfluidity is indicated by a nonclassical turnaround and subsequent increase in the effective rotational constant (B_{eff}) of the molecule (a decrease in the effective moment of inertia) as the number (N) of solvent particles is increased [21, 25, 55, 103]. This indicates a decoupling of the helium density from the rotational motion of the dopant molecule. Often discussion of microscopic superfluidity will adopt the language of the two-fluid theory of Tisza and Landau [55–59], in which the helium or $para\text{-H}_2$ density surrounding the dopant molecule will consist of a normal fluid and a superfluid fraction. Path integral Monte Carlo (PIMC) studies of small CO doped $para\text{-H}_2$ droplets have observed microscopic superfluidity in clusters containing as few as 6 $para\text{-H}_2$ molecules, with both the superfluid and the normal fraction coexisting [25]. The PIMC calculations found the at the superfluid fraction declined from roughly 95% at $N = 1$ to approximately 82% at $N = 6$, followed by an increase to essentially 100% for $N > 10$, which is congruent with experimental results. However, since PIMC simulates the properties of a superfluid by projecting the system

in question onto a classical analogy [62], it is difficult to get an understanding of the actual quantum behavior. It is very difficult, for example, to conceptualize how there could exist a normal and a superfluid fraction for a $N = 1$ cluster [55].

The goal of the study is to gain insight into the physics that result in microscopic superfluidity. There is no standard definition on microscopic superfluidity [131] and the mechanisms that lead to the decoupling have been studied only once before [121].

4.3 Genetic algorithm

Genetic algorithms are a subset of evolutionary algorithms that model biological processes to optimize highly complex functions [98]. The method was developed by John Holland and popularized by his student David Goldberg who was able to solve a difficult problem involving the control of gas pipeline transmission for his dissertation [154]. The key idea of employing the GA in this project is to have it hone in on the nodal hypersurfaces of the $^4\text{He-HCN}$ excited states during the DMC calculation itself. Genetic algorithms are an efficient and accurate method of finding extrema in high-dimension spaces. The GA begins by creating a population of candidate solutions (individuals) that are then evaluated against a user defined fitness function. Each individual is a representation of a guess at a possible solution to the problem. The initial population is evaluated against the fitness function. The individuals that perform the best against the fitness function are then allowed to interbreed and mutate. The algorithm terminates after a specific, user specified, number of generations have been propagated. If a satisfactory solution has not been attained, the last generation may be used as the starting point for the evolution of future generations.

The two most important factors in setting up the GA are (i) encoding a representation of a potential solution and, (ii) defining a fitness function against which

to toes the individuals [155]. Therefore, in order to use the GA for nodal optimization we need: (i) a parameterization of the nodal surface to be available and also able to be progressively optimized by the GA and (ii) a set of optimization criteria. This allows for the population (possible solutions) to evolve to an optimal solution as governed by the user defined fitness function. In general, the nodal function may be parameterized as $\Psi = \sum_n c_n \phi_n$ where c_n are expansion coefficients and ϕ_n are a set of basis functions similar to those employed in variational calculations. The GA refines c_n using the defined optimization procedures. Since several different excited states can be represented by the same basis vectors, but with different expansion coefficients, multiple maxima may exist in the fitness function. In order to narrow down to a specific state two approaches are possible: (i) modify the fitness function so that only states within a given energy range are found and (ii) bias the c_n to target the state of interest.

In previous studies [64, 100], the optimization criteria required: (i) that the separate DMC calculations inside each pocket result in identical “pocket energies” if the node is exact and (ii) the directional flux histogram, obtained by binning the walkers before and after they cross the node, be identical. This paper improves on this procedure by using non-directional histograms in the optimization criteria instead of directional flux histograms.

4.4 On the fly computation of nodal hypersurfaces

The diffusion Monte Carlo (DMC) method is a fairly straightforward and accurate way of determining the ground state energies of quantum systems. Excellent reviews of the DMC algorithm and its implementation are available [70, 93]. Although the DMC method is numerically exact for the ground state, it is not so for excited states or fermions. Fixed node diffusion Monte Carlo (FNDMC) is one approach at adapting the DMC algorithm to calculations of excited and fermionic states. In the FNDMC method any walkers that cross a predetermined nodal

surface are eliminated. The accuracy of the results obtained using this method depend of the accuracy of the nodal topography of the trial wave function used to guide the calculations. In this respect the FNDMC algorithm is somewhat paradoxical in nature; to be able to perform excited state calculation of an unknown wave function one must have prior knowledge of the nodal topology of this unknown wave function. While symmetry and other approximations may be used to estimate the topology of the node, there has not been until very recently [121], a systematic method of determining nodal hypersurfaces. Past studies within this group [101, 121, 156] have begun the development, implementation and testing of a new approach that allows for the systematic computation of nodal hypersurfaces on the fly within DMC calculations.

On the fly computation of the the nodal hypersurfaces of the $^4\text{He-HCN}$ wave functions are done using a genetic algorithm (GA). This new algorithm improves on the optimization criteria proposed by Lüchow and co-workers [90, 102]. The criteria is based on the hypothesis that if the true wave function is governed by $\hat{H}\Psi = (\hat{T} + V)\Psi = E\Psi$ where \hat{T} is the kinetic energy operator, then the functions Ψ_T , $\hat{T}\Psi_T$ and $\hat{H}\Psi_T$ will have the same nodal hypersurface if the the trial wave function Ψ_T is exact. Therefore, one should be able to optimize the nodal hypersurface of the trial wave function by minimizing the differences between Ψ_T , $\hat{T}\Psi_T$ and $\hat{H}\Psi_T$. There are, however, a number of problems with this approach: (i) to derive explicit expressions for the distances between the nodal hypersurfaces the surfaces must be close to each other and locally parallel, (ii) while Ψ_T and $\hat{T}\Psi_T$ will have nodes in common when Ψ_T is an eigenfunction, it is possible for $\hat{T}\Psi_T$ to have additional nodes, and (iii) it possible for functions to exist that are not eigenfunctions but are such that $\hat{H}\Psi_T$ and Ψ_T have nearly identical nodes. To by pass these problems we developed a new algorithm that searches for the nodal topology of a wave function within the DMC calculations. It is as follows:

1. A genetic algorithm (GA) generates a random population of trial wave functions based on a user defined parameterization of the node.
2. For every Ψ_T a new function $\Xi_T = \hat{H}\Psi_T$ is formed.
3. Two DMC calculations, corresponding to regions where $\Psi_T > 0$ and $\Psi_T < 0$, are performed, yielding two pocket energies E_{Ψ}^+ and E_{Ψ}^- .
4. Step 3 is then repeated with Ξ_T in place of Ψ_T , yielding two energies E_{Ξ}^+ and E_{Ξ}^- .
5. Flux histogram are accumulated throughout the DMC calculations as walkers cross the nodal surfaces of Ψ_T and Ξ_T independent of direction.
6. If Ψ_T is an exact eigenfunction then all the pocket energies and the histograms will be identical. The goal of the GA is to iterate to a Ψ_T that fulfills this criterion.

The fitness function is also user defined. In this case it requires that: (i) near equality of pocket energies with small standard deviations, (ii) minimizing the standard deviation between the energies E_{Ψ}^+ , E_{Ψ}^- , E_{Ξ}^+ and E_{Ξ}^- , and (iii) minimizing the differences between the flux histograms.

4.5 Epochal GA-DMC

In practice, an epochal GA-DMC procedure was used during the nodal optimization process. The procedure was as follows:

1. The first epoch uses a relatively small number of walkers and a large time step during the DMC calculations. A given number of generations are evolved, usually several hundred. In general, the specific values of walkers, time step and generations are determined by the problem at hand through initial experimentations.

2. At the end of the first epoch the individuals with the highest fitness are examined. Usually, the high fitness functions will cluster around one or more excited states. The approximate value of the energy of interest is estimated and a new fitness function is defined which is biased against those states outside of the energy range of interest. This is done using an energy cutoff outside of which the fitness function is set to zero.
3. A second epoch GA run is then performed. This time the number of walkers used in the DMC calculations are increased and the time step is decreased.
4. The process is repeated for a number of epochs until satisfactory convergence and standard errors are attained. The number of generations evolved for the later epochs is reduced to decrease the overall computer time.
5. Convergence is achieved when the energies have converged as a function of fitness. This is done by defining a fitness cut off, f_{cut} ; only individuals with fitness greater than f_{cut} , $f > f_{cut}$, are included in computing the average DMC energy. The calculation is considered converged once the energies are stabilized as a function of varying f_{cut} .

4.6 Computer methodology: fine grained parallel genetic algorithm

The GA method involves two basic procedures: (i) evaluating the fitness function and (ii) applying the genetic operators to each generation after calculation of the fitness function. The most computationally demanding step is evaluation of the fitness function. 99% of the computer time, in fact, is consumed in computing the fitness function. To increase efficiency, each GA individual is farmed out to a separate cpu core while a master cpu takes care of the GA related functions. It is natural then to send one individual to each available thread. In this study, 5×4-core HP 3130 Linux machines capable of hyper threading (two thread per core) were used. This approach is known as fine graining. Each of the DMC calculations

done for each individual guess at the node, if done on identical processors, are quite similar in speed. This makes parallelization computationally efficient with little idle time for any given cpu core. Maximal efficiency in the calculations is attained by choosing a population size that is the same as the number of available core (or possibly threads).

4.7 Reduced dimensionality models

It has been demonstrated that the physics of microscopic superfluidity in bosonic solvents is quite similar to that of a stirred Tonks-Girardeau (TG) gas with the barrier replaced by a rotating impurity molecule [121]. A TG gas is a one dimensional gas of impenetrable bosons constrained to a ring of finite circumference. Theoretical studies have shown that the TG gas displays a critical velocity below which the system is hard to stir [104–106] which is a characteristic of a superfluid. This similarity enables us to do two things: (i) construct reduced-dimensionality models of the ^4He -HCN system with the the ^4He atoms confined to a ring (bosons-on-a-ring model (BOAR)) [121] to use in our calculations and, (ii) to model the system as a stirred TG gas, which allows us to be able to solve for the N-body-time-dependent Schrödinger equations numerically when calculating the particle current density. The particle current is calculated to determine whether there is any superfluid behavior. The one dimensional model enables us to perform accurate quantum basis set calculations for $N \leq 5$.

The BOAR Hamiltonian is given by

$$\hat{H} = \frac{\hat{j}_z^2}{2I_{HCN}} + \sum_{i=1}^N \left[\frac{\hat{l}_{iz}^2}{2mR_0^2} + v(\psi_i - \theta) \right] + \sum_{ik}^N U(\psi_i - \psi_k) \quad (4.1)$$

where I_{HCN} is the moment of inertia of the HCN molecule and \hat{j}_z is the molecular rotational angular momentum (AM) operator. The moment of inertia I_0 is defined as $I_0 = mR_0^2$ and given by the quantity $\frac{\hbar^2}{2mR_0^2} \sim 0.19 \text{ cm}^{-1}$; \hat{l}_{iz} is the orbital AM

operator for the i^{th} ^4He atom (mass m), and ϕ_i and θ are the azimuthal angles of the HCN molecule and the i^{th} ^4He atom [121]. $V(\phi_i - \theta)$ is the atom-molecule potential energy surface (PES) and $U(\phi_i - \theta_k)$ is the He-He PES. The gas phase rotational constant for HCN is $B_0 = 1.47822 \text{ cm}^{-1}$. The masses of HCN and He are 27.011 amu and 4.00260 amu respectively. All the DMC calculations were performed using the rigid-body approximation.

4.8 Potential energy surface (PES)

Three different He-He PES were used: (i) the He-He PES of Aziz, McCourt and Wong (AMcW) [135], (ii) a purely repulsive Gaussian barrier, given by $U_{\text{He-He}}^g(\phi_{ij}) = g_0 e^{-\alpha\phi_{ij}^2}$, where ϕ_{ij} is the angle between the i th and j th ^4He atoms, and (iii) a δ -function potential similar to that of the TG gas. The Gaussian barrier lies somewhere between the AMcW PES and the TG limit; a soft barrier will be closer to the actual van der Waals radius of the ^4He atoms, whereas a hard barrier is closer to the TG limit of a δ -function with strength going to infinity [131]. The Gaussian barrier also has the advantage of simplifying the calculation of matrix elements compared to the AMcW PES. In order to simplify the Hamiltonian of the system further, only the first three dominant terms of the ^4He -HCN PES expansion in Legendre polynomials is retained, i.e., $V(R, \Theta) = \sum_{n=0}^{n=2} V_n(R_0) P_n(\cos\theta)$ where $\Theta = \phi_i - \theta$.

4.9 Results and conclusions

Figure 4.1 shows data from simulations using BOAR models (main panel) and BOAS(insert). B_{eff} is defined as half of the energy difference between the ground state and the lowest excited a -type state [21, 100]. All computations were done using fixed-node diffusion Monte Carlo (FN-DMC) coupled to a genetic algorithm (GA)[100, 156], and using the AMcW PES, and a soft, intermediate and hard Gaussian barrier on the BOAR and BOAS model. The BOAS Hamiltonian is closer to the full problem Hamiltonian than the BOAR; it better depicts the ^4He

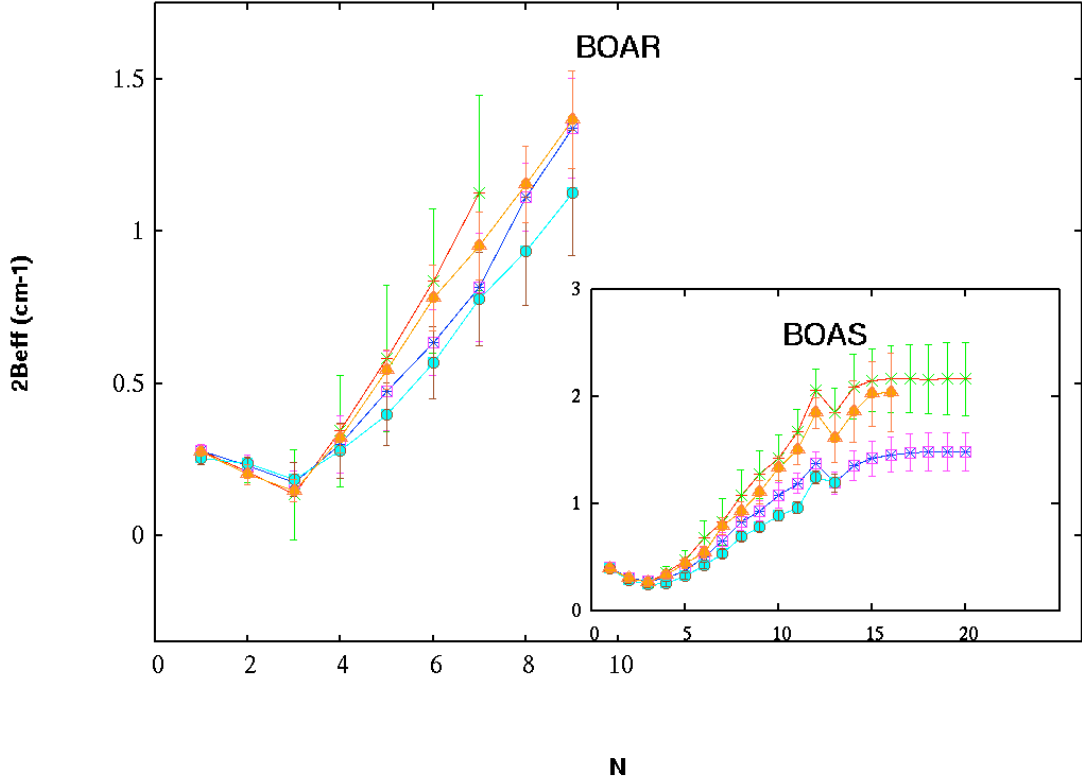


FIG. 4.1 (color online). Energy splittings ($2B_{eff}$) for a -type, $J = 1-0$ rotational transitions as a function of the number of ^4He atoms (N). The main panel shows data from the BOARs simulations. The results show data gathered using: AMcW PES (green asterisks); three different forms of the Gaussian barrier: $g_0 = 100\text{cm}^{-1}$, $\alpha = 40\text{rad}^{-1}$ (soft barrier, orange triangles); $g_0 = 100\text{cm}^{-1}$, $\alpha = 500\text{rad}^{-1}$ (medium barrier, purple open squares); $g_0 = 500\text{cm}^{-1}$, $\alpha = 750\text{rad}^{-1}$ (hard barrier, blue circles); , with the error bars. The lower inset show data from the BOAS simulations. Both the AMcW PES and the Gaussian barrier capture the trend of the effective rotational constant (B_{eff}) with increasing helium atoms (N), i.e., a gradual decrease in B_{eff} , then a subsequent turn around at $N = 3$.

density distribution in three dimensions. The BOAS results were done to illustrate how well the reduced dimensionality models captured the physics of the system. All data was compared to those obtained experimentally. Both models capture the initial decrease of B_{eff} with a turnaround at $N = 3$. The trend is observed even when the AMcW potential is replaced by the purely repulsive Gaussian barrier, which leads us to conclude that the decoupling mechanism is primarily due to the

repulsive solvent-solvent interactions. This result agrees with that of an earlier study on ^4He -CO microscopic superfluidity [121].

4.10 Acknowledgments

This work was supported, in part, by grant CHE1300504 from the National Science Foundation to Utah State University.

CHAPTER 5
RENORMALIZATION OF THE ROTATIONAL CONSTANTS OF NH₃
SEEDED IN SMALL ⁴HE CLUSTERS

5.1 Abstract

The solvation dynamics of NH₃ molecule seeded into a droplet of ⁴He containing $N = 1-25$ ⁴He atoms are studied using diffusion Monte Carlo method for ground state calculations and fixed node diffusion Monte Carlo method for excited state calculations. The investigation centers around the $|0011\rangle$ states using anisotropic nodes. The accurate rotational constants ($B_0 = 9.945 \text{ cm}^{-1}$, $C_0 = 6.229 \text{ cm}^{-1}$) and “fudged” versions of the rotational constants ($B_{fudged} = 0.9945 \text{ cm}^{-1}$, $C_{fudged} = 0.6229 \text{ cm}^{-1}$) are used. Neither the accurate or fudged rotational constant of this state exhibited the turn around behavior, i.e. initial decrease than a subsequent increase with increasing number of ⁴He atoms, that is characteristic of the onset of microscopic superfluidity. The reduction in B_0 calculated using the accurate rotational constants for the ammonia molecule for the $|0011\rangle$ state, about 34% , is much higher than expected and requires further investigation. The fudged rotational constants are in an indeterminate range between the light and heavy rotors. The fudged rotational constants experience slightly smaller renormalization than the accurate rotational constants. This may be attributed to the importance of molecular anisotropy versus the size of the rotational constants in molecules whose rotational constants fall in an intermediate regime.

5.2 Introduction

Helium is a singularly unique substance with special properties. It has no triple point and was the first material observed to exist as a liquid at arbitrarily close to absolute zero [6, 57, 157, 158]. Although the study of helium has a long history, going as far back as 1908, a new phase in the study of helium was triggered by the creation of technology that allowed helium nanodroplets to be used

for cluster isolation spectroscopy and microscopic Andronikashvili experiments. In this early Andronikashvili-type experiments, with OCS and SF₆ dopant molecules, sharp rotational features, characteristic of free (gas-phase) molecular rotation, were observed but with reduced (renormalized) rotational constants. SF₆, for example, had a renormalized constant that was $\frac{1}{3}$ of its gas phase value. This behavior, to varying degrees, seemed to be the norm for molecules doped into ⁴He droplets. The rotational resolved spectra were however not observed in fermionic ³He clusters. These findings were taken to imply that free rotation of the dopant molecule is a consequence of the superfluidity of the bosonic ⁴He clusters [2].

Several studies have been done with the goal of understanding how the properties of a system affect the renormalization constants. Generally, light rotors, for example HF, H₂O and NH₃, experience smaller renormalization. This is largely due to the fact that light rotors have large rotational constants which in effect leads them to average the interaction potential so that the rotor appears to the ⁴He atoms as if the potential were spatially isotropic. In isotropic potentials the angular momentum quantum numbers for the molecule and the atom are conserved separately; in the case of light rotors (since the potential is not exactly isotropic), the angular momentum of the molecule and atom are not conserved separately but the angular momentum transfer between the dopant molecule and the ⁴He atoms is relatively ineffective. In contrast, for heavy rotors a fraction of the helium density is able to follow the rotor adiabatically which results in the large renormalization. This generalized trend has been shown as an effective model by several studies [111, 112, 115].

The extent of renormalization can be expressed as $\Delta = \frac{B}{B_0}$, where B₀ is the free molecule rotational constant and B is the renormalized constant observed in the ⁴He droplet [115]. There have been deviations to the trends stated above. For example, in a computational study of HF, HCl and HBr in ⁴He nanodroplets the renormalization observed for HF was larger than that calculated for HBr and

HCl despite the fact that of the three molecules HF has the largest gas-phase rotational constant. The values Δ for HF, HCl and HBr were 0.98, 1, 1 respectively. The greater renormalization of the HF molecule was attributed to the slightly stronger anisotropic He-HF intermolecular potential. The effect of the molecular anisotropy in this series of molecules, HX, though present seems to be relatively weak in comparison to the renormalization induced by the size of the rotational constants. The effects of anisotropy were observed as weak in a path integral Monte Carlo (PIMC) simulation of the rotational dynamics of CH₄ using the true rotational constant of the molecule $B_0 = 5.1 \text{ cm}^{-1}$ and a “fudged” version $B_f = 0.105 \text{ cm}^{-1}$. Altering the rotational constants makes it possible to sort the kinetic versus the potential anisotropic factors in the behavior of the molecule. B_f exhibits a greater anisotropic potential than B_0 . B_0 , on the other hand, appears to be essentially isotropic due to orientational averaging. For B_0 the CH₄ molecule is almost completely decoupled from the ⁴He droplet. The results for B_f are similar to those of SF₆ ($B_0 = 0.091 \text{ cm}^{-1}$). This shows that in light rotors renormalization is not directly the result of adiabatic following. However, it is important to note that other studies [159] have reached conclusions that directly contradict this, i.e. that the molecular anisotropy is in fact more important than the size of the rotational constants and not vice versa.

The extent of renormalization of the rotational constants is also determined by the rate at which the cluster attains its saturated value (nanodroplet limit) as a function of the number of helium atoms. Saturation has been shown to occur with as few as $N = 8$ ⁴He atoms [112]. The rapid onset of saturation has been attributed to the phenomenon of adiabatic following. In adiabatic following the ⁴He atoms respond almost instantaneously to the motion of the doped molecule. This means that the doped molecule in essence carries a “coating” of the ⁴He density along with it. The interaction of the “molecule + coating” experiences a much more isotropic interaction than the rest of the solvent as the number of ⁴He atoms increased. Once

the coating is completed, saturation occurs quickly as a function of the number of helium atoms (N). Light rotors, i.e., rotors with large rotational constants, have very little adiabatic following. We instead consider the hypothetical limit in which the potential is isotropic, known as the isotropic binary complex (IBC), in which there is no possibility of angular momentum exchange between the molecule and solvent atoms and so the nanodroplet should, theoretically, be arrived at immediately. This suggests that light rotors achieve saturation relatively quickly due to fast orientational averaging of the potential.

While fast saturation has been observed in previous computational studies for several light rotors: HF, HCl and HBr [113] and CH_4 [114] for example, ambiguous results and even results that contradict the expected behavior of light rotors as it pertains to saturation have also been observed. HCN, for example, which is a light rotor exhibited three different rates of saturation under three different studies. In projection operation calculations [76], HCN had a relatively slow approach to the nanodroplet limit, i.e. requiring the participation of ^4He atoms outside the first solvation shell. However, in reptation Monte Carlo calculations [159] and adiabatic node DMC (ANDMC) calculations [113] the saturation occurred relatively quickly, i.e., within the first solvation shell. The unexpected results observed in Ref. [76] was explained in a later study as being the result of coupling of the HCN rotation to the collective excitations of the ^4He atoms [160]. This results were then later contradicted by another study by Moroni and Baroni [161] who had found that the nanodroplet limit was in fact reached within the first solvation shell. Similar discrepancies between the theorized results and actual results have been observed in a study of the $^4\text{He}_N\text{-CO}$ system [25]. The experimental study found the effective rotational constant of the CO molecule to be $\sim 0.74\%$ of its gas-phase value when $N = 14$ (i.e., $\Delta = 0.74$) (in excellent agreement with results obtained from computational simulations [162]) but a smaller renormalization constant than the $\Delta = 0.63$ inferred from the nanodroplet experiments [25, 163]. CO

($B_0 = 1.923 \text{ cm}^{-1}$) is expected to behave in a similar fashion to HCN ($B_0 = 1.478 \text{ cm}^{-1}$) which has a $\Delta = 0.80$ at the nanodroplet limit. However, as pointed out by Raston et al. [25], the experimental nanodroplet value of the rotational constant (B) is much more accurately known for HCN than for CO; therefore, the observed discrepancy in the HCN results may be due to the value of B used and not the behavior of the molecule.

While the above results give an ambiguous overall picture for light rotors, it should be noted that the rotational constants of the two molecules studied, HCN and CO, are not exceptionally large when compared to those of HF, HCl, HBr, H₂O, NH₃ and CH₄. It is possible then that anisotropy is only important in an intermediate regime of rotational constants, one in which the molecular anisotropy competes with size of the rotational constants in determining the behavior of the molecule.

Recent experimental studies have employed the angular momentum of the bosonic solvent in their study of the renormalization of the rotational constants of different molecules seeded into ⁴He droplets. To determine the accuracy of the results they obtained and gain further insight into the mechanism that leads to renormalization of rotational constants, we conducted fixed node diffusion Monte Carlo (FNDMC) calculations on the ammonia molecule doped into ⁴He droplets. NH₃ is a light rotor ($B_0 = 9.9455 \text{ cm}^{-1}$ and $C_0 = 6.229 \text{ cm}^{-1}$) and has a potential that is not strongly anisotropic. A brief overview on the methodology and discussion on the results is presented below.

5.3 Hamiltonian

Three Euler angles, (α, β, γ) , define the orientation of the NH₃ molecule (mass M) and two more, (θ_i, ϕ_i) , specify the angular location of the i^{th} ⁴He atom in the space fixed frame, neglecting three body effects. The distance of the i^{th} ⁴He atom from the center of mass of NH₃ is R_i . If the NH₃ molecule is rigid then the

potential energy surface (PES) is $V(R_i, \Theta_{il}, \Phi_{il})$, where Θ_{il} and Φ_{il} are spherical polar angles in an axis system that coincides with the principal axes of the NH_3 molecule, denoted in this paper as “I”. The polar angles relate the R-vector of the i^{th} ^4He atom to the axis system. The He- NH_3 potential used was outlined by Hodges and Whitley [164] while the PES of the He-He interaction is that of Aziz and Slaman [135, 165]. In the potential from Hodges and Wheatley the N atom of the NH_3 atom is used as the origin, rather than the center of mass of the NH_3 molecule which must be accounted for in the calculations. The mass of NH_3 and ^4He used were 17.0305 a.u. and 4.00260 a.u. respectively, and the gas phase rotational constants of NH_3 used were $B_0 = 9.945 \text{ cm}^{-1}$ and $C_0 = 6.229 \text{ cm}^{-1}$. The umbrella angle of the NH_3 molecule was fixed at 112.14° . In the space fixed frame the Hamiltonian is given as:

$$H = \frac{-\hbar^2}{2M} \delta_i^2 - \frac{\hbar^2}{2m} + H_I + \sum_{i < j}^N V_{\text{He}}^{\text{He}}(r_{ij}) + \sum_{i=1}^N V(R_I, \Theta_{il}, \Psi_{il}), \quad (5.1)$$

where

$$H_I = B_0 j^2 + (C_0 - B_0) j_z^2, \quad (5.2)$$

and j is the angular momentum vector of the molecule.

5.3.1 Nodal functions

It is important to study carefully the nodal structures of the excited rotational states since knowledge of these states are crucial in fixed-node DMC calculations. Furthermore, the conflicting experimental results obtained for this complex in regards to the extent of renormalization also dictates that a thorough investigation of nodal hypersurfaces is done. Given the relatively large rotational gas phase constants of NH_3 it would seem reasonable that using a “isotropic-node” (a nodal

function appropriate to the IBC) would be sufficient. However, the experimental results [33] imply significant state mixing and, therefore, a potentially significant distortion of the nodal topologies in the excited states. The calculations in this study were therefore done using isotropic nodal functions as well as adiabatic nodal functions.

5.3.1.1 Isotropic nodal functions

The potential in these $^4\text{He-NH}_3$ complex nodal functions are assumed to be isotropic. The interaction potential, for a single ^4He atoms, can therefore be expanded in terms of renormalized spherical harmonics $C_{nm}(\Theta, \Psi)$ [166]:

$$V(R, \Theta, \Psi) = \sum_{nm} V_{nm} C_{nm}(\Theta, \Psi) \quad (5.3)$$

$V_{nm}(R)$ are known as radial strength functions. If only the strength function with $n = m = 0$ is retained then the IBC is obtained. In the space-fixed frame, after separation of the center of mass, the eigenfunctions of the IBC have the form

$$\Phi_{\sigma}^{JM} = X_{jkL}^{J\sigma}(R) Y_L^{m_l}(\theta, \psi) \psi_{m_j, k}^j(\alpha, \beta, \gamma) \quad (5.4)$$

where $Y_L^{m_l}$ is a spherical harmonic and L, m_l are the angular momentum quantum numbers of the complex, i.e., the end-over-end angular quantum numbers; $\phi_{m_j, k}^j$ is a normalized rotation matrix and j, m_j, k are the usual symmetric top quantum numbers of the monomer, i.e., the quantum numbers of the free NH_3 molecule in the space-fixed frame [94, 166–168]; J, M are the quantum number corresponding to the total angular momentum numbers of the complex; the Euler angles, α, β, γ , specify the orientation of the monomer in the space-fixed frame while the angles, θ, ψ , specify the orientation of the vector from the center of mass of the monomer to the ^4He atom in the space fixed frame.

The angular nodal function of the IBC correspond to the angular part of Eq. (5.4). They are, in general, the nodes of a product of spherical harmonic and a rotation matrix and so are available analytically. The wave function of more than a single ^4He atom, in the isotropic limit, are a generalization of those for the IBC and the nodes are easily computed.

The degree of similarity of the nodes of the actual anisotropic complex to the of the IBC depends on the degree of anisotropy of the potential as reflected in the higher order radial strength functions. In the case of HCN dopants, for example, using IBC nodes in fixed-node DMC calculations produces very poor results [76, 101, 113]. Therefore, it is important that we also consider a study of the $^4\text{He-NH}_3$ nodal structure using a method that relies on an adiabatic separation of the radial and angular motions [101, 111, 113].

5.3.1.2 Adiabatic nodal functions

The adiabatic node DMC (ANDMC) procedure is based of that of Holmgren et al. [155], in which an adiabatic, i.e., Born-Oppenheimer-like, angular-radial separation (BOARS) is made in the molecule fixed frame. The radial degree of freedom is frozen at some value $R = R_0$ and the angular portion of the resulting Schrödinger equation is then solved. This procedure is then repeated for different values of R_0 which generates families of adiabatic radial potentials. The adiabatic potentials are then used to solve for the radial wave functions. This method generates a good estimate of the nodal surfaces for small helium clusters and is also computationally quite efficient because the angular matrix elements can be computed analytically or semi-analytically [169, 170].

The adiabatic Hamiltonian for $N = 1$ in a center of mass coordinate system of the dimer is as follows:

$$H_{adiabatic} = H_l + kl^2 + V(R_0, \Theta, \Psi) \quad (5.5)$$

where $k = \frac{1}{2\mu R_0^2}$, l is the orbital angular momentum of the complex and μ is the reduced mass. Diagonalization of $H_{adiabatic}$ at fixed J and N produces estimates for the nodes. The basis function used have the same form as in Eq. (5.4) but with R frozen at $R = R_0$.

The solutions for Eq. (5.5) for a series of R_0 values yield a set of effective potentials which are then used to solve for the radial function $\tau (R)$ and eigenvalues. The value of R_0 used to calculate the nodal topology of the angular wave function was calculated as the expectation value of R for the appropriate radial eigenfunction in the BOARS procedure. This procedure yields $R_0 = 9.1$ a.u.

The ground and excited ($J = 1$) states were computed using nodal functions for the hypothetical isotropic complex, adiabatic nodal functions and coupled channel calculations obtained using the program BOUND [171]. The results are shown in Table 5.1 and Table 5.2

5.4 Importance sampling

In importance sampling a trial wave function, Ψ_T , is used to guide the DMC walkers. Utilizing importance sampling in DMC calculations has a number of advantages: (i) it increases the precision of the computed energies, (ii) it improves the efficiency of the method, and (iii) it prevents dissociation for clusters containing large numbers of ^4He atoms [70]. Use of the guiding trial wave function results in a diffusion-like equation for the mixed function $f(R, r_i)$ where R and r_i are the molecular and ^4He atom coordinates respectively. Quantum forces, additional drift terms, are employed to guide the walkers during the diffusive process to regions of high probability density [72]. The trial wave functions were chosen to have the form:

$$\Psi_T = \{\prod_{i=1}^N f(R_i) \prod_{i \neq j}^N \Xi(r_{ij})\} \Upsilon(\Omega, \theta_i, \psi_i), \quad (5.6)$$

where Ω denotes the Euler angles and θ_i, ψ_i are spherical polar angles of the i th ${}^4\text{He}$ atoms referred to in space fixed axes. The radial functions were chosen to have the form [76, 112, 113, 116]:

$$f(R) = be^{(-\frac{c}{R^5} - aR)}, \quad (5.7)$$

where the parameters a, b, c were obtained by fitting the function $f(R)$ to adiabatic nodal functions. Υ is set to unity for ground state calculations; it contains the nodal topology for the excited state wave functions. $\Xi(r_{ij})$, the ${}^4\text{He}$ - ${}^4\text{He}$ portion of the trial wave function, is used in previous studies [111].

5.5 Recrossing correction

FNDMC calculations use a finite-sized time step. Due to this there is the possibility that a walker crosses and recrosses the nodal surface within a single time step which results in artificially lowered excited state energies. To avoid this, the walkers that recross a node are eliminated using a recrossing correction [172]. In this study, a modified version of the recrossing correction outlined by Petite and McCoy [172] is used; Eqs. (10) - (12) from Petite and McCoy are used but with the intramolecular vibrations of the rotor frozen. The general expression for the probability that a walker should be removed from the simulation because it has crossed and recrossed a particular node during the time step from τ to $\tau + \delta\tau$ is

$$P_{recross} = e^{[-\frac{m_{eff}d(\tau)d(\tau+\delta\tau)}{\delta\tau}]} \quad (5.8)$$

where m_{eff} is the effective mass associated with the nodal coordinate and $d(\tau)$ is the distance from the nodal surface at imaginary time τ [67]. The Euler angles $\{\theta, \chi, \phi\}$, for a rigid body, transform a set of space axes, whose origin is fixed at the center of mass, into the chosen body-fixed axis system. Since the nodal

surfaces are defined here as $\theta = \theta_{node}$ or $\chi = \chi_{node}$, the distances in Eq. (5.8) will be $d(\tau) = \theta(\tau) - \theta_{node}$ or $d(\tau) = \chi(\tau) - \chi_{node}$, where the angles are all measured in radians. For symmetric rotors, m_{eff} for a node in θ is defined as:

$$m_{eff,\theta} = \left[\frac{I_{AA}(\tau) + I_{BB}(\tau)}{2} \right] \left[\frac{I_{AA}(\tau + \delta\tau) + I_{BB}(\tau + \delta\tau)}{2} \right] \quad (5.9)$$

while for a node in χ , m_{eff} is defined as:

$$m_{eff} = I_{CC}(\tau)I_{CC}(\tau + \delta\tau) \quad (5.10)$$

5.6 Computational details

The calculations were done using 10,000 walkers with continuous weighting. The time step value, $\Delta\tau$, was selected to be 20 a.u. for the ground state calculations and 5 a.u for excited state calculations. A total run of 350,000 steps was done to ensure convergence.

5.7 Results

This study focused mainly on the behavior of the $|0011\rangle$ excited state. In this labeling scheme $|jklJ\rangle$, j is the orbital angular momentum of the molecule; k is the orbital angular momentum of the complex; l is the orbital angular momentum of the ^4He atoms and J is the total angular momentum. For the $|0011\rangle$ state the rotational constants of note are the orbital angular momentum of the ^4He atoms. The effective rotational constant of the state were computed at each cluster size, by comparing the difference between the ground and the excited state energy of the $|0011\rangle$ state using the accurate rotational constants- see Table 5.1- and the fudged rotational constants shown in Table 5.2 to the corresponding expressions for a pure symmetric top. The equations used to solve for the renormalized rotational

constants B and C are

$$E_{JK} = J(J+1)\frac{\hbar^2}{2I_b} + K^2\hbar^2\left(\frac{1}{2I_A} - \frac{1}{2I_b}\right) \quad (5.11)$$

and

$$B_e = \frac{h}{4\pi^2 I_e c} \quad (5.12)$$

where J and K are angular momentum operators. The inertia components satisfy $I_a I_b = I_c$ and B_e is the rotational constant.

The rotational constant B_e obtained using the accurate rotational constants ($B_0 = 9.945 \text{ cm}^{-1}$, $C_0 = 6.229 \text{ cm}^{-1}$) and using the “fudged” versions of the rotational constants ($B_{fudged} = 0.9945 \text{ cm}^{-1}$, $C_{fudged} = 0.6229 \text{ cm}^{-1}$) are shown in Fig 5.1 for the state $|0011\rangle$. The fudged rotational constants were in an indeterminate range between the light and heavy rotors. While both show a reduction in the renormalization constants the simulations done with the fudged rotational constants experienced a slightly smaller reduction than those done using the accurate rotational constants. This may be attributed to the importance of molecular anisotropy versus the size of the rotational constants in molecules whose rotational constants fall in an intermediate regime. It is possible that, in this intermediate regime of the fudged rotational constants of the NH_3 molecule studied, the effects of the molecular anisotropy govern the extent of renormalization much more than the size of the bare gas rotational constant. The $^4\text{He-NH}_3$ intramolecular potential energy is dominated by the isotropic radial strength function V_{00} [115]. Thus the weak anisotropy of the He- NH_3 intermolecular potential results in a small reduction of the gas phase rotational constant B_0 . This confirms an earlier theory suggested by Suárez et al. [115] that in intermediately sized rotational constants there exists a complex interplay between the effect of the size of the gas-phase

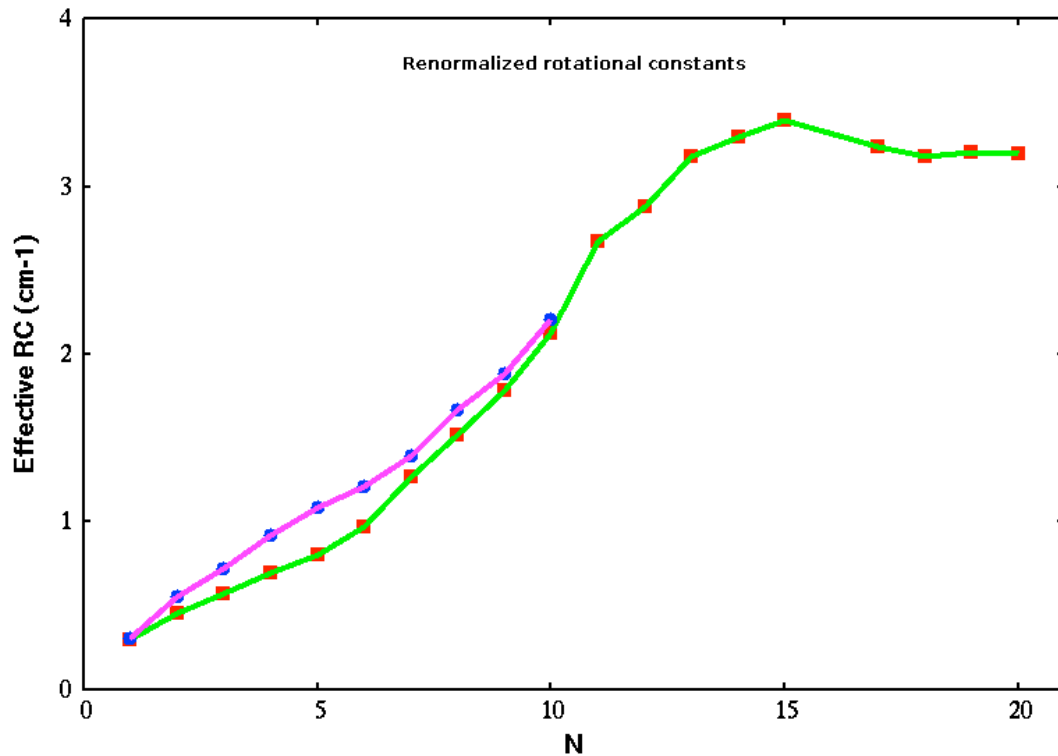


FIG. 5.1 (color online). Renormalized rotational constants (RC) for NH_3 as a function of the number, N , of ^4He atoms. The filled red squares show the B rotational constant obtained using the accurate rotational constants ($B_0 = 9.945 \text{ cm}^{-1}$, $C_0 = 6.229 \text{ cm}^{-1}$) and the filled blue circles are the B rotational constants found using the “fudged” versions of the rotational constants ($B_{fudged} = 0.9945 \text{ cm}^{-1}$, $C_{fudged} = 0.6229 \text{ cm}^{-1}$). These results were obtained using the IBC nodes corresponding to the $|0011\rangle$ state.

rotational constant of the molecule and the anisotropic contributions to the atom-molecule potential energy that makes it very hard to predict the extent or the rate of renormalization based solely on the knowledge of the size of the gas-phase rotational constants and the degree of anisotropy of the potential.

The reduction in B_0 calculated using the accurate rotational constants for the ammonia molecule for the $|0011\rangle$ state, about 34% achieved for $N \sim 15-20$, was much higher than that found by Slipchenko and Vilesov [35], Suárez et al. [115], a 3% reduction of B_0 and even the controversial finding by Behrens et al. [33] of a reduction of $\sim 25\%$. This discrepancy might be due to the state used for

the simulations, i.e., the fact that the calculations for the B_0 was based off of the excited state energies calculated for the $|0011\rangle$ state. This, to our knowledge, is the first time that simulations of the $^4\text{He-NH}_3$ complex have been done primarily using the ^4He angular momentum. The results also show that the rate of renormalization as a function of N was relatively fast. The nanodroplet limit was attained within the first solvation shell. It should be noted that while saturation occurs within the first solvation shell, the rate of convergence to the nanodroplet limit within that shell is slower for light rotors than for heavy rotors. This slower rate of saturation, comparative to the molecules with smaller rotational constants, was also noted by Suárez et al. [115]. Light rotors have large rotational constants which in turn means that they have more rotational energy in the system for any given value of J . Therefore, depending on the degree of molecule anisotropy, a larger number of solvent atoms might be needed to equilibrate this angular momentum and reach saturation.

The main conclusion of this study is that the “rule-of-thumb” theories that are used to predict the extent or the rate of renormalization for light or heavy rotors are not applicable to those rotors that fall in the intermediate regime. A new set of rules needs to be developed for these rotors. Also, while the results on the rate of renormalization were in agreement with previous studies [111, 113, 115], the data obtained for the renormalization of the rotational constants are far off from the expected values. Thus further investigations needs to be done to determine the root cause of this discrepancy.

5.8 Acknowledgments

This work was supported, in part, by grant CHE1300504 from the National Science Foundation to Utah State University.

TABLE 5.1 Ground and selected $J = 1$ excited state energies and standard errors for the ${}^4\text{He}_N\text{-NH}_3$ clusters considered for $N = 1, 20$. The rotational constants used are $B_0 = 9.945 \text{ cm}^{-1}$, $C_0 = 6.229 \text{ cm}^{-1}$. Energies are from the DMC computations.

He	$E^{0000}(\text{cm}^{-1})$	$E^{0011}(\text{cm}^{-1})$	$\Delta\text{Energy}(\text{cm}^{-1})$
1	-5.294941 ± 0.0032454	-4.704268 ± 0.00201131	0.590680 ± 0.00203732
2	-10.816842 ± 0.0054568	-9.907839 ± 0.00322129	0.909010 ± 0.00633669
3	-16.572129 ± 0.0125475	$-15.434471 \pm 0.00723680$	1.137658 ± 0.01448455
4	-22.477943 ± 0.0165846	$-21.084647 \pm 0.01025689$	1.393295 ± 0.01950007
5	-28.539917 ± 0.0153859	$-26.941385 \pm 0.01271693$	1.598527 ± 0.01996118
6	-34.772809 ± 0.0164827	$-32.830224 \pm 0.01435483$	1.942585 ± 0.02185727
7	-40.943716 ± 0.0177730	$-38.413471 \pm 0.01448251$	2.530245 ± 0.02292564
8	-47.204731 ± 0.0364123	$-44.160130 \pm 0.02056581$	3.044600 ± 0.04181875
9	-53.317812 ± 0.0430032	$-49.746168 \pm 0.03714673$	3.571644 ± 0.05682565
10	-59.216946 ± 0.0654167	$-54.973646 \pm 0.05498657$	4.243294 ± 0.08545670
11	-64.766344 ± 0.0946687	$-59.421072 \pm 0.10684566$	5.343527 ± 0.14275208
12	-69.692717 ± 0.1005689	$-63.933998 \pm 0.11602214$	5.758719 ± 0.15354230
13	-74.705026 ± 0.1200316	$-68.346411 \pm 0.10999465$	6.358641 ± 0.15947467
14	-78.108150 ± 0.1589564	$-71.515256 \pm 0.12846523$	6.592900 ± 0.16280788
15	-83.423224 ± 0.1765371	$-76.633811 \pm 0.13299465$	6.789415 ± 0.22102697
17	-89.674059 ± 0.1944356	$-83.189617 \pm 0.17686034$	6.484435 ± 0.26283984
18	-92.625574 ± 0.2015986	$-86.270892 \pm 0.19551892$	6.354582 ± 0.28083746
19	-95.018032 ± 0.2248321	$-88.614477 \pm 0.19965435$	6.403554 ± 0.30068476
20	-97.777826 ± 0.2657535	$-91.379186 \pm 0.20358954$	6.398640 ± 0.33477390

TABLE 5.2 Ground and selected $J = 1$ excited state energies and standard errors for the ${}^4\text{He}_N\text{-NH}_3$ clusters considered for $N = 1, 10$ using the “fudged” rotational constants $B_{fudged} = 0.9945 \text{ cm}^{-1}$, $C_{fudged} = 0.6229 \text{ cm}^{-1}$. Energies are from the DMC computations.

N	$E^{0000}(\text{cm}^{-1})$	$E^{0011}(\text{cm}^{-1})$	$\Delta E (\text{cm}^{-1})$
1	-6.317783 ± 0.0016220	-5.704739 ± 0.0026350	0.613044 ± 0.00309420
2	-12.785293 ± 0.0054568	-11.684794 ± 0.0042382	1.100502 ± 0.00690934
3	-19.368862 ± 0.0052481	-17.936108 ± 0.0064023	1.432754 ± 0.00827840
4	-26.029469 ± 0.0081025	-24.196897 ± 0.0095569	1.832571 ± 0.00819383
5	-32.639206 ± 0.0118965	-30.465489 ± 0.0139876	2.173717 ± 0.01836245
6	-39.176090 ± 0.0186493	-36.750274 ± 0.0166713	2.425816 ± 0.02501456
7	-45.670744 ± 0.0187012	-42.885139 ± 0.0236431	2.785610 ± 0.03014516
8	-52.035207 ± 0.0263370	-48.693062 ± 0.0325189	3.342414 ± 0.04184634
9	-58.198456 ± 0.0414089	-54.425595 ± 0.0689546	3.772860 ± 0.08043279
10	-64.010720 ± 0.0574458	-59.594215 ± 0.0674724	4.416504 ± 0.08857773
15	-85.599537 ± 0.1773056	-78.684042 ± 0.0929081	6.915495 ± 0.20017290
18	$-102.855953 \pm 0.2093145$	-96.260908 ± 0.1592199	6.646871 ± 0.26298961
20	$-114.872467 \pm 0.2931846$	$-108.322220 \pm 0.2310984$	6.550253 ± 0.37331445

CHAPTER 6

SUMMARY

Ultra cold droplets of ^4He atoms have been and continue to be of great interest in multiple scientific fields. These droplets have been utilized in a variety of ways. The ^4He droplet is used, for example, as an ultra cold ($\sim 0.38\text{K}$) matrix to study other species [28–33, 35–41], to develop new spectroscopic techniques that have greater sensitivity [53] and for atmospheric studies [173]. A long list of molecules doped into ^4He droplets have been studied, experimentally and theoretically. The question of bulk superfluidity had been tackled extensively. For example, in early “Andronikashvili-type” experiments that, using spectra, showed superfluid behavior in ^4He droplets doped with SF_6 and OCS dopants. The spectra showed sharp rotational features, characteristic of free (gas-phase) molecular rotation but with renormalized (reduced) rotational constants. In the case of SF_6 , the renormalized rotational constant was approximately one third of its gas phase value; this behavior is the norm, to varying extents, for molecules seeded into ^4He droplets [1]. Microscopic superfluidity has also been observed in helium atoms [3–13, 25, 55] and more recently in clusters of *para*- H_2 molecules [55]. Microscopic superfluidity is indicated by the nonclassical turnaround, and subsequent increase, in the effective rotational constant (B_{eff}) of the doped molecule with increasing number of ^4He atoms. This turnaround indicates a decoupling of the helium density from the rotational motion of the dopant molecule.

The physics of macroscopic superfluidity has been attributed to both Bose Einstein condensation (BEC) and superfluidity. BEC is a result of the macroscopic occupation of the same quantum state and occurs because of the underlying bose statistics. Superfluidity, however, is considered to be a hydrodynamic phenomenon characterized by zero viscosity and frictionless flow. Though similar, the two phenomena are not the same; for example, condensate and superfluid fractions are

often different. Superfluidity is fundamentally a microscopic effect and no thermodynamic limit is necessary. In fact, the signature of superfluidity has been observed in as few as 4-6 ^4He atoms [25, 61, 103]. The relationship between conventional bulk superfluidity and microscopic superfluidity has not been extensively studied. Many discussion of microscopic superfluidity use the two-fluid theory of Tisza and Landau [56] which states that below a critical temperature there exists both a superfluid and a normal fluid fraction. In a PIMC study doped $p\text{-H}_{2N}\text{-CO}$ clusters were found to have a superfluid fraction that declines from about 95% at $N = 1$ to about 82% at $N = 6$ followed by an increase to 100% for $N = 10$. 0 K quantum Monte Carlo (QMC) calculations have also predicted a turnaround in B_{eff} for CO doped in ^4He droplets; which is curious since at that temperature there should be no normal fraction of the ^4He solvent. The overarching goal of this research, as a whole, is to understand the mechanics behind the decoupling of the doped molecule from the bosonic solvent.

In order to investigate the physics behind the decoupling mechanism we first had to develop a method that would allow to ascertain the wave function nodal topology of the target complex system which would be used in our diffusion Monte Carlo (DMC) calculations. Although these systems are not large in size they still pose a challenge for computational studies since they must be treated fully quantum mechanically. Most studies employ variations on quantum Monte Carlo (QMC) methods to do so. QMC methods converge to the exact ground state of a many-body system only if that ground state wave function contains no nodes. This is the origin of the “sign problem” which complicates calculations of fermions and excited state systems. A way to combat this problem is through the use of fixed node diffusion Monte Carlo (FNDMC). The studies presented in this text were done using FNDMC. In the FNDMC method, the nodes of the wave function partition the space into pockets within which the wave function is either positive or negative. Any walkers that cross these nodes are eliminated. This means

that the energy of the system can then be calculated by performing two separate DMC calculations yielding two pocket energies, corresponding to the positive and negative configuration space of the wave function, denoted as E_+^i and E_-^i . If the nodal hypersurface used is exact the separate DMC calculations inside all of the pockets will yield the same energy. In general the FNDMC method is somewhat paradoxical, in that in order to perform any calculations prior knowledge of the nodal surface of the unknown wave function is required. While symmetry or approximations may be used to estimate the topology of the node they are not always viable options. We developed a systematic method of determining the nodal hypersurface of a wave function within the DMC calculation using a genetic algorithm.

Genetic algorithms (GA) are used to determine global extrema in high dimensional search spaces. They are particularly advantageous in that, provided the problem and a suitable fitness function can be encoded, the GA algorithm is easy to implement, portable and requires little interfacing between the GA code and the intended application. In GA simulations, possible solutions to the problem are encoded as a string of binary bit; each solution represented as an “individual” in the simulation. A population of randomly chosen individuals is generated and then evaluated against a user defined fitness function. The individuals that perform best against the fitness function are then used to generate the next generation (breeding). The new population is used in the next iteration of the algorithm. The algorithm terminates after a certain predetermined number of generations. In this way the initial guess at the solution to the problem is refined until it yields a satisfactory solution. In practice, the most important steps are (i) encoding a representation of possible solutions to the problem, and (ii) defining a fitness function against which to test the individuals. Given the observation that $\hat{H}\Psi_T = (\hat{T} + V)\Psi = E\Psi$, where \hat{T} is the kinetic energy operator and V the potential energy surface, then the functions Ψ_T , $\hat{T}\Psi_T$ and $\hat{H}\Psi_T$ should

all change signs at the same place. The optimization scheme used in this project then was based on minimizing the distances between the nodal hypersurfaces of the trial wave function Ψ_T , $\hat{T}\Psi_T$ and $\hat{H}\Psi_T$. The fitness function was defined as follows: (i) requiring the pocket energies, E_+^i and E_-^i to be equal, (ii) minimizing the distance and standard deviation between E_+^i and E_-^i and (iii) minimizing the difference between the flux histograms (generated by binning walkers that cross nodes independent of direction).

To test the viability of the genetic algorithm-diffusion Monte Carlo (GA-DMC) method, it was applied to the calculation of the excited states of a coupled quartic oscillator and the excited states of the He-C₂H₂ van der Waals complex. The algorithm was first applied to quartic oscillators with increasing complex nodal hypersurfaces. Contour plots of the exact eigenstate, obtained from Jacobi diagonalization matrix calculation and the best estimate obtained from the GA-DMC calculation were plotted and compared. The wave function from the exact eigenstate and the best variational function were used in FNDMC calculations, the resultant energies from the two were then compared. In all cases the GA-DMC calculations yielded nodal topologies and energies that were virtually indistinguishable from those of the exact eigenstate. For the highest energy state studied, additional calculations were done in which a symmetry restriction, i.e., one in which the symmetry of the Hamiltonian is exploited, was applied to the search. This was done to compare the differences between the unrestricted and restricted nodal search. The nodal surface found in the symmetry-restricted calculation was slightly superior to that in the unrestricted calculation. However, the energy difference between the two was negligible. Application was then made to calculation of several excited states of He-C₂H₂. The wave function and energies obtained using the GA-DMC algorithm were compared to those obtained via an accurate diagonalization of the He-C₂H₂ Hamiltonian. The results obtained with the GA-DMC were nearly identical to those from the diagonalization.

The results all indicate that combining a GA to the FNDMC calculations is an effective way of locating or improving nodal surfaces on the fly. While there are challenges still to be solved in using this method, for example how to deal with complications that may arise from pathologies of the nodal hypersurfaces involved, the results showed that it was a viable method of determining the nodal topology of a wave function. It was then utilized in the study of the decoupling mechanism of molecules doped into ^4He solvent.

The first case study involved ^4He clusters doped with a CO molecule. Theoretical studies have shown that a one dimensional (1D) gas of impenetrable bosons (a Tonk Girardeau gas) [104–106] constrained to a ring of finite circumference displays a critical velocity below which the system is hard to stir and a vanishing drag force; characteristics that are associated with microscopic superfluidity. A one dimensional model, with the ^4He atoms confined to a ring, referred to as bosons-on-a-ring (BOAR) was used. Originally conceived as a way to simplify the search for nodal surfaces for use in full-dimensional FNDMC calculations, the reduced dimensionality model was simply introduced and the results it yielded used to prove that it captured much of the essential physics of the system. Three forms of the He-He potential energy surface (PES) were used: (i) the accurate Aziz PES [135], (ii) a purely repulsive Gaussian barrier, and (iii) a δ -function potential as in the TG gas. The Gaussian potential interpolates between the Aziz potential and the TG limit. Two different Gaussian barriers were used: a soft barrier, which roughly models the actual van der Waals potential and a hard barrier that lies closer to the TG limit of a hard δ -function potential.

The GA-DMC algorithm was then used to compute the effective rotational constant (B_{eff}) of various ^4He cluster size. The FNDMC results obtained using the BOAR model and a 3-dimensional version in which the ^4He atoms were confined to a sphere, bosons-on-a-sphere (BOAS) were compared to experimental results. The accurate results for clusters containing less than 5 ^4He atoms were obtained

using a finite basis set consisting of bose symmetrized products of eigenfunctions of the operators \hat{j}_z and \hat{l}_{iz} . The results were as follows: (i) both the BOAR and BOAS model captured the initial decrease in B_{eff} and subsequent turn around at $N = 3$. Both sets of results agreed with the experimental results, with the BOAS data in better quantitative agreement with the experimental results, (ii) the results obtained using the two Gaussian barriers and the Aziz potential were all similar to each other and (iii) the FNDMC calculations agreed with those done using basis set calculations for $N \leq 5$. Calculations were also done for \hat{j}_z^2 as a function of cluster size (N). After an early rise, \hat{j}_z^2 fell rapidly with increasing N which indicates the decoupling of the molecule from the ^4He atoms. These results show: (i) the BOAR model is able to detect the hallmarks of microscopic superfluidity, (ii) that this phenomenon is quite insensitive to many of the details of the 3D Hamiltonian and, (iii) the repulsive part of the He-He PES is implicated in the decoupling of the molecule from the ^4He atoms because decoupling is evident even when the Aziz PES is replaced with a purely repulsive barrier.

Microscopic superfluidity was also studied in a ^4He -HCN complex. Once again the reduced dimensionality BOAR model was employed and the same three types of PES were used in the simulations. The results obtained were in agreement with those of the ^4He -CO study. The BOAR model was able to capture the characteristic “turn around” of the effective rotational constant, B_{eff} , of the HCN molecule with increasing numbers of ^4He atoms. Once again the repulsive He-He interactions are implicated in the decoupling of the molecule from the ^4He atoms since replacing the Aziz PES does not have any effect on the trend observed for the effective rotational constant.

Lastly, the effects of rotor size versus anisotropy on renormalization of the rotational constants of an ammonia molecule seeded into a ^4He droplet were studied. Simulations were done using the accurate rotational constants ($B_0 = 9.945$

cm^{-1} , $C_0 = 6.229 \text{ cm}^{-1}$) and using a “fudged” versions of the rotational constants ($B_{fudged} = 0.9945 \text{ cm}^{-1}$, $C_{fudged} = 0.6229 \text{ cm}^{-1}$) for the $|0011\rangle$ state where the rotational dynamics of note were that of the ^4He atoms. A reduction in the renormalization constants was observed for both. The simulations done with the fudged rotational constants experienced a slightly smaller reduction than those done using the accurate rotational constants. This may be attributed to the importance of molecular anisotropy versus the size of the rotational constants in molecules whose rotational constants fall in an intermediate regime. It is possible that in this intermediate regime of the fudged rotational constants of the NH_3 molecule the effects of the molecular anisotropy govern the extent of renormalization much more than the size of the bare gas rotational constant. The reduction in B_0 calculated using the accurate rotational constants for the ammonia molecule for the $|0011\rangle$ state, about 34% achieved for $N \sim 15\text{-}20$, was much higher than that found by Slipchenko and Vilesov [35], Suárez et al. [115], a 3% reduction of B_0 and even the controversial finding by Behrens et al. [33] of a reduction of $\sim 25\%$. This discrepancy might be due to the state used for the simulations, i.e., the fact that the calculations for the B_0 was based off of the excited state energies calculated for the $|0011\rangle$ state. The main conclusion of this study is that the “rule-of-thumb” theories that are used to predict the extent or the rate of renormalization for light or heavy rotors are not applicable to those rotors that fall in the intermediate regime. A new set of rules needs to be developed for these rotors. Also, while the results on the rate of renormalization were in agreement with previous studies [111, 113, 115], the data obtained for the renormalization of the rotational constants are far off from the expected values. Thus further investigations needs to be done to determine the root cause of this discrepancy.

REFERENCES

- [1] S. Goyal, D. L. Schutt, G. Scoles, *Phys. Rev. Lett.* 69, 933 (1992).
- [2] S. Grebenev, J. Toennies, A. Vilesov, *Science* 279, 2083 (1998).
- [3] F. Stienkemeier, K. K. Lehmann, *J. Phys. B: At. Mol. Opt. Phys.* 39, R127 (2006).
- [4] C. Callegari, K. Lehmann, R. S. ad G. Scoles, *J. Chem. Phys.* 115, 10090 (2001).
- [5] C. Callegari, W. Jäger, F. Stienkemeier, in K. D. Sattler (ed.), *Handbook of Nanophysics: Nanoparticles and Quantum Dots*, chap. 4, pp. 4.1–4.28. CRC Press. Taylor and Francis Group, Boca Raton, Fl (2011).
- [6] J. Northby, *J. Chem. Phys.* 115, 10065 (2001).
- [7] J. P. Toennies, A. P. Vilesov, *Angew. Chem. Int. Ed.* 43, 2622 (2004).
- [8] K. B. Whaley, *Int. Revs. Phys. Chem.* 13, 41 (1994).
- [9] Y. Kwon, P. Huang, M. Patel, D. Blume, K. Whaley, *J. Chem. Phys.* 113, 6469 (2000).
- [10] M. N. Slipchenko, S. Kuma, T. Momose, A. F. Vilesov, *Rev. Sci. Instr.* 73, 3600 (2002).
- [11] G. N. Makarov, *Phys. Usp.* 47, 217 (2004).
- [12] M. Barranco, et al., *J. Low Temp. Phys.* 142, 1 (2006).
- [13] M. Y. Choi, et al., *Int. Rev. Phys. Chem.* 25, 15 (2006).
- [14] J. Küpper, J. M. Merritt, *Int. Rev. Phys. Chem.* 26, 249 (2007).
- [15] J. K. Gregory, D. C. Clary, *J. Chem. Phys.* 102, 7817 (1995).

- [16] J. K. Gregory, D. C. Clary, *J. Chem. Phys.* 103, 8924 (1995).
- [17] J. M. Sorenson, J. K. Gregory, D. C. Clary, *Chem. Phys. Lett.* 263, 680 (1996).
- [18] V. Buch, *J. Chem. Phys.* 97, 726 (1992).
- [19] M. Mella, D. C. Clary, *J. Chem. Phys.* 119, 10048 (2003).
- [20] K. Nauta, R. E. Miller, *J. Chem. Phys.* 113, 10158 (2000).
- [21] L. A. Surin, et al., *Phys. Rev. Lett.* 101, 233401 (2008).
- [22] X.-G. Wang, T. Carrington, J. Tang, A. R. W. McKellar, *J. Chem. Phys.* 123, 034301 (2005).
- [23] J. Tang, A. R. W. McKellar, X.-G. Wang, T. Carrington, *Can. J. Phys.* 87, 417 (2009).
- [24] X.-G. Wang, T. Carrington, A. R. W. McKellar, *J. Phys. Chem. A* 113, 13331 (2009).
- [25] P. L. Raston, et al., *Phys. Chem. Chem. Phys.* 12, 8260 (2010).
- [26] X.-G. Wang, T. Carrington, *Can. J. Chem.* 88, 779 (2010).
- [27] H. Li, Y. Liu, W. Jäger, R. J. LeRoy, P.-N. Roy, *Can. J. Chem.* 88, 1146 (2010).
- [28] M. N. Slipchenko, K. E. Kuyanov, B. G. Sartakov, A. F. Vilesov, *J. Chem. Phys.* 124, 241101 (2006).
- [29] J. Xu, K. D. Jordan, *J. Phys. Chem. A* 114, 1364 (2009).
- [30] S. Mueller, S. Krapf, T. Koslowski, M. Mudrich, F. Stienkemeier, *Phys. Rev. Lett.* 102, 183401 (2009).

- [31] K. Kuyanov-Prozument, M. Y. Choi, A. F. Vilesov, *J. Chem. Phys.* 132, 014304 (2010).
- [32] F. Zappa, et al., *JACS* 130, 5573 (2008).
- [33] M. Behrens, et al., *J. Chem. Phys.* 109, 5914 (1998).
- [34] M. Behrens, U. Buck, R. Fröchtenicht, M. Hartmann, M. Havenith, *J. Chem. Phys.* 107, 7179 (1994).
- [35] M. N. Slipchenko, A. F. Vilesov, *Chem. Phys. Lett.* 412, 176 (2005).
- [36] M. N. Slipchenko, B. G. Sartakov, A. F. Vilesov, *J. Chem. Phys.* 128, 134509 (2008).
- [37] S. Kuma, M. N. Slipchenko, T. Momose, A. F. Vilesov, *Chem. Phys. Lett.* 439, 265 (2007).
- [38] D. Skvortsov, M. Y. Choi, A. F. Vilesov, *J. Phys. Chem. A* 111, 12711 (2007).
- [39] D. Skvortsov, S. J. Lee, M. Y. Choi, A. F. Vilesov, *J. Phys. Chem. A* 113, 7360 (2009).
- [40] A. M. Morrison, S. D. Flynn, T. Liang, G. E. Douberly, *J. Phys. Chem. A* 114, 8090 (2010).
- [41] S. D. Flynn, et al., *J. Phys. Chem. Letts.* 1, 2233 (2010).
- [42] F. Ferreira da Silva, et al., *Phys. Chem. Chem. Phys.* 11, 11631 (2009).
- [43] K. Leino, A. Viel, R. E. Zillich, *J. Chem. Phys.* 129, 184308 (2008).
- [44] K. Nauta, R. E. Miller, *Science* 283, 1895 (1999).
- [45] E. Lugovoj, J. P. Toennies, A. Vilesov, *J. Chem. Phys.* 112, 8217 (2000).

- [46] A. Braun, M. Drabbels, J. Chem. Phys. 127, 114304 (2007).
- [47] A. Braun, M. Drabbels, J. Chem. Phys. 127, 114305 (2007).
- [48] A. Braun, M. Drabbels, J. Chem. Phys. 127, 114303 (2007).
- [49] M. Hartmann, A. Lindinger, J. P. Toennies, A. F. Vilesov, J. Phys. Chem. A 105, 6369 (2001).
- [50] M. Wewer, F. Stienkemeier, Phys. Chem. Chem. Phys. 7, 1171 (2005).
- [51] N. B. Brauer, S. Smolarek, X. Zhang, W. J. Buma, M. Drabbels, J. Phys. Chem. Letts. 2, 1563 (2011).
- [52] V. Mozhayskiy, M. N. Slipchenko, V. K. Adamchuk, A. F. Vilesov, J. Chem. Phys. 127, 094701 (2007).
- [53] S. Smolarek, N. B. Brauer, W. J. Buma, M. Drabbels, JACS 132, 14086 (2010).
- [54] M. Hartmann, R. Miller, J. Toennies, A. Vilesov, Phys. Rev. Lett. 75, 1566 (1995).
- [55] P. L. Raston, W. Jäger, H. Li, R. Le Roy, P.-N. Roy, Phys. Rev. Lett. 108, 253402 (2012).
- [56] L. D. Landau, J. Phys. USSR 5(71-90) (1941).
- [57] A. J. Leggett, Acta. Fenn. 8, 125 (1973).
- [58] C. Callegari, et al., Phys. Rev. Lett. 83, 5058 (1999).
- [59] C. Callegari, K. K. Lehmann, J. Chem. Phys. 117, 1595 (2002).
- [60] M. Boninsegni, N. Prokof'ev, B. Svistunov, Phys. Rev. Lett. 96, 070601 (2006).

- [61] L. A. Surin, *JETP Letters* 97(1), 57 (2013).
- [62] J. Toennies, *Mol. Phys.* 111(12-13), 1879 (2013).
- [63] W. M. C. Foulkes, L. Mitas, R. J. Needs, G. Rajagopal, *Rev. Mod. Phys.* 73, 33 (2001).
- [64] R. J. Needs, M. D. Towler, N. D. Drummond, P. L. Ríos, *J. Phys. Condensed Matter* 22, 1 (2010).
- [65] A. B. McCoy, *Int. Revs. Phys. Chem.* 25, 77 (2006).
- [66] J. B. Anderson, *J. Chem. Phys.* 63, 1499 (1975).
- [67] J. B. Anderson, *J. Chem. Phys.* 65, 4121 (1976).
- [68] D. M. Ceperley, B. J. Alder, *J. Chem. Phys.* 81, 5833 (1984).
- [69] D. M. Ceperley, B. Alder, *Science* 231, 555 (1986).
- [70] B. Hammond, J. W.A Lester, P. J. Reynolds, World Scientific (1994).
- [71] D. M. Ceperley, *Rev. Miner. Geochem.* 71, 129 (2010).
- [72] A. Viel, M. V. Patel, P. Niyaz, K. B. Whaley, *Comp. Phys. Commun.* 145, 24 (2002).
- [73] D. M. Ceperley, *Rev. Mod. Phys.* 67, 279 (1995).
- [74] R. E. Zillich, F. Paesani, Y. Know, K. B. Whaley, *J. Chem. Phys.* 123, 114301 (2005).
- [75] P. Huang, A. Viel, K. B. Whaley, in S. M. R. W. A. Lester, Jr., S. Tanaka (eds.), *Recent Advances in Quantum Monte Carlo Methods*, pp. 111–127. World Scientific, Singapore (2002).
- [76] A. Viel, K. B. Whaley, *J. Chem. Phys.* 115, 10186 (2001).

- [77] S. Baroni, S. Maroni, *Phys. Rev. Lett.* 82, 4745 (1999).
- [78] P. Cazzato, S. Paolini, S. Moroni, S. Baroni, *J. Chem. Phys.* 120, 9071 (2004).
- [79] J. Tang, A. R. W. McKellar, *J. Chem. Phys.* 119, 754 (2003).
- [80] A. Lüchow, R. Petz, A. Schwarz, *Zeit. für Phys. Chemie* 224, 343 (2010).
- [81] F. A. Reboredo, R. Q. Hood, P. R. C. Kent, *Phys. Rev. B* 79, 195117 (2009).
- [82] J. B. Anderson, *Phys. Rev. A* 35, 3550 (1987).
- [83] D. M. Ceperley, *J. Stat. Phys.* 63, 1237 (1991).
- [84] M. H. Kalos, *J. Stat. Phys.* 63, 1269 (1991).
- [85] M. Bajdich, L. Mitas, G. Drobný, L. K. Wagner, *Phys. Rev. B* 72, 075131 (2005).
- [86] L. Mitas, *Phys. Rev. Lett.* 96, 240402 (2006).
- [87] P. J. Reynolds, D. M. Ceperley, B. J. Alder, W. A. Lester, *J. Chem. Phys.* 77, 5593 (1982).
- [88] P. Sandler, V. Buch, J. Sadlej, *J. Chem. Phys.* 105, 10387 (1996).
- [89] M. W. Severson, V. Buch, *J. Chem. Phys.* 111, 10866 (1999).
- [90] A. Lüchow, T. C. Scott, *J. Phys. B: At. Mol. Opt. Phys.* 40, 851 (2007).
- [91] M. H. Kalos, D. Levesque, L. Verlet, *Phys. Rev. A* 9, 2178 (1974).
- [92] C. J. Umrigar, M. P. Nightingale, K. J. Runge, *J. Chem. Phys.* 99, 2865 (1993).
- [93] I. Kosztin, B. Faber, K. Schulten, *Am. J. Phys.* 64(5), 633 (1995).

- [94] D. Bressanini, P. J. Reynolds, *Phys. Rev. Lett.* 95, 110201 (2005).
- [95] E. LeDell, Prabhat, D. Zubarev, B. Austin, J. W.A. Lester, *J. Math Chem.* 50, 2043 (2012).
- [96] L. Hansen, E. A. Lee, K. Hestir, L. T. Williams, D. Farrelly, *Combinatorial Chemistry & High Throughput Screening* 12, 514 (2009).
- [97] T. Scott, A. Lüchow, D. Bressanini, J. Morgan, *Phys. Rev. A* 75, 060101 (2007).
- [98] R. Haupt, S. Haupt, *Practical genetic algorithms*. John Wiley & Sons. Inc., 605 Third Avenue, New York, NY 10158 (1998).
- [99] J. Holland, *Adaptation in Natural and Artificial Systems*. Holland (1975).
- [100] J. A. Ramilowski, D. Farrelly, *Phys. Chem. Chem. Phys.* 14, 8123 (2012).
- [101] J. A. Ramilowski, D. Farrelly, *Phys. Chem. Chem. Phys.* 12, 12450 (2010).
- [102] A. Lüchow, R. Petz, T. C. Scott, *J. Chem. Phys.* 126, 144110 (2007).
- [103] S. Dempster, O. Sukhorukov, Q.-Y. Lei, W. Jäger, *J. Chem. Phys.* 137, 174303 (2012).
- [104] M. Girardeau, *J. Math. Phys.* 1, 516 (1960).
- [105] M. Girardeau, E. Wright, J. Triscari, *Phys. Rev. A* 63, 033601 (2001).
- [106] T. Kinoshita, T. Wegner, D. Weiss, *Science* 305(5687), 1125 (2004).
- [107] K. K. Lehmann, *J. Chem. Phys.* 114, 4643 (2001).
- [108] R. Miller, *Faraday Disc.* 118, 1 (2001).
- [109] F. Paesani, K. B. Whaley, *J. Chem. Phys.* 121, 5293 (2004).

- [110] M. Patel, A. Viel, F. Paesani, P. Huang, K. B. Whaley, *J. Chem. Phys.* 118, 5011 (2003).
- [111] J. A. Ramilowski, A. A. Mikosz, D. Farrelly, J. L. C. Fajin, B. Fernández, *J. Phys. Chem.* 111, 12275 (2007).
- [112] E. A. Lee, D. Farrelly, K. B. Whaley, *Phys. Rev. Lett.* 83, 3812 (1999).
- [113] A. A. Mikosz, J. A. Ramilowski, D. Farrelly, *J. Chem. Phys.* 125, 014312 (2006).
- [114] N. Markovskiy, C. Mak, *J. Phys. Chem.* 113, 3812 (2009).
- [115] A. Gamboa Suárez, J. A. Ramilowski, R. M. Benito, D. Farrelly, *Chem. Phys. Lett.* 502, 14 (2011).
- [116] A. Viel, K. Whaley, R. Wheatley, *J. Chem. Phys.* 127, 194303 (2007).
- [117] R. Bartlett, M. Musial, *Rev. Mod. Phys.* 79, 291 (2007).
- [118] D. M. Benoit, D. C. Clary, *J. Chem. Phys.* 113, 5193 (2000).
- [119] B. M. Austin, D. Y. Zubarev, W. A. Lester, *Chem. Rev.* 112, 263 (2012).
- [120] A. Petit, A. McCoy, *J. Phys. Chem. A* 117, 7009 (2013).
- [121] A. Wairegi, A. Gamboa, A. D. Burbanks, E. A. Lee, D. Farrelly, *Phys. Rev. Lett.* 112, 143401 (2014).
- [122] D. Goldberg, K. Sastry, *Genetic algorithms: The design of innovation.* Springer (2010).
- [123] G. Garai, B. B. Chaudhuri, *Pattern Recognition* 40, 212 (2007).
- [124] B. Hartke, *Wiley Interdiscip. Rev. Comput. Mol. Sci.* 1, 879 (2011).
- [125] '<http://www.hao.ucar.edu/moedling/pikaia/pikaia.php>' (1999).

- [126] C. J. Umigar, M. P. Nightingale, K. J. Runge, *J. Chem. Phys.* 99, 2865 (1993).
- [127] G. G. de Polavieja, F. Borondo, *Int. J. Quantum. Chem.* 51, 555 (1994).
- [128] H. Aiba, T. Suzuki, *Phys. Rev. E* 72, 066214 (2005).
- [129] M. Rezaei, N. Moazzen-Ahmadi, A. McKellar, B. Fernández, D. Farrelly, *Mol. Phys.* 110, 2743 (2012).
- [130] B. Fernández, C. Henriksen, D. Farrelly, *Mol. Phys.* 111, 1173 (2013).
- [131] A. Y. Cherny, J.-S. Caux, J. Brand, *Front. Phys.* 7, 54 (2012).
- [132] A. Sykes, M. Davis, D. Roberts, *Phys. Rev. Lett.* 103, 085302 (2009).
- [133] C. Schenke, A. Minguzzi, F. W. J. Hekking, *Phys. Rev. A* 85, 053627 (2012).
- [134] C. E. Chuaqui, R. J. LeRoy, A. R. W. McKellar, *J. Chem. Phys.* 101, 39 (1994).
- [135] R. A. Aziz, F. R. W. McCourt, C. C. K. Wong, *Mol. Phys.* 61(6), 1487 (1987).
- [136] '<http://link.aps.org/supplemental/10.1103/physrevlett.112.143401>'.
- [137] L. F. Roncaratti, V. Aquilanti, *Int. J. Quantum. Chem.* 110, 716 (2010).
- [138] S. M. Parker, M. A. Ratner, T. Seideman, *J. Chem. Phys.* 135, 224301 (2011).
- [139] J. Ross, H. Capel, *Physica (Amsterdam)* 287A, 217 (2000).
- [140] D. Kosloff, R. Kosloff, *J. Comput. Phys.* 52, 35 (1983).
- [141] R. Chacon, F. Borondo, D. Farrelly, *Europhys. Lett.* 86, 30004 (2009).
- [142] M. Grifoni, P. Hanggi, *Phys. Rep.* 304, 134316 (1998).

- [143] B. G. Sartakov, J. P. Toennies, A. F. Vilesov, *J. Chem. Phys.* 136, 134316 (2012).
- [144] M. Girardeau, A. Minguzzi, *Phys. Rev. Lett* 96, 080404 (2006).
- [145] K. Sakmann, A. Streltsov, O. Alon, L. Cederbaum, *Phys. Rev. A* 72, 033613 (2005).
- [146] K. K. Lehmann, G. Scoles, *Science* 279, 2065 (1998).
- [147] K. Szalewicz, *Int. Rev. Phys. Chem.* 27, 273 (2008).
- [148] A. C. Moskun, E. J. Askat, S. E. Bradforth, G. Tao, R. M. Stratt, *Science* 311, 1907 (2006).
- [149] J. Tang, Y. J. Xu, A. R. W. McKellar, W. Jäger, *Science* 297, 2030 (2002).
- [150] K. Nauta, D. T. Moore, P. L. Stiles, R. E. Miller, *Science* 292, 481 (2001).
- [151] Y. Xu, W. Jaeger, J. Tang, A. R. W. McKellar, *Phys. Rev. Lett.* 91, 163401 (2003).
- [152] A. Conjusteau, C. Callegari, I. Reinhard, K. K. Lehmann, G. Scoles, *J. Chem. Phys.* 113, 4840 (2000).
- [153] G. Scoles, K. K. Lehmann, *Science* 287, 2429 (2000).
- [154] D. Goldberg, K. Deb, B. Korb, *Complex systems* 3, 493 (1989).
- [155] S. L. Holmgren, M. Waldman, W. Klemperer, *J. Chem. Phys.* 67, 4414 (1977).
- [156] A. Wairegi, D. Farrelly, *Chem. Phys. Lett.* 619, 71 (2015).
- [157] J. Wilks, D. S. Betts, *An Introduction to Liquid Helium*. Clarendon Press, Oxford, U.K. (1987).

- [158] D. R. Tilley, J. Tilley, Superfluidity and Superconductivity. Institute of Physics, Bristol, U.K. (1990).
- [159] S. Paolini, S. Fantoni, S. Moroni, S. Baroni, J. Chem. Phys. 123, 114306 (2005).
- [160] R. E. Zillich, Y. Kwon, K. B. Whaley, Phys. Rev. Lett. 93, 250401 (2004).
- [161] S. Moroni, M. Botti, S. DePalo, A. R. W. McKellar, J. Chem. Phys. 122, 094314 (2005).
- [162] T. Škrbić, S. Moroni, S. Baroni, J. Phys. Chem. A 111, 7640 (2007).
- [163] R. von Haeften, I. Simanovski, M. Havenith, R. Zillich, K. Whaley, Phys. Rev. B 73, 054502 (2006).
- [164] M. P. Hodges, R. J. Wheatley, J. Phys. Chem. 114, 8836 (2001).
- [165] R. Aziz, M. Slaman, J. Chem. Phys. 94, 8047 (1991).
- [166] J. Hutson, A. Thornley, J. Chem. Phys. 100, 2505 (1994).
- [167] R. N. Zare, Angular Momentum: Understanding Spatial Aspects in Chemistry and Physics. Wiley, New York (1988).
- [168] D. Brink, G. Satchler, Angular momentum. Clarendon Press, Oxford, U.K. (2002).
- [169] J. Hutson, J Chem. Phys. 92, 157 (1990).
- [170] J. M. Hutson, Adv. Mol. Vibr. Coll. Dyn. 1A, 1 (1991).
- [171] J. M. Hutson, 'BOUND, Version 5: A program for calculating bound-state energies for weakly bound molecular complexes, distributed *via* Collaborative Computing Project No. 6, of the Science and Engineering Research Council, on Molecular Quantum Dynamics, UK' (1993).

[172] A. Petit, A. B. McCoy, *J. Chem. Phys. A* 113, 12706 (2009).

[173] E. Vehmanen, et al., *J. Phys. Chem. A* 115, 7077 (2011).

APPENDICES

**JOHN WILEY AND SONS LICENSE
TERMS AND CONDITIONS**

Apr 18, 2016

This Agreement between Angeline R Wairegi ("You") and John Wiley and Sons ("John Wiley and Sons") consists of your license details and the terms and conditions provided by John Wiley and Sons and Copyright Clearance Center.

License Number	3824970360673
License date	Mar 09, 2016
Licensed Content Publisher	John Wiley and Sons
Licensed Content Publication	Wiley eBooks
Licensed Content Title	The Binary Genetic Algorithm
Licensed Content Author	Randy L. Haupt,Sue Ellen Haupt
Licensed Content Date	Jul 15, 2004
Pages	24
Type of use	Dissertation/Thesis
Requestor type	University/Academic
Format	Print and electronic
Portion	Figure/table
Number of figures/tables	1
Original Wiley figure/table number(s)	Figure 2.2
Will you be translating?	No
Title of your thesis / dissertation	Computational studies of microscopic superfluidity
Expected completion date	Mar 2016
Expected size (number of pages)	125
Requestor Location	Angeline R Wairegi 444 South 100 West Apt. 3 LOGAN, UT 84321 United States Attn: Angeline R Wairegi
Billing Type	Invoice
Billing Address	Angeline R Wairegi 444 South 100 West Apt. 3 LOGAN, UT 84321 United States Attn: Angeline R Wairegi

Total 0.00 USD

[Terms and Conditions](#)

TERMS AND CONDITIONS

This copyrighted material is owned by or exclusively licensed to John Wiley & Sons, Inc. or one of its group companies (each a "Wiley Company") or handled on behalf of a society with which a Wiley Company has exclusive publishing rights in relation to a particular work (collectively "WILEY"). By clicking "accept" in connection with completing this licensing transaction, you agree that the following terms and conditions apply to this transaction (along with the billing and payment terms and conditions established by the Copyright Clearance Center Inc., ("CCC's Billing and Payment terms and conditions"), at the time that you opened your RightsLink account (these are available at any time at <http://myaccount.copyright.com>).

Terms and Conditions

- The materials you have requested permission to reproduce or reuse (the "Wiley Materials") are protected by copyright.
- You are hereby granted a personal, non-exclusive, non-sub licensable (on a stand-alone basis), non-transferable, worldwide, limited license to reproduce the Wiley Materials for the purpose specified in the licensing process. This license, **and any CONTENT (PDF or image file) purchased as part of your order**, is for a one-time use only and limited to any maximum distribution number specified in the license. The first instance of republication or reuse granted by this license must be completed within two years of the date of the grant of this license (although copies prepared before the end date may be distributed thereafter). The Wiley Materials shall not be used in any other manner or for any other purpose, beyond what is granted in the license. Permission is granted subject to an appropriate acknowledgement given to the author, title of the material/book/journal and the publisher. You shall also duplicate the copyright notice that appears in the Wiley publication in your use of the Wiley Material. Permission is also granted on the understanding that nowhere in the text is a previously published source acknowledged for all or part of this Wiley Material. Any third party content is expressly excluded from this permission.
- With respect to the Wiley Materials, all rights are reserved. Except as expressly granted by the terms of the license, no part of the Wiley Materials may be copied, modified, adapted (except for minor reformatting required by the new Publication), translated, reproduced, transferred or distributed, in any form or by any means, and no derivative works may be made based on the Wiley Materials without the prior permission of the respective copyright owner. **For STM Signatory Publishers clearing permission under the terms of the [STM Permissions Guidelines](#) only, the terms of the license are extended to include subsequent editions and for editions in other languages, provided such editions are for the work as a whole in situ and does not involve the separate exploitation of the permitted figures or extracts**, You may not alter, remove or suppress in any manner any copyright, trademark or other notices displayed by the Wiley Materials. You may not license, rent, sell, loan, lease, pledge, offer as security, transfer or assign the Wiley Materials on a stand-alone basis, or any of the rights granted to you hereunder to any other person.
- The Wiley Materials and all of the intellectual property rights therein shall at all times

remain the exclusive property of John Wiley & Sons Inc, the Wiley Companies, or their respective licensors, and your interest therein is only that of having possession of and the right to reproduce the Wiley Materials pursuant to Section 2 herein during the continuance of this Agreement. You agree that you own no right, title or interest in or to the Wiley Materials or any of the intellectual property rights therein. You shall have no rights hereunder other than the license as provided for above in Section 2. No right, license or interest to any trademark, trade name, service mark or other branding ("Marks") of WILEY or its licensors is granted hereunder, and you agree that you shall not assert any such right, license or interest with respect thereto

- NEITHER WILEY NOR ITS LICENSORS MAKES ANY WARRANTY OR REPRESENTATION OF ANY KIND TO YOU OR ANY THIRD PARTY, EXPRESS, IMPLIED OR STATUTORY, WITH RESPECT TO THE MATERIALS OR THE ACCURACY OF ANY INFORMATION CONTAINED IN THE MATERIALS, INCLUDING, WITHOUT LIMITATION, ANY IMPLIED WARRANTY OF MERCHANTABILITY, ACCURACY, SATISFACTORY QUALITY, FITNESS FOR A PARTICULAR PURPOSE, USABILITY, INTEGRATION OR NON-INFRINGEMENT AND ALL SUCH WARRANTIES ARE HEREBY EXCLUDED BY WILEY AND ITS LICENSORS AND WAIVED BY YOU.
- WILEY shall have the right to terminate this Agreement immediately upon breach of this Agreement by you.
- You shall indemnify, defend and hold harmless WILEY, its Licensors and their respective directors, officers, agents and employees, from and against any actual or threatened claims, demands, causes of action or proceedings arising from any breach of this Agreement by you.
- IN NO EVENT SHALL WILEY OR ITS LICENSORS BE LIABLE TO YOU OR ANY OTHER PARTY OR ANY OTHER PERSON OR ENTITY FOR ANY SPECIAL, CONSEQUENTIAL, INCIDENTAL, INDIRECT, EXEMPLARY OR PUNITIVE DAMAGES, HOWEVER CAUSED, ARISING OUT OF OR IN CONNECTION WITH THE DOWNLOADING, PROVISIONING, VIEWING OR USE OF THE MATERIALS REGARDLESS OF THE FORM OF ACTION, WHETHER FOR BREACH OF CONTRACT, BREACH OF WARRANTY, TORT, NEGLIGENCE, INFRINGEMENT OR OTHERWISE (INCLUDING, WITHOUT LIMITATION, DAMAGES BASED ON LOSS OF PROFITS, DATA, FILES, USE, BUSINESS OPPORTUNITY OR CLAIMS OF THIRD PARTIES), AND WHETHER OR NOT THE PARTY HAS BEEN ADVISED OF THE POSSIBILITY OF SUCH DAMAGES. THIS LIMITATION SHALL APPLY NOTWITHSTANDING ANY FAILURE OF ESSENTIAL PURPOSE OF ANY LIMITED REMEDY PROVIDED HEREIN.
- Should any provision of this Agreement be held by a court of competent jurisdiction to be illegal, invalid, or unenforceable, that provision shall be deemed amended to achieve as nearly as possible the same economic effect as the original provision, and the legality, validity and enforceability of the remaining provisions of this Agreement shall not be affected or impaired thereby.

- The failure of either party to enforce any term or condition of this Agreement shall not constitute a waiver of either party's right to enforce each and every term and condition of this Agreement. No breach under this agreement shall be deemed waived or excused by either party unless such waiver or consent is in writing signed by the party granting such waiver or consent. The waiver by or consent of a party to a breach of any provision of this Agreement shall not operate or be construed as a waiver of or consent to any other or subsequent breach by such other party.
- This Agreement may not be assigned (including by operation of law or otherwise) by you without WILEY's prior written consent.
- Any fee required for this permission shall be non-refundable after thirty (30) days from receipt by the CCC.
- These terms and conditions together with CCC's Billing and Payment terms and conditions (which are incorporated herein) form the entire agreement between you and WILEY concerning this licensing transaction and (in the absence of fraud) supersedes all prior agreements and representations of the parties, oral or written. This Agreement may not be amended except in writing signed by both parties. This Agreement shall be binding upon and inure to the benefit of the parties' successors, legal representatives, and authorized assigns.
- In the event of any conflict between your obligations established by these terms and conditions and those established by CCC's Billing and Payment terms and conditions, these terms and conditions shall prevail.
- WILEY expressly reserves all rights not specifically granted in the combination of (i) the license details provided by you and accepted in the course of this licensing transaction, (ii) these terms and conditions and (iii) CCC's Billing and Payment terms and conditions.
- This Agreement will be void if the Type of Use, Format, Circulation, or Requestor Type was misrepresented during the licensing process.
- This Agreement shall be governed by and construed in accordance with the laws of the State of New York, USA, without regards to such state's conflict of law rules. Any legal action, suit or proceeding arising out of or relating to these Terms and Conditions or the breach thereof shall be instituted in a court of competent jurisdiction in New York County in the State of New York in the United States of America and each party hereby consents and submits to the personal jurisdiction of such court, waives any objection to venue in such court and consents to service of process by registered or certified mail, return receipt requested, at the last known address of such party.

WILEY OPEN ACCESS TERMS AND CONDITIONS

Wiley Publishes Open Access Articles in fully Open Access Journals and in Subscription journals offering Online Open. Although most of the fully Open Access journals publish open access articles under the terms of the Creative Commons Attribution (CC BY) License only, the subscription journals and a few of the Open Access Journals offer a choice of Creative Commons Licenses. The license type is clearly identified on the article.

The Creative Commons Attribution License

The [Creative Commons Attribution License \(CC-BY\)](#) allows users to copy, distribute and transmit an article, adapt the article and make commercial use of the article. The CC-BY license permits commercial and non-

Creative Commons Attribution Non-Commercial License

The [Creative Commons Attribution Non-Commercial \(CC-BY-NC\)License](#) permits use, distribution and reproduction in any medium, provided the original work is properly cited and is not used for commercial purposes.(see below)

Creative Commons Attribution-Non-Commercial-NoDerivs License

The [Creative Commons Attribution Non-Commercial-NoDerivs License](#) (CC-BY-NC-ND) permits use, distribution and reproduction in any medium, provided the original work is properly cited, is not used for commercial purposes and no modifications or adaptations are made. (see below)

Use by commercial "for-profit" organizations

Use of Wiley Open Access articles for commercial, promotional, or marketing purposes requires further explicit permission from Wiley and will be subject to a fee.

Further details can be found on Wiley Online Library
<http://olabout.wiley.com/WileyCDA/Section/id-410895.html>

Other Terms and Conditions:

v1.10 Last updated September 2015

Questions? customercare@copyright.com or +1-855-239-3415 (toll free in the US) or +1-978-646-2777.

**AMERICAN PHYSICAL SOCIETY LICENSE
TERMS AND CONDITIONS**

Apr 18, 2016

This Agreement between Angeline R Wairegi ("You") and American Physical Society ("American Physical Society") consists of your license details and the terms and conditions provided by American Physical Society and Copyright Clearance Center.

License Number	3824980168709
License date	Mar 09, 2016
Licensed Content Publisher	American Physical Society
Licensed Content Publication	Physical Review Letters
Licensed Content Title	Microscopic Superfluidity in $^4\mathrm{He}$ Clusters Stirred by a Rotating Impurity Molecule
Licensed Content Author	Angeline Wairegi et al.
Licensed Content Date	Apr 11, 2014
Licensed Content Volume Number	112
Type of Use	Thesis/Dissertation
Requestor type	Student
Format	Print, Electronic
Portion	chapter/article
Rights for	Main product
Duration of use	Life of Current Edition
Creation of copies for the disabled	no
With minor editing privileges	no
For distribution to	United States
In the following language(s)	Original language of publication
With incidental promotional use	no
The lifetime unit quantity of new product	0 to 499
The requesting person/organization is:	Angeline Wairegi
Order reference number	None
Title of your thesis / dissertation	Computational studies of microscopic superfluidity
Expected completion date	Mar 2016
Expected size (number of pages)	125
Requestor Location	Angeline R Wairegi

	444 South 100 West Apt. 3
	LOGAN, UT 84321 United States Attn: Angeline R Wairegi
Billing Type	Invoice
Billing Address	Angeline R Wairegi 444 South 100 West Apt. 3
	LOGAN, UT 84321 United States Attn: Angeline R Wairegi
Total	0.00 USD
Terms and Conditions	

Terms and Conditions

The American Physical Society (APS) is pleased to grant the Requestor of this license a non-exclusive, non-transferable permission, limited to [**print** and/or **electronic** format, depending on what they chose], provided all criteria outlined below are followed.

1. For electronic format permissions, Requestor agrees to provide a hyperlink from the reprinted APS material using the source material's DOI on the web page where the work appears. The hyperlink should use the standard DOI resolution URL, <http://dx.doi.org/{DOI}>. The hyperlink may be embedded in the copyright credit line.
2. For print format permissions, Requestor agrees to print the required copyright credit line on the first page where the material appears: "Reprinted (abstract/excerpt/figure) with permission from [(FULL REFERENCE CITATION) as follows: Author's Names, APS Journal Title, Volume Number, Page Number and Year of Publication.] Copyright (YEAR) by the American Physical Society."
3. Permission granted in this license is for a one-time use and does not include permission for any future editions, updates, databases, formats or other matters. Permission must be sought for any additional use.
4. Use of the material does not and must not imply any endorsement by APS.
5. Under no circumstance does APS purport or intend to grant permission to reuse materials to which it does not hold copyright. It is the requestors sole responsibility to ensure the licensed material is original to APS and does not contain the copyright of another entity, and that the copyright notice of the figure, photograph, cover or table does not indicate that it was reprinted by APS, with permission from another source.
6. The permission granted herein is personal to the Requestor for the use specified and is not transferable or assignable without express written permission of APS. This license may not be amended except in writing by APS.
7. You may not alter, edit or modify the material in any manner.
8. You may translate the materials only when translation rights have been granted.
9. You may not use the material for promotional, sales, advertising or marketing purposes.
10. The foregoing license shall not take effect unless and until APS or its agent, Copyright Clearance Center (CCC), receives payment in full in accordance with CCC Billing and Payment Terms and Conditions, which are incorporated herein by reference.
11. Should the terms of this license be violated at any time, APS or CCC may revoke the license with no refund to you and seek relief to the fullest extent of the laws of the USA. Official written notice will be made using the contact information provided with the

permission request. Failure to receive such notice will not nullify revocation of the permission.

12. APS reserves all rights not specifically granted herein.

13. This document, including the CCC Billing and Payment Terms and Conditions, shall be the entire agreement between the parties relating to the subject matter hereof.

Other Terms and Conditions

Questions? customer@copyright.com or +1-855-239-3415 (toll free in the US) or +1-978-646-2777.

**ELSEVIER LICENSE
TERMS AND CONDITIONS**

Apr 18, 2016

This is a License Agreement between Angeline R Wairegi ("You") and Elsevier ("Elsevier") provided by Copyright Clearance Center ("CCC"). The license consists of your order details, the terms and conditions provided by Elsevier, and the payment terms and conditions.

All payments must be made in full to CCC. For payment instructions, please see information listed at the bottom of this form.

Supplier	Elsevier Limited The Boulevard, Langford Lane Kidlington, Oxford, OX5 1GB, UK
Registered Company Number	1982084
Customer name	Angeline R Wairegi
Customer address	444 South 100 West LOGAN, UT 84321
License number	3825000746939
License date	Mar 09, 2016
Licensed content publisher	Elsevier
Licensed content publication	Chemical Physics Letters
Licensed content title	On the fly nodal searches in importance sampled fixed-node diffusion Monte Carlo using a parallel, fine-grained, genetic algorithm
Licensed content author	Angeline Wairegi, David Farrelly
Licensed content date	5 January 2015
Licensed content volume number	619
Licensed content issue number	n/a
Number of pages	6
Start Page	71
End Page	76
Type of Use	reuse in a thesis/dissertation
Intended publisher of new work	other
Portion	full article
Format	both print and electronic
Are you the author of this Elsevier article?	Yes
Will you be translating?	No

Title of your thesis/dissertation	Computational studies of microscopic superfluidity
Expected completion date	Mar 2016
Estimated size (number of pages)	125
Elsevier VAT number	GB 494 6272 12
Permissions price	0.00 USD
VAT/Local Sales Tax	0.00 USD / 0.00 GBP
Total	0.00 USD
Terms and Conditions	

INTRODUCTION

1. The publisher for this copyrighted material is Elsevier. By clicking "accept" in connection with completing this licensing transaction, you agree that the following terms and conditions apply to this transaction (along with the Billing and Payment terms and conditions established by Copyright Clearance Center, Inc. ("CCC"), at the time that you opened your Rightslink account and that are available at any time at <http://myaccount.copyright.com>).

GENERAL TERMS

2. Elsevier hereby grants you permission to reproduce the aforementioned material subject to the terms and conditions indicated.
3. Acknowledgement: If any part of the material to be used (for example, figures) has appeared in our publication with credit or acknowledgement to another source, permission must also be sought from that source. If such permission is not obtained then that material may not be included in your publication/copies. Suitable acknowledgement to the source must be made, either as a footnote or in a reference list at the end of your publication, as follows:
"Reprinted from Publication title, Vol /edition number, Author(s), Title of article / title of chapter, Pages No., Copyright (Year), with permission from Elsevier [OR APPLICABLE SOCIETY COPYRIGHT OWNER]." Also Lancet special credit - "Reprinted from The Lancet, Vol. number, Author(s), Title of article, Pages No., Copyright (Year), with permission from Elsevier."
4. Reproduction of this material is confined to the purpose and/or media for which permission is hereby given.
5. Altering/Modifying Material: Not Permitted. However figures and illustrations may be altered/adapted minimally to serve your work. Any other abbreviations, additions, deletions and/or any other alterations shall be made only with prior written authorization of Elsevier Ltd. (Please contact Elsevier at permissions@elsevier.com)
6. If the permission fee for the requested use of our material is waived in this instance, please be advised that your future requests for Elsevier materials may attract a fee.
7. Reservation of Rights: Publisher reserves all rights not specifically granted in the combination of (i) the license details provided by you and accepted in the course of this licensing transaction, (ii) these terms and conditions and (iii) CCC's Billing and Payment terms and conditions.
8. License Contingent Upon Payment: While you may exercise the rights licensed immediately upon issuance of the license at the end of the licensing process for the transaction, provided that you have disclosed complete and accurate details of your proposed use, no license is finally effective unless and until full payment is received from you (either by publisher or by CCC) as provided in CCC's Billing and Payment terms and conditions. If

full payment is not received on a timely basis, then any license preliminarily granted shall be deemed automatically revoked and shall be void as if never granted. Further, in the event that you breach any of these terms and conditions or any of CCC's Billing and Payment terms and conditions, the license is automatically revoked and shall be void as if never granted. Use of materials as described in a revoked license, as well as any use of the materials beyond the scope of an unrevoked license, may constitute copyright infringement and publisher reserves the right to take any and all action to protect its copyright in the materials.

9. **Warranties:** Publisher makes no representations or warranties with respect to the licensed material.

10. **Indemnity:** You hereby indemnify and agree to hold harmless publisher and CCC, and their respective officers, directors, employees and agents, from and against any and all claims arising out of your use of the licensed material other than as specifically authorized pursuant to this license.

11. **No Transfer of License:** This license is personal to you and may not be sublicensed, assigned, or transferred by you to any other person without publisher's written permission.

12. **No Amendment Except in Writing:** This license may not be amended except in a writing signed by both parties (or, in the case of publisher, by CCC on publisher's behalf).

13. **Objection to Contrary Terms:** Publisher hereby objects to any terms contained in any purchase order, acknowledgment, check endorsement or other writing prepared by you, which terms are inconsistent with these terms and conditions or CCC's Billing and Payment terms and conditions. These terms and conditions, together with CCC's Billing and Payment terms and conditions (which are incorporated herein), comprise the entire agreement between you and publisher (and CCC) concerning this licensing transaction. In the event of any conflict between your obligations established by these terms and conditions and those established by CCC's Billing and Payment terms and conditions, these terms and conditions shall control.

14. **Revocation:** Elsevier or Copyright Clearance Center may deny the permissions described in this License at their sole discretion, for any reason or no reason, with a full refund payable to you. Notice of such denial will be made using the contact information provided by you. Failure to receive such notice will not alter or invalidate the denial. In no event will Elsevier or Copyright Clearance Center be responsible or liable for any costs, expenses or damage incurred by you as a result of a denial of your permission request, other than a refund of the amount(s) paid by you to Elsevier and/or Copyright Clearance Center for denied permissions.

LIMITED LICENSE

The following terms and conditions apply only to specific license types:

15. **Translation:** This permission is granted for non-exclusive world **English** rights only unless your license was granted for translation rights. If you licensed translation rights you may only translate this content into the languages you requested. A professional translator must perform all translations and reproduce the content word for word preserving the integrity of the article.

16. **Posting licensed content on any Website:** The following terms and conditions apply as follows: Licensing material from an Elsevier journal: All content posted to the web site must maintain the copyright information line on the bottom of each image; A hyper-text must be included to the Homepage of the journal from which you are licensing at <http://www.sciencedirect.com/science/journal/xxxxx> or the Elsevier homepage for books at <http://www.elsevier.com>; Central Storage: This license does not include permission for a scanned version of the material to be stored in a central repository such as that provided by Heron/XanEdu.

Licensing material from an Elsevier book: A hyper-text link must be included to the Elsevier homepage at <http://www.elsevier.com> . All content posted to the web site must maintain the copyright information line on the bottom of each image.

Posting licensed content on Electronic reserve: In addition to the above the following clauses are applicable: The web site must be password-protected and made available only to bona fide students registered on a relevant course. This permission is granted for 1 year only. You may obtain a new license for future website posting.

17. **For journal authors:** the following clauses are applicable in addition to the above:

Preprints:

A preprint is an author's own write-up of research results and analysis, it has not been peer-reviewed, nor has it had any other value added to it by a publisher (such as formatting, copyright, technical enhancement etc.).

Authors can share their preprints anywhere at any time. Preprints should not be added to or enhanced in any way in order to appear more like, or to substitute for, the final versions of articles however authors can update their preprints on arXiv or RePEc with their Accepted Author Manuscript (see below).

If accepted for publication, we encourage authors to link from the preprint to their formal publication via its DOI. Millions of researchers have access to the formal publications on ScienceDirect, and so links will help users to find, access, cite and use the best available version. Please note that Cell Press, The Lancet and some society-owned have different preprint policies. Information on these policies is available on the journal homepage.

Accepted Author Manuscripts: An accepted author manuscript is the manuscript of an article that has been accepted for publication and which typically includes author-incorporated changes suggested during submission, peer review and editor-author communications.

Authors can share their accepted author manuscript:

- immediately
 - o via their non-commercial person homepage or blog
 - o by updating a preprint in arXiv or RePEc with the accepted manuscript
 - o via their research institute or institutional repository for internal institutional uses or as part of an invitation-only research collaboration work-group
 - o directly by providing copies to their students or to research collaborators for their personal use
 - o for private scholarly sharing as part of an invitation-only work group on commercial sites with which Elsevier has an agreement
- after the embargo period
 - o via non-commercial hosting platforms such as their institutional repository
 - o via commercial sites with which Elsevier has an agreement

In all cases accepted manuscripts should:

- link to the formal publication via its DOI
- bear a CC-BY-NC-ND license - this is easy to do
- if aggregated with other manuscripts, for example in a repository or other site, be shared in alignment with our hosting policy not be added to or enhanced in any way to appear more like, or to substitute for, the published journal article.

Published journal article (JPA): A published journal article (PJA) is the definitive final

record of published research that appears or will appear in the journal and embodies all value-adding publishing activities including peer review co-ordination, copy-editing, formatting, (if relevant) pagination and online enrichment. Policies for sharing publishing journal articles differ for subscription and gold open access articles:

Subscription Articles: If you are an author, please share a link to your article rather than the full-text. Millions of researchers have access to the formal publications on ScienceDirect, and so links will help your users to find, access, cite, and use the best available version. Theses and dissertations which contain embedded PJAs as part of the formal submission can be posted publicly by the awarding institution with DOI links back to the formal publications on ScienceDirect.

If you are affiliated with a library that subscribes to ScienceDirect you have additional private sharing rights for others' research accessed under that agreement. This includes use for classroom teaching and internal training at the institution (including use in course packs and courseware programs), and inclusion of the article for grant funding purposes.

Gold Open Access Articles: May be shared according to the author-selected end-user license and should contain a [CrossMark logo](#), the end user license, and a DOI link to the formal publication on ScienceDirect.

Please refer to Elsevier's [posting policy](#) for further information.

18. **For book authors** the following clauses are applicable in addition to the above: Authors are permitted to place a brief summary of their work online only. You are not allowed to download and post the published electronic version of your chapter, nor may you scan the printed edition to create an electronic version. **Posting to a repository:** Authors are permitted to post a summary of their chapter only in their institution's repository.

19. **Thesis/Dissertation:** If your license is for use in a thesis/dissertation your thesis may be submitted to your institution in either print or electronic form. Should your thesis be published commercially, please reapply for permission. These requirements include permission for the Library and Archives of Canada to supply single copies, on demand, of the complete thesis and include permission for Proquest/UMI to supply single copies, on demand, of the complete thesis. Should your thesis be published commercially, please reapply for permission. Theses and dissertations which contain embedded PJAs as part of the formal submission can be posted publicly by the awarding institution with DOI links back to the formal publications on ScienceDirect.

Elsevier Open Access Terms and Conditions

You can publish open access with Elsevier in hundreds of open access journals or in nearly 2000 established subscription journals that support open access publishing. Permitted third party re-use of these open access articles is defined by the author's choice of Creative Commons user license. See our [open access license policy](#) for more information.

Terms & Conditions applicable to all Open Access articles published with Elsevier:

Any reuse of the article must not represent the author as endorsing the adaptation of the article nor should the article be modified in such a way as to damage the author's honour or reputation. If any changes have been made, such changes must be clearly indicated.

The author(s) must be appropriately credited and we ask that you include the end user license and a DOI link to the formal publication on ScienceDirect.

If any part of the material to be used (for example, figures) has appeared in our publication with credit or acknowledgement to another source it is the responsibility of the user to ensure their reuse complies with the terms and conditions determined by the rights holder.

Additional Terms & Conditions applicable to each Creative Commons user license:

CC BY: The CC-BY license allows users to copy, to create extracts, abstracts and new

works from the Article, to alter and revise the Article and to make commercial use of the Article (including reuse and/or resale of the Article by commercial entities), provided the user gives appropriate credit (with a link to the formal publication through the relevant DOI), provides a link to the license, indicates if changes were made and the licensor is not represented as endorsing the use made of the work. The full details of the license are available at <http://creativecommons.org/licenses/by/4.0>.

CC BY NC SA: The CC BY-NC-SA license allows users to copy, to create extracts, abstracts and new works from the Article, to alter and revise the Article, provided this is not done for commercial purposes, and that the user gives appropriate credit (with a link to the formal publication through the relevant DOI), provides a link to the license, indicates if changes were made and the licensor is not represented as endorsing the use made of the work. Further, any new works must be made available on the same conditions. The full details of the license are available at <http://creativecommons.org/licenses/by-nc-sa/4.0>.

CC BY NC ND: The CC BY-NC-ND license allows users to copy and distribute the Article, provided this is not done for commercial purposes and further does not permit distribution of the Article if it is changed or edited in any way, and provided the user gives appropriate credit (with a link to the formal publication through the relevant DOI), provides a link to the license, and that the licensor is not represented as endorsing the use made of the work. The full details of the license are available at <http://creativecommons.org/licenses/by-nc-nd/4.0>. Any commercial reuse of Open Access articles published with a CC BY NC SA or CC BY NC ND license requires permission from Elsevier and will be subject to a fee.

Commercial reuse includes:

- Associating advertising with the full text of the Article
- Charging fees for document delivery or access
- Article aggregation
- Systematic distribution via e-mail lists or share buttons

Posting or linking by commercial companies for use by customers of those companies.

20. Other Conditions:

v1.8

Questions? customer care@copyright.com or +1-855-239-3415 (toll free in the US) or +1-978-646-2777.

Our Ref: MD/TMPH/P7343

5th May 2016

Dear Angeline Wairegi,

Thank you for your correspondence **requesting** permission to reproduce the following material from our Journal in your printed thesis and to be posted in your university's repository at Utah State University.

'Figure 1 and figure 6 from 'Helium clusters and droplets: microscopic superfluidity and other quantum effects' By J. Peter Toennies
Molecular Physics 111: 12-13 (2013) pp.1880-1886

We will be pleased to grant entirely free permission on the condition that you acknowledge the original source of publication and insert a reference to the Journal's web site:
www.tandfonline.com

Please note that this licence does not allow you to post our content on any third party websites or repositories.

Thank you for your interest in our Journal.

Yours sincerely

Michelle Dickson – Permissions & Licensing Executive, Journals.
Routledge, Taylor & Francis Group.

4 Park Square, Milton Park, Abingdon, Oxon, OX14 4RN, UK.

Tel: +44 (0)20 7017 7413

Fax: +44 (0)20 7017 6336

Web: www.tandfonline.com

e-mail: Michelle.Dickson@tandf.co.uk

Taylor & Francis is a trading name of Informa UK Limited,
registered in England under no. 1072954

Angeline R. Wairegi

444 South 100 West, Apt. 3, Logan, UT 84321

rekmma@yahoo.co.uk; 903-240-1545

June 30, 2016

Dr. Andrew Burbanks

Department of Mathematics

University of Portsmouth

Portsmouth PO1 3HF, United Kingdom

Dr. Burbanks,

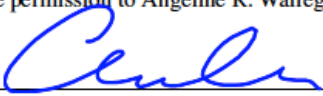
I am in the process of preparing my dissertation. I am requesting permission to include the manuscript listed below in its entirety as a chapter in my dissertation.

1. A. Wairegi, A.Gamboa, A.D Burbanks, E.A. Lee and D. Farrelly, "Microscopic superfluidity in ^4He clusters stirred by a rotating impurity molecule," Phys. Rev. Lett. 112, 143401 (2014)

I will acknowledge your contribution to this part of my dissertation by the inclusion of a footnote on the title page for that chapter. Additionally, a copy of this letter will be added to the appendix of the dissertation. Please indicate your approval of this request by signing the endorsement below. Thank you for your assistance on this matter.

Angeline R. Wairegi. Ph.D.

I hereby give permission to Angeline R. Wairegi to reprint the manuscript listed above in her dissertation.

 01/07/2016

Signature

Date

Angeline R. Wairegi, Ph.D

444 South 100 West, Apt. 3, Logan, UT 84321

rekmma@yahoo.co.uk; 903-240-1545

June 30, 2016

Dr. Antonio Gamboa

Institut de Sciences Moléculaires d' Orsay

CNRS UMR 8214

Université de Paris-Sid 11, Bâtiment 210, F9140

Orsay Cedex, France

Dr. Gamboa,

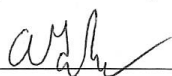
I am in the process of preparing my dissertation. I am requesting permission to include the manuscript listed below in its entirety as a chapter in my dissertation.

1. A. Wairegi, A.Gamboa, A.D Burbanks, E.A. Lee and D. Farrelly, "Microscopic superfluidity in ^4He clusters stirred by a rotating impurity molecule," Phys. Rev. Lett. 112, 143401 (2014)

I will acknowledge your contribution to this part of my dissertation by the inclusion of a footnote on the title page for that chapter. Additionally, a copy of this letter will be added to the appendix of the dissertation. Please indicate your approval of this request by signing the endorsement below. Thank you for your assistance on this matter.

Angeline R. Wairegi. Ph.D.

I hereby give permission to Angeline R. Wairegi to reprint the manuscript listed above in her dissertation.



Signature

07-06-2016

Date

Curriculum Vitae

Angeline R. Wairegi, Ph.D
 444 South 100 West, Apt. 3
 Logan, UT 84321
 rekhmma@yahoo.co.uk
 (903) 240-1545

Education

- Doctor of Philosophy, Chemistry Utah State University, Logan, UT** **March 2016**
 Dissertation: Computational studies of microscopic superfluidity in ^4He clusters
- Master of Science, Food Science Chapman University, Orange, CA** **May 2009**
 Master's project: Inhibiting lipid oxidation in cooked beef products using naturally occurring phenolic compounds
- Bachelor of Science, Chemistry University of North Texas, Denton, TX** **May 2007**
 Project: Characterization of the retention behavior of organic and pharmaceutical drug molecules on an immobilized artificial membrane column with the Abraham model

Presentation and publications

The following publications have resulted from the above detailed studies:

1. A. Wairegi, A. Gamboa-Suarez, A. D. Burbanks, E. Lee and D. Farrelly, **Microscopic superfluidity in ^4He clusters stirred by a rotating impurity molecule**, *Physical Review Letters*, **112**, pp 14301 (2014)
2. A. Wairegi and D. Farrelly, **On the fly nodal searches in importance sampled fixed node diffusion Monte Carlo using a parallel, fine-grained, genetic algorithm**, *Chemical Physics Letters*, **619**, pp 71-76 (2015)
3. L. Sprunger B.H. Blake-Taylor, A. Wairegi, W.E. Acree Jr., **Characterization of the retention behavior of organic and pharmaceutical drug molecules on an immobilized artificial membrane column with the Abraham model**, *J. Chrom. A*, **1160**, pp 235-245 (2007)

Grants

- (1) Research Enhancement Grant, Utah State University Graduate School, 2014

Research Experience

Physical Chemistry program, Utah State University, Logan, UT
2010 - 2016

Theoretical calculations on the phenomenon of microscopic superfluidity in ultra cold ^4He clusters doped with impurity molecules .

- Developed a novel approach of systematically determining the nodal hyper surfaces of wave functions using a genetic algorithm (GA) coupled to diffusion Monte Carlo (DMC) algorithms.
- Developed reduced dimensionality models to describe boson solvent - dopant molecule interactions that greatly simplified the calculations of the many-body Hamiltonian of the target systems using quantum Monte Carlo (QMC) methods.
- Analyzed the phenomenon of microscopic superfluidity in ultra cold ^4He clusters.

**Food Science program, Chapman University, City of Orange, CA
2007 - 2008**

Research into the inhibition of lipid oxidation in cooked beef samples using the naturally occurring phenols in almond skin as anti oxidants.

2006 - 2007

Analytical Chemistry program, University of North Texas, Denton, TX

Studied the retention behavior of different organic and pharmaceutical drug molecules on an immobilized artificial membrane column with the Abraham model.

University Teaching Experience

Instructor, 2012-Present

Dept. of Chemistry, Utah State University, Logan, UT

- Instructor for the online introductory Chemistry course, Chemistry 1010; assisted in setting up the online course
- Led online course session four times a week that covered lectures, discussion and review sessions on fundamental Chemistry principals.

Teaching Assistant, 2012-2013

Dept. of Chemistry, Utah State University, Logan, UT

- Teaching assistant for the upper division course, Physical Chemistry.
- Led discussion, laboratory and review sessions over the principle concepts in Physical chemistry.

Teaching Assistant, 2010-2012

Dept. of Chemistry, Utah State University, Logan, UT

- Teaching assistant for the introductory division courses, General Chemistry I and II, with a total of 72 students.
- Set up reagents, equipment to be used in laboratory experiments
- Led discussion, laboratory and review sessions over the basic concepts in Chemistry.

Teaching Assistant, 2008-2009

Dept. of Food Science, Chapman University, City of Orange, CA

- Teaching assistant for the courses, Food Processing and Preservation and Food Chemistry.
- Assisted in the preparation of laboratory experiments, grading exams and maintaining laboratory equipments and equipments.